Interconexíón monolitíca de dispositivos fotovoltaicos basados en a-Si mediante ablación directa con fuentes láser ultravioleta

Sara Lauzurica Santiago

Departamento de Física Aplicada a la Ingeniería Industrial

Universidad Politécnica de Madrid

Para la obtención del Grado de Doctor

Licenciada en CC. Físicas

Junio 2013

Título:

Interconexión monolitíca de dispositivos fotovoltaicos basados en a-Si mediante ablación directa con fuentes láser ultravioleta

Autor:

Sara Lauzurica Santiago Licenciada en CC. Físicas

Director de tesis:

Dr. Carlos Luis Molpeceres Álvarez

Tribunal nombrado por el Mgfco. y Excmo. Sr Rector de la Universidad Politécnica de Madrid el día ....

Tribunal:

Presidente: D. José Luis Ocaña Moreno.

Secretario: D. Miguel Morales Furió.

Vocal: D. Heinz P. Huber

Vocal: D. Julio Cárabe López

Vocal: D. Joan Bertomeu Balagueró

Suplente: Javier Gandía Alabau

Suplente: Cristobal Voz Sánchez

Realizado el acto de lectura y defensa de la tesis el día 23 de Julio de 2013

Calificación de la Tesis ....

El presidente: Los Vocales:

El Secretario:

Agradecimientos

En primer lugar, me gustaría mostrar mi mayor agradecimiento a Carlos Molpeceres, el director de esta tesis, y un gran amigo. Ha sido un pilar fundamental en la consecución de este trabajo, con sus ánimos y su inestimable ayuda técnica. Pero, debo también agradecerle su gran calidad humana, y todo lo que me ha ayudado en estos años (que han sido unos cuantos) tanto personal como profesionalmente. Sin él, este trabajo no hubiera sido posible.

Esta tesis está enmarcada en la estrecha colaboración establecida con el Grupo de Silicio depositado del Ciemat y la Universidad de Barcelona. Me gustaría por tanto agradecer a ambos grupos la disposición de las muestras para realizar este trabajo y su ayuda técnica en el campo fotovoltaico. En especial, a Julio Cárabe, Javier Gandía y Joan Bertomeu por el apoyo recibido a lo largo de estos años.

Expresar también mi agradecimiento al Centro Láser por los medios puestos a mi disposición para la realización de esta tesis, y al departamento de Física Aplicada a la Ingeniería Industrial de la ETSII por la posibilidad de iniciar mi carrera docente.

También quiero expresar mi gratitud al acogimiento que me brindaron el Prof. Ian Boyd durante mi estancia en el London Centre for Nanotechnology, así como a el Prof. Heinz Huber en la Universidad de Ciencias Aplicadas de Munich.

Agradezco al MICINN y al MINECO por la financiación recibida a través de la Beca FPI que dió pie al comienzo de esta tesis, y a los proyectos de investigación que han financiado la realización de la misma.

Agradecer también a mis compañeros del Centro Láser su apoyo y buenos ratos, en especial a Juanjo, Isabel, Miguel Morales, Juan, Alberto y a los que han seguido su carrera fuera del centro, Manu y Mónica.

Me gustaría agradecer especialmente a Javi su apoyo incondicional y su amor a lo largo de todos los años que llevamos juntos, su comprensión y paciencia han sido fundamentales en esta etapa. Agradecer también a mi familia su aliento para que este trabajo saliera adelante.

Por último mencionar a Germán e Irene que son la feliz razón por la que, en parte, este trabajo se haya alargado más de lo previsto.

Contents

List of Figures **vii**

List of Tables **xiii**

1 Introduction **1**

1.1 Photovoltaic Technology 2

1.2 Current Situation and Future of Photovoltaic Technology 3

1.3 Laser Monolithic Interconnection of Thin Film Modules 8

2 Laser-Material Interaction **13**

2.1 Laser Solid Interactions 13

2.2 Thermal Diffusion in Laser Irradiation 16

2.3 Laser Damage Threshold Calculation 19

2.4 Damage Threshold Calculation for Energy Gaussian Distributions . . . 20

3 Materials and Methods **23**

3.1 Design and Deposition of the Samples 23

3.2 Laser Systems 26

3.2.1 355 nm Nanosecond Laser Set-up 26

3.2.2 355 nm Picosecond Laser Set-up 28

3.3 Laser Scribing Characterization 30

3.3.1 Scanning Electron Microscope (SEM) and EDX (Energy Dispersive X-Ray) Spectroscopy Analysis 30

3.3.2 Confocal Laser Scanning Microscopy 33

3.3.3 Raman Spectroscopy 35

3.3.4 IR-VIS Spectrometry 40

3.3.5 Electrical Characterization 45

4 Scribing Results 49

4.1 Scribing of Transparent Conductive Oxides (TCO) Layers 49

4.1.1 Damage Fluence Threshold Results 50

4.1.1.1 Single Pulse Damage Threshold for λ = 355 nm and Nanosecond Pulse-width 51

4.1.1.2 Single Pulse Damage Threshold for λ = 355 nm and Picosecond Pulse-width 52

4.1.1.3 Single pulse damage threshold for λ = 1064 nm and picosecond pulse-width 53

4.1.1.4 Multi-pulse Damage Threshold for λ = 355 nm and Nanosecond Pulse-width 54

4.1.1.5 Multi-pulse damage Threshold for Picosecond Pulse-width 55

4.1.2 TCO Scribing Results 58

4.1.2.1 Asahi-U Scribing Characterization 59

4.1.2.2 ITO Scribing Characterization 64

4.1.2.3 AZO Scribing Characterization 71

4.2 Scribing of a-Si:H Structure Layer 76

4.2.1 Damage fluence threshold results. 76

4.2.1.1 Single Pulse Damage Threshold at λ = 355 nm and Nanosecond Pulse-width. 77

4.2.1.2 Multi-pulse Damage Threshold at λ = 355 nm Nanosecond Radiation. 78

4.2.1.3 Single pulse damage threshold at λ = 355 nm, 1064 nm and picosecond pulse-width. 79

4.2.1.4 Multi-pulse damage threshold at λ = 355 nm, 1064 nm 80

4.2.2 Selective ablation of a-Si:H structure characterization 81

4.3 Selective Ablation of Front Contact Characterization 87

4.3.1 Substrate configuration 88

4.3.1.1 Ad-hoc modules with AZO deposited by UB 89

4.3.1.2 Commercial modules from GADIR 91

4.3.2 Superstrate configuration 94

4.3.2.1 Laser direct scribing interconnection of a complete module in superstrate configuration 100

5 Conclusions **105**

6 Lines of Future Development **109**

List of Publications **111**

References **113**

List of Figures

1.1 Growth of photovoltaic capacity installed worldwide since 2000. 4
1.2 Three mayor thin film technologies in the current market with their corresponding typical efficiencies 6
1.3 Organic photovoltaic module.(Source: Heliatek GmbH) 7
1.4 Process flow for manufacturing a module by monolithic interconnection. 8
1.5 Superstrate/Substrate configuration attending to the material sequence deposition 9
1.6 Laser monolithic interconnection for the two different structure configuration 10

2.1 Laser excitation of electrons. The linear absorption including (a) free-carrier absorption (b) interband single-photon absorption. The non-linear optical process is found in (c) interband multi-photon absorption, (d) avalanche ionization [66]. 15
2.2 Different time scale in the laser excitation of materials [66] 17
2.3 Laser-matter interaction attending to the pulse duration 18

3.1 PECVD system at CIEMAT facilities 24
3.2 RF sputtering plant using a MV Systems device at CIEMAT facilities . 25
3.3 Typical performance data for HIPPO laser source at different frequencies 27
3.4 HIPPO setup scheme 28
3.5 Innolas set-up scheme 30
3.6 Techniques obtained with the SEM EDX system available at Centro Laser UPM 32
3.7 Confocal squeme 33

3.8 Combination of three techniques in scribing morphology evaluation . . . 34
3.9 3-D confocal topographical reconstruction with its corresponding profile 35
3.10 Examples of Raman spectra taken on our set up for different phases of the silicon in a thin layer 37
3.11 Effect of excitation light power (P) on the Raman spectrum of an a-Si:H sample 39
3.12 Raman spectrum and peak deconvolution of a-Si:H 40
3.13 Schematic diagram showing sample structure and measurement procedure performed for the acquisition of the transmittance spectra. 41
3.14 Transmittance spectra, measured at different positions (x) from the center of the a-Si:H sample: (a) before and (b) after a laser direct-scribing treatment. Reference corresponds to the spectrum acquired at x=0 mm before the laser process. 42
3.15 Variation of the refractive index as a function of the distance from the groove center 44
3.16 Model showing the relation between the Gaussian fit of the refraction index variation and laser groove characteristics lengths for laser treated a-Si:H layers. 45
3.17 a) Equivalent circuit of a solar cell, b) J-V curve showing the ideal J-V curve (black line) and the effects of the variation of the internal resistance of the device (red and blue lines) 46

4.1 Damage threshold calculation, crater diameter represented as a function of its energy per pulse for 50 KHz of repetition rate with the corresponding fitting line and the damage threshold result 51
4.2 Damage threshold calculation, crater diameter represented as a function of its energy per pulse for 10 KHz of repetition rate with the corresponding fitting line and the damage threshold result 53
4.3 Damage threshold calculation, crater diameter represented as a function of its energy per pulse for 10 KHz of repetition rate with the corresponding fitting line and the damage threshold result 54
4.4 Damage threshold for 1000 pulses as a function of the repetition rate for 355 nm and nanosecond pulse-width 55

4.5 Damage threshold for 1000 pulses as a function of the repetition rate for 355 nm and picosecond pulse-width 56
4.6 Damage threshold for 1000 pulses as a function of the repetition rate for 1064 nm and picosecond pulse-width 58
4.7 Contact resistance of grooves performed at the maximum energy per pulse of the laser sources for different speed process. 60
4.8 Contact resistance of grooves performed at 50 KHz, 350 mms^{-1} for nanosecond radiation and 10 KHz, 70 mms^{-1} for picosecond pulses, varying the energy per pulse 60
4.9 SEM image and Confocal profiles of the optimal laser scribe performed with nanosecond pulses and 355 nm of wavelength 61
4.10 SEM image and Confocal profiles of the optimal laser scribe performed with picosecond pulses and 355 nm of wavelength 62
4.11 Substrate damage assessment of laser scribing of Asahi-U over glass for the nanosecond source with a fixed repetition rate of 50KHz and 350 mms^{-1} 63
4.12 Substrate damage assessment of laser scribing of Asahi-U over glass for the nanosecond source with a fixed repetition rate of 10 KHz and 70 mm s^{-1} 65
4.13 SEM image and Confocal profiles of the optimal laser scribe performed with nanosecond pulses and 355 nm of wavelength at 1050 mm s^{-1} . . . 67
4.14 SEM image and Confocal profiles of the optimal laser scribe performed with picosecond pulses and 355 nm of wavelength at 530 mm s^{-1} 67
4.15 SEM images of ITO laser scribes carried out with nanosecond pulse-width at 355 nm of wavelength and 1050 mm s^{-1} of speed process . . . 68
4.16 SEM images of ITO laser scribes carried out with nanosecond pulse-width at 355 nm of wavelength and 600 mm s^{-1} of speed process 69
4.17 SEM images of ITO laser scribes carried out with nanosecond pulse-width at 355 nm of wavelength and 530 mm s^{-1} of speed process 69
4.18 Confocal, EDX profiles and a confocal topographical image where the accumulation with the increase of of processing energy of material is demonstrated 70

4.19 Confocal profiles and topographical images of laser scribes carried out at 355 nm and picosecond pulse-width for different pulse energies. . . . 70
4.20 Contact resistance of grooves performed at 50 KHz, 600 mms^{-1} and nanosecond radiation and 10 KHz, 350 mms^{-1} for picosecond pulses, varying the energy per pulse 72
4.21 SEM image and Confocal profiles of the optimal laser scribe performed with nanosecond pulses and 355 nm of wavelength at 600 mms^{-1} of speed process and 5.96 μJ of pulse energy. 72
4.22 SEM image and Confocal profiles of the optimal laser scribe performed with picosecond pulses and 355 nm of wavelength at 350 mms^{-1} of speed process and 33.8 μJ of pulse energy. 73
4.23 Laser scribes of AZO over glass performed at nanosecond radiation of 355 nm of wavelength 50 KHz and 5.96 μJ of pulse energy. 74
4.24 EDX Zinc profiles of laser scribes of AZO over glass performed at nanosecond radiation of 355 nm of wavelength 50 KHz and 5.96 μJ of pulse energy, varying the scribing speed. 74
4.25 Laser scribes of AZO over glass performed at picosecond radiation of 355 nm of wavelength 10 KHz and a common pulse energy of 33.8 μJ. 75
4.26 EDX Zinc profiles of laser scribes of AZO over glass performed at picosecond radiation of 355 nm of wavelength 10 KHz and 33.8 μJ of pulse energy, varying the scribing speed. 75
4.27 Damage threshold calculation, crater diameter represented as a function of its energy per pulse for three repetition rates with the corresponding fitting line and the damage threshold result 77
4.28 Damage threshold for 1000 pulses as a function of the repetition rate for 355 nm and nanosecond pulse-width 78
4.29 Damage threshold crater diameter represented as a function of its energy per pulse with the corresponding fitting line and the ablation threshold result for two wavelengths 80
4.30 Damage threshold for 1000 pulses as a function of the repetition rate for 355 nm and nanosecond pulse-width 81
4.31 SEM images and EDX profiles of laser scribes at nanosecond and picosecond radiation of a-Si:H (pin)/Asahi-U/Glass) 83

4.32 Confocal and EDX profiles of laser scribes of asi (pin)/Asahi-U/Glass for optimal scribes for two different pulse-widths 84
4.33 EDX profiles and SEM images of laser scribes at picosecond radiation of a-Si:H (pin)/Asahi-U/Glass to illustrate the damage on the TCO layer . 85
4.34 Raman crystalline fraction study of a-Si:H structure performed from the edge of the groove with ns and ps radiation for different energy conditions 86
4.35 Samples used in substrate configuration. 88
4.36 SEM image, EDX profile, Confocal profile and 3D topographical image for P3 laser scribing step for two different pulse-widths 90
4.37 Raman crystalline fraction study of a-Si:H structure performed with ns and ps pulses for different energy conditions 92
4.38 SEM image and EDX profile picosecond scribe with 100KHz of repetition rate 250 mm/s of speed process and 600 mW two lines overlapped and 30 minutes of Ultrasonic cleaning 93
4.39 Crystalline fraction assessment of a-Si:H structure in the vicinity of the groove 94
4.40 Samples used in superstrate configuration. 94
4.41 Damage threshold result for Aluminum layer obtained for nanosecond and picosecond radiation 95
4.42 Sketch of P3 experiments over a cell with Aluminium layer as back contact with its corresponding electrical characterization by means of dark current curves. 96
4.43 SEM image and EDX profile of the best laser scribe performed at 496 mW, 50KHz, 30% overlap 96
4.44 J-V characteristic where pulse energy assessment has been performed with picosecond 355 nm radiation 98
4.45 J-V characteristic for multiples lines in a cell for three different fluences of picosecond 355 nm radiation 99
4.46 SEM image, EDX profile and 3D image and depth Confocal profile performed with laser parameters obtained by the presented study for T-Solar modules. 100
4.47 Structure and picture of the final module interconnected performed by means of laser direct scribing at 355 nm and picosecond pulses. 101

4.48 SEM images of the three steps of the laser monolithic interconnection. . 101
4.49 Confocal characterization of laser interconnection process in direct scribing configuration by means of 3D topographical images of the three laser steps carried out in the final device. 102
4.50 J-V characteristics of the cells which make up the complete module . . . 103
4.51 J-V characteristic of the functional module fully interconnected by laser direct scribing with 355 nm and picosecond pulses 104

List of Tables

3.1 Sample features used in this work 24
3.2 Laser specifications of HIPPO SPECTRA PHYSICS system for 355 nm of wavelength 27
3.3 Laser specifications of LUMERA SUPER RAPID system. 29

4.1 Single pulse damage threshold values obtained for nanosecond pulse-width radiation at 355 nm of wavelength 51
4.2 Single pulse damage threshold values obtained for picosecond pulse-width radiation at 355 nm of wavelength 52
4.3 Single pulse damage threshold values obtained for picosecond pulse-width radiation at 1064 nm of wavelength 53
4.4 Damage threshold values obtained for 1000 pulses as a function of the repetition rate for nanosecond pulse-width radiation and 355 nm of wavelength 56
4.5 Damage threshold comparison for $\lambda = 355$ nm 15 ns of pulsewidht and 50 KHz of repetition rate. 56
4.6 Damage threshold values obtained for picosecond pulse-width radiation at 355 nm of wavelength 57
4.7 Damage threshold comparison for $\lambda = 355$ nm 8 ps of pulse-width. . . . 57
4.8 Damage threshold values obtained for picosecond pulse-width radiation at 1064 nm of wavelength 57
4.9 Damage threshold comparison for $\lambda = 1064$ nm 8 ps of pulse-width. . . 58
4.10 Laser process parameters for optimal scribes over Asahi-U for nanosecond and picosecond UV radiation 64

4.11 Laser process parameters for optimal scribes over ITO for nanosecond and picosecond UV radiation 66
4.12 Laser process parameters for optimal scribes over AZO for nanosecond and picosecond UV radiation 72
4.13 Single pulse damage threshold values of a-Si:H obtained for nanosecond pulse-width radiation at 355 nm of wavelength 77
4.14 Damage threshold values obtained for 1000 pulses as a function of the repetition rate for nanosecond pulse-width radiation and 355 nm of wavelength 79
4.15 Single pulse damage threshold values obtained for nanosecond pulse-width radiation at 355 nm of wavelength 79
4.16 Damage threshold values obtained for 1000 pulses as a function of the repetition rate for picosecond pulse-width radiation at 355 and 1064 nm of wavelength 81
4.17 Laser parameter for the optimal scribes of amorphous silicon structure layer in terms of fluence (J/cm^2) and number of pulses per location with damage of threshold of 0.13 and 0.11 J/cm^2 for ns and ps radiation respectively 82
4.18 Laser parameter for the optimal scribes of P3 step over AZO layer of the ad-hoc module in terms of fluence (J/cm^2) and damage threshold values 0.184 and 0.324 J/cm^2 for ns and ps radiation 89
4.19 Laser parameter for the optimal scribes P1 over Asahi-U, P2 and P3 over Aluminum. 101
4.20 I-V relevant characteristics for the eight cells which compone the functional module, each cell has 7.5 cm^2 of area 103

Resumen

En la última década la tecnología láser se ha convertido en una herramienta imprescindible en la fabricación de dispositivos fotovoltaicos, muy especialmente en aquellos basados en tecnología de lámina delgada. Independientemente de crisis coyunturales en el sector, la evolución en los próximos años de estas tecnologías seguirá aprovechándose de la flexibilidad y calidad de proceso de la herramienta láser para la consecución de los dos objetivos básicos que harán de la fotovoltaica una opción energética económicamente viable: la reducción de costes de fabricación y el aumento de eficiencia de los dispositivos.

Dentro de las tecnologías fotovoltaicas de lámina delgada, la tecnología de dispositivos basados en silicio amorfo ha tenido un gran desarrollo en sistemas estándar en configuración de superestrato, pero su limitada eficiencia hace que su supervivencia futura pase por el desarrollo de formatos en configuración de substrato sobre materiales flexibles de bajo coste. En esta aproximación, las soluciones industriales basadas en láser actualmente disponibles para la interconexión monolítica de dispositivos no son aplicables, y desde hace años se viene investigando en la búsqueda de soluciones apropiadas para el desarrollo de dichos procesos de interconexión de forma que sean transferibles a la industria.

En este contexto, esta Tesis propone una aproximación completamente original, demostrando la posibilidad de ejecutar una interconexión completa de estos dispositivos irradiando por el lado de la lámina (es decir de forma compatible con la opción de configuración de substrato y, valga la redundancia, con el substrato del dispositivo opaco), y con fuentes láser emitiendo en UV. Este resultado, obtenido por primera vez a nivel internacional con este trabajo, aporta un conocimiento revelador del verdadero potencial de estas

fuentes en el desarrollo industrial futuro de estas tecnologías. Si bien muy posiblemente la solución industrial final requiera de una solución mixta con el empleo de fuentes en UV y, posiblemente, en otras longitudes de onda, esta Tesis y su planteamiento novedoso aportan un conocimiento de gran valor a la comunidad internacional por la originalidad del planteamiento seguido, los resultados parciales encontrados en su desarrollo (un número importante de los cuales han aparecido en revistas del JCR que recogen en la actualidad un número muy significativo de citas) y porque saca además a la luz, con las consideraciones físicas pertinentes, las limitaciones intrínsecas que el desarrollo de procesos de ablación directa selectiva con láseres UV en parte de los materiales utilizados presenta en el rango temporal de interacción de ns y ps.

En este trabajo se han desarrollado y optimizado los tres pasos estándar de interconexión (los habitualmente denominados P1, P2 y P3 en la industria fotovoltaica) demostrando las ventajas y limitaciones del uso de fuentes en UV tanto con ancho temporal de ns como de ps. En particular destaca, por el éxito en los resultados obtenidos, el estudio de procesos de ablación selectiva de óxidos conductores transparentes (en este trabajo utilizados tanto como contacto frontal así como posterior en los módulos) que ha generado resultados, de excelente acogida científica a nivel internacional, cuya aplicación trasciende el ámbito de las tecnologías de silicio amorfo en lámina delgada.

Además en este trabajo de Tesis, en el desarrollo del objetivo citado, se han puesto a punto técnicas de análisis de los procesos láser, basadas en métodos avanzados de caracterización de materiales (como el uso combinado de la espectroscopía dispersiva de rayos X y la microscopía confocal de barrido) que se presentan como auténticos avances en el desarrollo de técnicas específicas de caracterización para el estudio de los procesos con láser de ablación selectiva de materiales en lámina delgada, procesos que no solo tienen impacto en el ámbito de la fotovoltaica, sino también en la microelectrónica, la biotecnología, la microfabricación, etc. Como resultado

adicional, parte de los resultados de este trabajo, han sido aplicados exitosamente por el grupo de investigación en la que la autora desarrolla su labor para conseguir desarrollar procesos de enorme interés en otras tecnologías fotovoltaicas, como las tecnologías estándar de silicio amorfo sobre vidrio en configuración de superestrato o el procesado de capas delgadas en tecnologías convencionales de silicio cristalino.

Por último decir que este trabajo ha sido posible por una colaboración muy estrecha entre el Centro Láser de la UPM, en el que la autora desarrolla su labor, y el Grupo de Silicio Depositado del Centro de Investigaciones Energéticas, Medioambientales y Tecnológicas, CIEMAT, que, junto al Grupo de Energía Fotovoltaica de la Universidad de Barcelona, han preparado la mayor parte de las muestras utilizadas en este estudio. Dichas colaboraciones se han desarrollado en el marco de varios proyectos de investigación aplicada con subvención pública, tales como el proyecto singular estratégico PSE-MICROSIL08 (PSE-120000-2006-6), el proyecto INNDISOL (IPT-420000-2010-6), ambos financiados porel Fondo Europeo de Desarrollo Regional FEDER (UE) "Una manera de hacer Europa y el MICINN, y los proyectos de Plan Nacional AMIC (ENE2010-21384-C04-02) y CLÁSICO (ENE2007-6772-C04-04), cuya financiación ha permitido en gran parte llevar a término este trabajo.

Abstract

In the last decade, the laser technology has turned into an indispensable tool in the production of photovoltaic devices, especially of those based on thin film technology. Regardless the current crisis in the sector, the evolution of these technologies in the upcoming years will keep taking advantage of the flexibility and process quality of the laser tool for the accomplishment of the two basic goals that will convert the photovoltaic energy into economically viable: the manufacture cost reduction and the increase in the efficiency of the devices.

Amongst the thin film laser technologies, the technology of devices based on amorphous silicon has had a great development in standard systems of superstrate configuration, but its limited efficiency makes its survival dependant on the development of formats in substrate configuration with low cost flexible materials. In this approach, the laser industrial solutions currently available for the monolithic interconnection are not applicable, and in the last few years the investigations have been focused on the search of appropriate solutions for the development of such interconnection processes in a way that the same are transferable to the industry.

In this context, this Thesis proposes a totally original approach, proving the possibility of executing a full interconnection of these devices by means of irradiation from the film side, i.e., compatible with the substrate configuration, and with UV laser sources. This result, obtained for the first time at international level in this work, provides a revealing knowledge of the true potential of these sources in the future industrial development of these technologies. Even though very probably the final industrial solution will require a combination of the use of UV sources along with other wavelengths, this Thesis and its novel approach contribute with a high value

to the international community because of the originality of the approach, the partial results found throughout its development (out of which, a large number has appeared in JCR journals that currently accumulate a significant number of citations) and brings to light, with the pertinent scientific considerations, the intrinsic limitations that the selective direct ablation processes with UV laser present in the temporal range of interaction of ns and ps for part of the materials used in this study.

More particularly, the three standard steps of interconnection (usually denominated P1, P2 and P3 in the photovoltaic industry) have been developed and optimized, showing the advantages as well as the limitations of the use of UV sources in both the ns and ps pulse-width ranges. It is highly remarkable, because of the success in the obtained results, the study of selective ablation processes in transparent conductive oxide (in this work used as a front and back contact), that has generated results, of excellent international scientific reception, whose applications go beyond the scope of thin film photovoltaic technologies based on amorphous silicon.

Moreover, in this Thesis, with the development of the mentioned goal, different techniques of analysis of laser processes have been fine-tuned, basing the same in advanced methods for material characterization (like the combined use of EDX Analysis and Confocal Laser Scanning Microscopy) that can be presented as true breakthroughs in the development of specific techniques for characterization in the study of laser processes of selective ablation of materials in thin film technologies, processes that not only have impact in the photovoltaic field, but also in those of microelectronics, biotechnology, micro-fabrication, etc.

As an additional outcome, part of the results of this work has been successfully applied, by the investigation group to which the author belongs, to the development of processes of enormous interest within other photovoltaic technologies, such as the standard technologies on amorphous silicon over glass in superstrate configuration or the processing of thin layers in conventional technologies using crystalline silicon.

Lastly, it is important to mention that this work has been possible thanks to the close cooperation between the Centro Láser of the UPM, in which the author develops her work, and the Grupo de Silicio Depositado of Centro de Investigaciones Energéticas, Medioambientales y Tecnológicas, CIEMAT, which, along with the Grupo de Energía Fotovoltaica of Universidad de Barcelona, has prepared the largest part of the samples utilized in this study. Such collaborations have been carried out in the context of several projects of applied investigation with public funding, like Proyecto Singular Estratégico PSE-MICROSIL08 (PSE-120000-2006-6), Proyecto INNDISOL (IPT-420000-2010-6), both funded by the European Regional Development Fund (ERDF), "Una manera de hacer Europa" and MICINN, and the projects of Plan Nacional AMIC (ENE2010-21384-C04-02) and CLÁSICO (ENE2007-6772-C04-04), whose funds have enabled the development of large part of this work.

1

Introduction

The beginning of this work is framed at the start of a collaboration that our group maintains with CIEMAT, where it is proposed the first monolithic interconnection by laser processing of photovoltaic modules based on amorphous silicon in Spain. The work was initiated with the first of the three laser steps that conform the interconnection, i.e. the front contact removal to isolate and define the cells within a module. This study assessed the effect of the laser wavelength on the process, and the results showed UV wavelength as the best option to carry out the isolation, with good electrical and morphological results [51].

At that time, the first patent of laser scribing with UV laser of transparent conductive oxide came to light [36]. This, along with the good results obtained for the first laser step performed with a Diode Pumped Solid State (DPSS) UV laser source, lead us to consider a newer and more original approach for the monolithic interconnection than the one being performed at that time consisting in performing the first step, so called P1, with Infrared lasers and second (P2) and third (P3) steps with green laser sources through the glass substrates in backscribing configuration.

It has been observed that UV laser sources offer better behavior within a wide range of materials [6]. This, alongside the possibility to reduce the size of the laser process, leads to formulate a sole and different geometrical configuration, where the laser source is the same for the three laser steps of the interconnection, and the processes P1, P2 and P3 are performed from the film side in a direct scribing configuration. This approach offers no restrictions as to the choice of materials which make up the devices and offers

the possibility to opt for opaque substrates. More details about this will be provided further in this work.

This thesis deals with the laser interconnection steps from the film side, assessing the same for two different laser sources working at 355 nm of wavelength with two different pulse-width ranges: nanosecond and picosecond. It this work it will be found an exhaustive parametrization and characterization of the laser processes involved.

1.1 Photovoltaic Technology

Within renewable energy, research in photovoltaic power generation has always been a priority. This research follows a clear objective: to increase as much as possible the level of efficiency (and if possible leading to its theoretical limits) with lower material and energy input to the device, and it is right on the achievement of this objective where laser techniques are indispensable tools to convert solar photovoltaic energy in an energetic alternative economically viable.

During the last few years laser technology has been used in manufacturing of photovoltaic devices based on standard cell technology. Thus the laser cutting of crystalline and polycrystalline silicon, the edge isolation techniques and laser buried contacts are usual in production processes. Amongst the technologies based on thin film (CdTe, CIS / CIGS or a-Si:H) laser techniques acquire a yet more relevant and clear strategic role. In particular, laser ablation techniques in thin film modules (laser scribing) have proven to be the most effective, and most industrially favourable for the monolithic interconnection processing of these devices [2, 58]. Something similar happens in the race, particularly active at present, to achieve the development of high efficiency crystalline cells, where new techniques for laser contact definition (using point contact or transfer processes), and new selective doping open up new expectations in improving the efficiency of these devices. Even in devices and processes that are still in basic research, such as organic cells or advanced nanotechnology processes to increase efficiency, the laser tool appears as the ideal companion for the realization of the same. Such is the current impact of laser technology in the photovoltaic manufacturing, and so spectacular the future growth prospects, that it should be highlighted that this field appears, at industrial level as the most dynamic in the development of new laser techniques and systems, as well as the market with largest potential. This fact has been recognized

by the companies in the photovoltaic sector, the laser manufacturers as well as the integrators and developers of laser machinery, as a market niche that has completely refocused its business in recent years. However, the strategic nature of these processes in manufacturing makes the access to knowledge (especially scientific developments, both theoretical and applied) very restricted. It is a fact that almost all technological development has been done by the companies that today dominate the photovoltaic area (Sanyo, Applied Materials, Oerlikon, Manz, etc.), leading the rest of the sector to a strong dependence on suppliers equipment or developments with restrictive intellectual protection. Thus, relevant references like Sanyo (which with its HIT heterojunction product maintains approximately 4% of the global PV market [49]), dedicate a special effort to develop new technologies to produce devices with laser techniques, to the point of conditioning aspects that were formerly governed by pure electronic criteria, such as the layout and film thickness [65]. Obviously, considering the importance of these developments for the industry and its current dependence on a very small number of manufacturers of specific devices or machines, public research groups have started consolidating the existing development, filling a large portion of the knowledge gap, and opening a bright future to the partnership between laser techniques and high efficiency and low cost photovoltaic devices.

1.2 Current Situation and Future of Photovoltaic Technology

For a long time the PV has evolved as a marginal sector within the energy market. However, in recent years, the cost evolution has shown a steady trend in reduction of the same, associated with an increase in annual market volume of around 40%, only braking in 2009 (where growth was only 25 %) by the global economic crisis. However in 2010 the sector's recovery was excellent and the annual installed capacity doubled the one from 2009 see Fig. 1.1 and almost doubled up again in 2011, reaching a worldwide cumulative installed capacity of 70 GW. However, the current situation in PV market is highly volatile, and the prospects for near future are strongly dependent on the economic policies adopted by the leading countries in this sector, specially the position taken by the Chinese authorities.

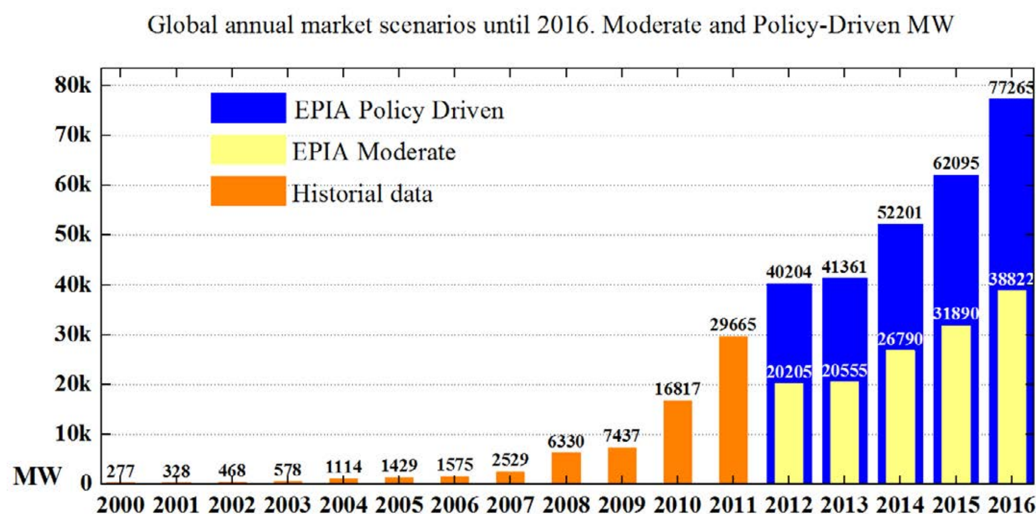

Figure 1.1: Growth of photovoltaic capacity installed worldwide since 2000.

These excellent prospects for the PV market may be still critically enhanced if there was a definitive incorporation of photovoltaics for energy production in the countries of the so-called ”sun belt” (region between 35 degrees north latitude and 35 ° latitude south). A group of countries (China, India, Mexico, Indonesia, etc.) densely populated (the region represents 78% of the world population), with an excellent location for photovoltaic energy production, with an average GDP growth of more than 3.1% per year and a spectacular expected increase in energy demand in the upcoming years.

But the realization of these excellent prospects has been possible mainly thanks to the reduced costs of photovoltaic systems. In just five years, the unit costs have been reduced by approximately 30%. This has been achieved through a constant technological development of the sector, which not only has reduced drastically the manufacturing costs of the devices, but also increased their efficiency making the overall cost of electricity generation gradually lower and providing the industry with a very promising future.

From the technological point of view, photovoltaics is still dominated by crystalline silicon-based devices (almost 90% market share in 2010), but all forecasts point to a relative market size for thin film and other emerging technologies growing in the coming years.

As mentioned, to date, PV sector has been dominated by technologies based on silicon wafers (crystalline and polycrystalline). These technologies reported typical cell efficiencies between 14% and 22% (between 12% and 19% in module) and now suffering a market-based rejuvenation to reduce the amount of silicon that is used without compromising its high efficiency.

This will develop new concepts for achieving the so called high efficiency cells (HE), in particular by means of the innovation in the designs of front and back contacts, or through the use of hybrid technologies combining thin film and conventional crystalline cells (as heterojunction cells). The really relevant fact is that laser technology appears as essential to achieve the goal of cost reduction and increased efficiency.

Focusing on thin film technology, where this work is centred, this has the advantage of using very little material that is grown on low cost substrates, allowing the design and implementation of flexible modules with advanced manufacturing techniques like roll-to-roll.

Currently there are four types of thin film modules in the market: single junction amorphous silicon, multijunction amorphous silicon, chalcogenides technologies (CIS/CIGS) and CdTe modules [18, 28, 39]. The first two, which traditionally go under the name of thin-film silicon technology, are based on the use of thin film amorphous silicon as a semiconductor material [8]. But, while the single junction module has a very low cost in production with low efficiency (7-8%), and can be produced with sizes of several square meters which helps to reduce the production cost, the multijunction adds additional layers to the structure (including microcrystalline silicon), which increases the efficiency (up to 10%) and module stability, but consists in having to significantly reduce the deposited area, which limits their use for example in architectural integration. CdTe technology is the one with lower production costs, and its efficiency (around 11%) is very reasonable. However, the toxicity and the lack of materials that are used in this technology, do not make it a sustainable alternative over time, at least when it is compared to its competitors. Fig. 1.2 presents the most important thin film module technologies with its corresponding device standard efficiencies.

$CuInSe_2$ (CIS) and $Cu(In,Ga)Se_2$ (CIGS) are two of the most promising materials for thin-film photovoltaic devices due to the suitability of its bandgap and its high-absorption coefficient for solar radiation. Recently, the efficiency of CIGS thin-film solar cells has reached 20.3%. In commercial modules currently has reached up to

(a) Cd/Te Typical efficiency 12 % Image: First Solar

(b) CIS/CIGS Typical efficiency 12-14% Image: Global

(c) a-Si:H Typical efficiency 7-8% Image: T-Solar

Figure 1.2: Three mayor thin film technologies in the current market with their corresponding typical efficiencies

14%, making this technology the most promising in the field of thin film. However, dependence of a scarce and expensive material as the Indium (which also depends on the TFT industry) and Gallium can cause current cost increases, so finding alternative materials in CIGS has now become crucial.

Finally it is necessary to discuss what is the current status of concepts such as Organic photovoltaic (OPV) cells Fig. 1.3. The so-called 'third generation' of solar technology offers exciting opportunities thanks to the potential for very cheap manufacture, lightweight and compatibility with flexible substrates, which means they are ideal for portable electronic device applications. This new OPV technology is a significant breakthrough as scientists have addressed the problem of low output voltage when the module is in low light levels or partial shading, taking an important step towards rolling out cheap OPV cells in low-power portable electronics.

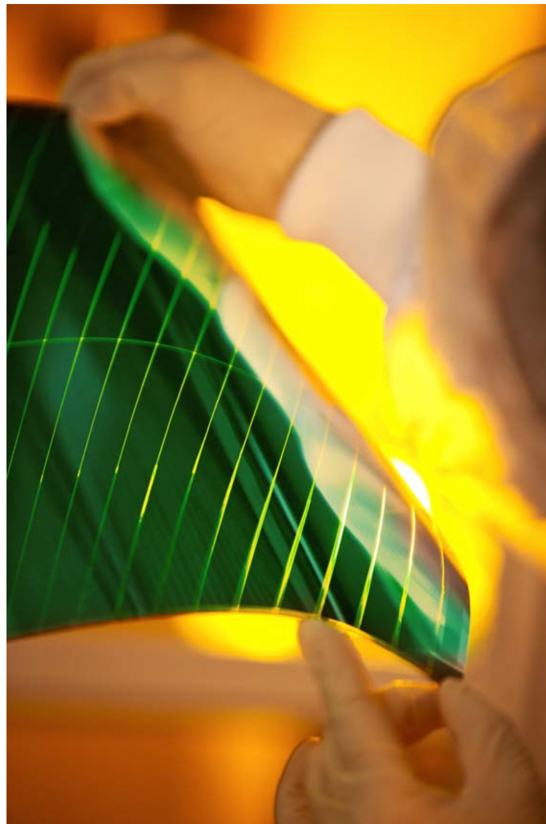

Figure 1.3: Organic photovoltaic module.(Source: Heliatek GmbH)

1.3 Laser Monolithic Interconnection of Thin Film Modules

Although historically laser processes were first used in photovoltaic technologies based on crystalline silicon (mainly for cutting edge and isolation of cells), its main potential field has proven to be the fabrication of thin film modules [19]. We have already mentioned that there are currently three main groups of thin-film modules in the market, based on a-Si:H , and the chalcogenide (CIS / CIGS) and CdTe based.

In these technologies, the deposit of material over large areas makes necessary, for the device to be functional, to subdivide the area into smaller cells that have to be connected in series to draw the current of the device properly [12, 33]. This process alternates deposition steps processes and the definition of lines by selective ablation, removing selectively the contact and semiconductor layers in order to achieve monolithic interconnection [24, 55]. This selective removal is made almost exclusively by laser ablation in the case of amorphous silicon modules and combines laser ablation and mechanical processes for CdTe and CIGS technologies, although the current trend is to substitute as much as possible the mechanical steps by laser ablation processes [53]. As an example Fig. 1.4 shows the manufacturing process flow of a module of a-Si:H.

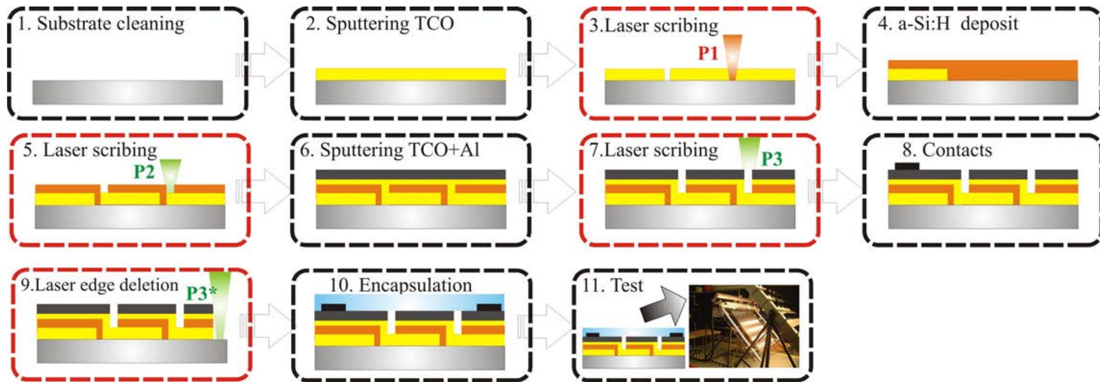

Figure 1.4: Process flow for manufacturing a module by monolithic interconnection.

Thin-film solar cell devices are configured in either substrate or a superstrate structure shown in Fig. 1.5. For superstrate configuration, the substrate is transparent and the contact is made by a conducting oxide coating on the substrate. For substrate configuration, where the light is entering through the last deposited layer, the proper

substrate can be metal or metallic coating on a glass/polymer substrate which also acts as the back contact [39].

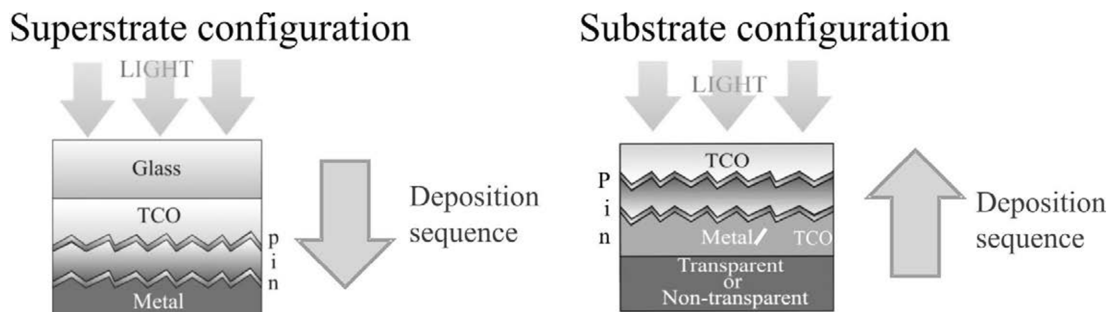

Figure 1.5: Superstrate/Substrate configuration attending to the material sequence deposition

The monolithic interconnection of the cells is fully industrialized and performed by laser scribing for the superstrate structure configuration of thin film a-Si:H modules, where the substrate must be transparent and the front contact is made by a TCO (transparent conductive oxide) coated on the substrate (see Fig. 1.5). These configuration allows to tackle the material removal by laser backscribing process, this is carrying it out from the substrate side, commonly glass, as it is transparent with good thermo-physical properties and with a mature industry capable to provide the quality required for this technology [3, 13, 14].

Fig. 1.6a depicts the three laser steps to conclude the interconnection in superstrate configuration. The three steps (so-called P1, P2 and P3) for monolithic interconnection of solar cells within modules are nowadays defined by DPSS laser sources working at IR (λ= 1064 nm) and VIS (λ= 532 nm) wavelengths for thin film module fabrication. It is important to highlight again the backscribing configuration to carry out P2 and P3, where the laser comes into contact with the material through the glass substrate, restricting the latter to be transparent to the laser radiation.

The aim of this thesis is to carry out the interconnection by laser scribing in a different approach to the one described above. This thesis treats this interconnection in a different geometric approach (Fig.1.6b), whereas the backscribing laser processing tackles the P2 and P3 processes from the substrate side, obliging it to be transparent to the laser radiation, this work tries to accomplish all the laser steps involved in the interconnection from the film side. The laser process must be improved in order to

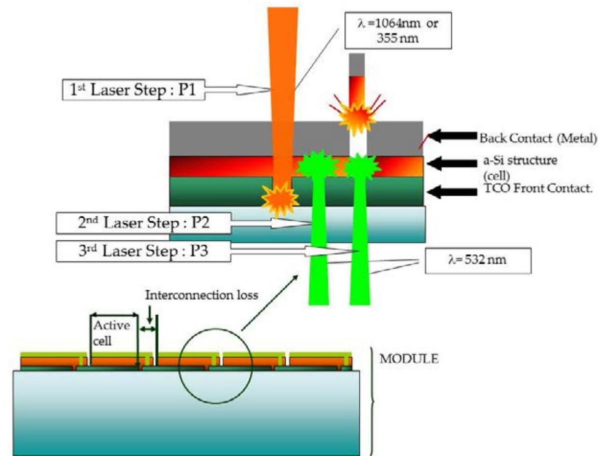

(a) Laser back scribing

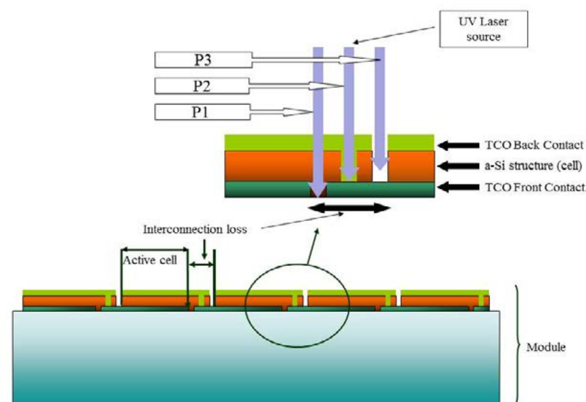

(b) Laser direct scribing

Figure 1.6: Laser monolithic interconnection for the two different structure configuration

minimize shunting problems which are closely related to the inherent thermal affection of laser irradiation at these wavelengths and nanosecond pulse duration. This work moves towards the possibility of performing the three laser steps with UV laser sources working at two different temporal ranges of pulse-width (nanosecond and picosecond) in order to eliminate the thermal affectation and performing the process from the film side, which makes the process suitable for the two different configurations (superstrate and substrate) and other kinds of technologies (CIS/CIGS, CdTe) including opaque substrates. Especially important is the picoseconds laser scribing evaluation, due to the lack of literature in this subject and the fact that these laser sources have become nowadays good industrial tools with high repetition rates, which allows the high processing speed required for industrial application.

2

Laser-Material Interaction

For a better understanding of the material removal from the surface of the targets by means of laser irradiation, it must be taken into account the physical mechanisms that governs the absorption of laser light by matter. These mechanisms are very complex and depend on the laser irradiance delivered into the target, the material properties and the laser parameters (wavelength, pulse width, polarization, intensity, spatial energy distribution, etc.). This chapter will describe these mechanisms bearing in mind the difficulty to show them in a very detailed description.

2.1 Laser Solid Interactions

The absorption of laser irradiation in the material is generally expressed in terms of the Beer-Lambert's law:

$$I(z) = I_0(1 - R)\exp(-\delta z) \tag{2.1}$$

where I(z) is the laser intensity (W/cm^2) at depth z, R is the surface reflectivity and δ is the material absorption coefficient (cm^{-1}). Normally δ is function of laser wavelength. According to equation 2.1 the intensity of the laser radiation gets attenuated inside the material. The length which laser reaches before being significantly attenuated is often referred to as optical penetration depth given by the reciprocal of the absorption coefficient:

$$l_{opt} = \delta^{-1} \tag{2.2}$$

As mentioned before the interaction mechanisms between laser light and matter depend on the parameters of the laser beam and the physical and chemical properties of the material. Coming to material response, in solids, light can interact with elementary electronic excitations that are optically active. Therefore, the laser-matter excitation is strongly dependent on the electronic band structure of the material. These excitations occurs differently attending at the type of material [4, 5, 7, 9].

For metals, there is no band gap since the valence band overlaps the conduction band and a significant fraction of the valence electrons can move through the material which are called free electrons. The optical absorption is governed by free-carrier absorption, which excites electrons in the conduction band to a higher-lying level by Inverse Bremsstrahlumg and gains energy from laser beam. Energy is subsequence transferred to lattice phonon by collision [54].

For semiconductors, the absorption of laser light predominantly occurs through resonant excitations such as transition of valence band electrons to the conduction bands (interband transition) or within bands (intersubband transition) seen in Fig. (2.1). These excited electronic states can then transfer energy to lattice phonons.

Photons with energy below the material band gap energy, E_g will not be absorbed (unless there are other impurity or defect states to couple to or if there is multi-photon absorption). When the energy of the photon exceeds the semiconductor band gap $\hbar\nu > E_g$, single-photon absorption could happen exciting a valence electron to the conduction band.

For higher laser frequencies, but still below that required for a single-photon absorption, the multi-photon absorption with simultaneous absorption of multiple photons by an electron can occur, the sum of the energy of all the photons absorbed must exceed the band gap energy, $n\hbar\nu > E_g$. Hence, multi-photon absorption requires n photons to interact simultaneously with a single electron. As photon density is proportional to laser intensity I, the probability for multi-photon absorption scales as I^n. As long as the laser field is present, this process repeats and the electron density in the conduction band grows exponentially.

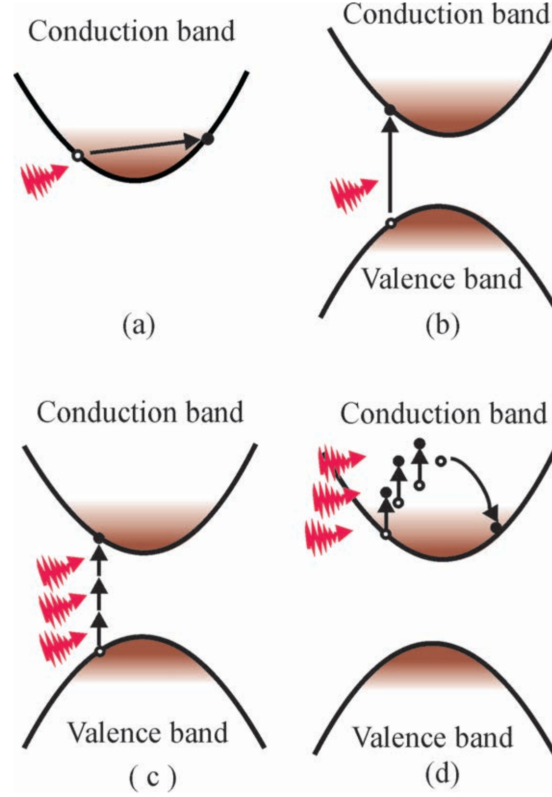

Figure 2.1: Laser excitation of electrons. The linear absorption including (a) free-carrier absorption (b) interband single-photon absorption. The non-linear optical process is found in (c) interband multi-photon absorption, (d) avalanche ionization [66].

As it has mentioned above, energy is transferred to the lattice by phonon emission and the temperature of the lattice is increased by carrier-carrier and carrier-phonon collisions. These phenomena occur simultaneously during the first few hundred femtosecond after excitation. When the thermal equilibrium of free carriers and the lattice is reached, in several picoseconds, the temperature of laser-excited material can be defined by conventional heat conduction means. After the thermalization, the spatial distribution of the energy can be characterized by the temperature profile. The generation of heat and its conduction into the material establish the temperature gradient, which is highly dependent on the applied pulse parameters and the thermo-physical properties of the material.

If the incident laser intensity is sufficiently high, the absorption of laser energy can result in the phase transformations of the target, such as melting and evaporation.

Generally, the phase transformations are associated with threshold (minimum) laser intensities, referred to as melting and evaporation thresholds. Melting and evaporation are efficient material removal mechanisms in many laser machining applications. Furthermore, the ionization of vapor during high laser intensity irradiation may lead to generation of plasma due to the growing of electron density. At this stage, mainly produced with nanosecond pulses, the high density plasma plume strongly absorbs the laser energy by free-carrier absorption changing the actual energy received by the surface. The plasma plume expansion could also lead to the generation of stress wave. On the other hand, the laser-matter interactions are associated with mechanical stress due to the thermal expansion or the propagation of shockwave, which could cause another kind of ablation form exhibits as spallation in case the amplitude exceeds the bounding strength of lattice in the target[10, 26].

2.2 Thermal Diffusion in Laser Irradiation

The above mentioned carrier excitation and energy exchange can be subdivided in several ultra-fast processes which have been depicted in Fig. 2.2. The carrier excitation happens at a time of several femtosecond order. The carrier-carrier and carrier-phonon energy coupling occurs in a time of sub-picosecond level, and heating of the lattice happens at approximately 50 $\sim$ 200 ps. Usually after a few tens of picosecond the relaxation of energy exchange between electrons and lattice will complete. The time to deposit the energy within these states is determined by the laser pulse duration [20]. Therefore, after the absorption of the laser radiation by the electrons, the energy is transferred to the lattice on a picosecond timescale. For nanosecond laser pulses, the laser can be considered a heat source and a one-temperature model is used to describe the heat regime within the target material [56]. In the case of ultrashort laser pulses, a two-temperature model is required to take into account that electrons and lattice have different temperatures [7]. Defining the characteristic time τ_c to describe the time required for the construction of thermal equilibrium between electron and lattice subsystems, as shown in Fig. 2.2, the general so-called short and ultra-short pulses can be separated by the characteristic time τ_c [66].

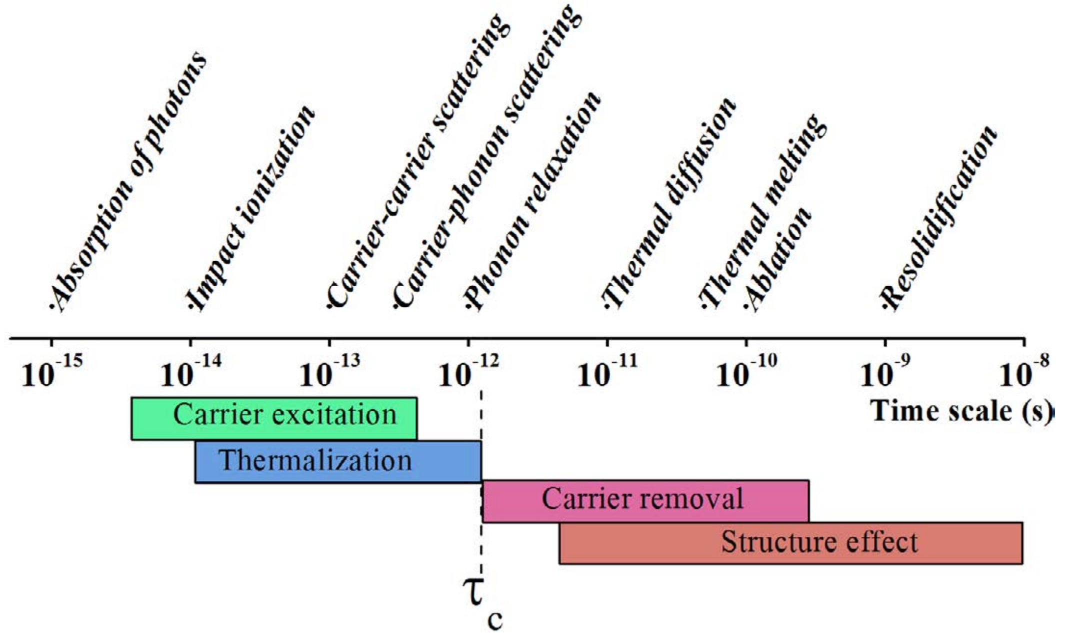

Figure 2.2: Different time scale in the laser excitation of materials [66]

In the regime where the pulse width is longer than the characteristic time $\tau_{las} > \tau_c$ (but still in nanosecond scale), although the laser radiation energy is transferred to the electron initially, the electrons coupling their energy to the lattice on a timescale shorter then the pulse width. Thus, the electrons and the lattice remain in thermal equilibrium and the thermal wave propagation is mainly due to the heat conduction by lattice. The spread in energy during the laser pulse combined with the spread in energy after the pulse can lead to changes in the material properties. The region over which these changes occur is denoted the heat affected zone (HAZ) and can exhibit a number of significant differences relative to the bulk material.

Typically the optical penetration depth l_{opt} (equation 2.2) is much smaller than lateral dimension, which is in the scale of laser spot size. Considering the absorbed laser energy as being directly transformed into heat, the material response can be treated in a purely thermal way. An important quantity that comes out of these simplified treatments is the thermal diffusion length [10]:

$$l_{th} = 2\sqrt{\chi\tau_{las}} \qquad (2.3)$$

where χ and τ_{laser} are the thermal diffusivity of the material and the laser pulse duration, respectively. The thermal diffusion length measures how far the energy spreads into the material during the laser irradiation. Therefore, laser temporal pulse length has a significant effect on the dynamics of the ablation process. In general, as the pulse length is shorted, energy is more rapidly deposited into the material leading to a more rapid material ejection. The volume of material that is directly excited by the laser has less time to transfer energy to the surrounding material before being ejected. Therefore, the ablated volume becomes more precisely defined by the lasers spatial profile and optical penetration depth, and the remaining material has less residual energy, which reduces the HAZ [45].

The damage threshold fluence, magnitude that will be treated in detail in next section, for a material reduces at shorter pulse lengths and becomes more sharply defined. However, even for these ultrashort pulses, there is excess energy remaining in the material that can still cause thermal effects in the surrounding material after the pulse has ended [34]. As it has been discussed before, another distinction of ns and ps ablation is that the laser material interaction is separated in time from material response and ejection. During nanosecond ablation, shielding of the surface by the ejected ablation plume can reduce the amount of energy absorbed by the material [69]. Fig. 2.3 illustrates the difference interaction with matter for short and ultrashort pulses.

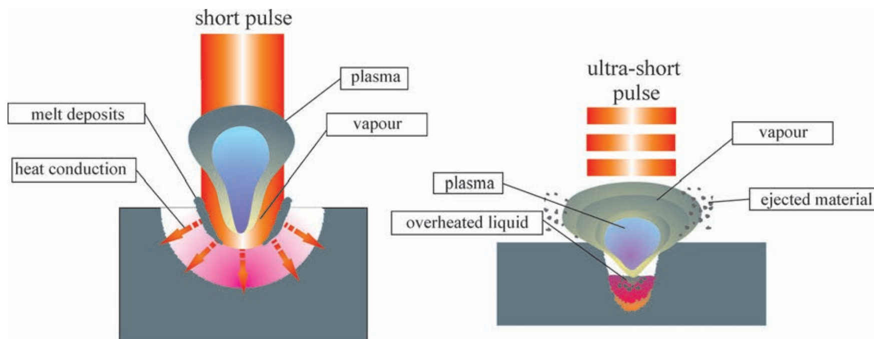

Figure 2.3: Laser-matter interaction attending to the pulse duration

2.3 Laser Damage Threshold Calculation

Laser ablation is the removal of material from a substrate by direct absorption of laser energy. The onset of ablation occurs above a threshold fluence, which will depend on the absorption mechanism, particular material properties, microstructure, morphology, the presence of defects, and on laser parameters such as wavelength and pulse duration as detailed above. The fluence threshold is measured by means of visual damage evaluation on the material surface as will be describe in following section 2.4. Owing to this matter and to avoid misunderstandings with other physical phenomena broadly studied in fundamental laser-matter interaction references, threshold fluence will be referred in this work as damage threshold.

With multiple pulses, the damage thresholds may decrease due to accumulation of defects. Above the damage threshold, thickness or volume of material removed per pulse typically shows a logarithmic increase with fluence according to the Beer−Lambert law (equation 2.1). This section describes the method used to calculate the damage threshold of the materials involved in this work.

The damage threshold is an important parameter to compare qualitatively interaction with laser between materials. In this section we will discuss the theoretical fundamentals for the damage threshold calculation taking into consideration the characteristics of the laser sources presented in this work. This threshold will take an important roll to unearth the proper parameters for the best development of the process.

As the laser sources used at this work has a spatial and time Gaussian distribution of its energy. The calculation method presented here is developed attending exclusively to Gaussian distribution.

Pulsed laser ablation is characterized by two parameters, the damage threshold fluence Φ_{Th}, that is, the minimum energy per unit surface required to ablate the material and the ablation rate Γ, which is the ablated depth per laser pulse. The latter depends naturally on the incident laser fluence Φ and on the material properties.

2.4 Damage Threshold Calculation for Energy Gaussian Distributions

In order to calculate the damage threshold when a pure gaussian energy distribution is assumed for our laser sources, the calculation is based on the well known work from J. M. Liu [44]. This method is based in the achievement of the damage threshold by the measurement of the craters diameter induced in the material by means of the laser light interaction with it, this crater or spot will be changed in dependence of different parameters such the energy per pulse, focus distance, material, etc. This method has been used largely by other groups [48] as a experimental way to determine the damage threshold for materials of interest.

Gaussian spatial and temporal laser pulses profiles follow the following formula to describe their intensity,

$$I(r,t) = I_0 \; exp\left(\frac{-r^2}{\omega_0^2}\right) \; exp\left(\frac{-t^2}{\tau^2}\right) \tag{2.4}$$

Where I_0 is the peak intensity, ω_0 and τ are the spatial radius and the temporal pulse-width at the ($1/e^2$) intensity contour, r is the radial coordinate of distance from the propagation axis, and t is the time variable.

The spatial distribution of the energy fluence is then given by,

$$\Phi(r) = \int_{-\infty}^{\infty} dtI(r,t) = \phi_0 \; exp\left(\frac{-2r^2}{\omega_0^2}\right) \tag{2.5}$$

Where $\Phi_0 = \sqrt{\pi}\;\tau I_0$ is the peak fluence at the centre of the beam. From this relation and making the appropriate calculation a relationship between the diameter and the fluence is obtained,

$$D^2 = 2\omega_0^2 \; ln\left(\frac{\Phi_0}{\Phi_{Th}}\right) \tag{2.6}$$

This equation is the based of the empirical method to determine the damage threshold for Gaussian beams. Which is able to be derived from an appropriate fitting of the experimental data. Then, considering the peak fluence as a function of the energy per pulse E_p:

$$\Phi_0 = \frac{2E_p}{\pi\omega_0^2} \tag{2.7}$$

equation 2.6 is related to E_p by

$$D^2 = -2\omega_0^2 \ \ln\left(\frac{\pi\omega_0\Phi_{Th}}{2}\right) + 2\omega_0^2 \ \ln\left(E_p\right) \tag{2.8}$$

The experimental calculations of the damage threshold will be presented in this work attending to this procedure. The diameter of the crater is measured and plotted as a function of its $\ln E_p$, obtaining the damage thresholds values Φ_{Th} for all the materials involved in this thesis.

In multi-pulse ablation, the damage threshold Φ_{Th} (N) can be determined in a similar way, corresponding to the relation D^2(N) and energy per pulse.

3

Materials and Methods

This chapter will describe the experimental methods employed in this work with respect to the laser process, deposition of the thin layers and the characterization techniques. The chapter has been divided in three fundamental parts, the first one describes the design and deposition of the samples, the second treats the laser systems used and the last one deals with the laser process characterization.

3.1 Design and Deposition of the Samples

In this thesis two types of samples have been processed. For studying the damage thresholds, single-layers of the materials which compose the devices have been deposited on glass. The deposition techniques for single-layers are the same than for the stacks of them that have been used for the laser scribing study; Table 3.1 shows in detail the characteristics of the samples, providing information about the stack scheme deposition, range of thickness of the analyzed samples, providers of the samples and the process evaluated with them. To study P2 and P3 laser scribing steps, non-finished and non-functional devices were deposited in order to evaluate the processes and achieve an optimal result to be prove in final devices.

The amorphous-silicon layers were deposited by PECVD (plasma-enhanced chemical-vapor deposition) in an MVSystems capacitive-coupled reactor yielding highly uniform films with thicknesses in the range 300-600 nm. PECVD is one of the main techniques for depositing hydrogenated amorphous Silicon (a-Si:H) at low temperatures (lower than 400° C) from a gas mixture with a process pressure between 100 and 100 mTorr

Samples		Thickness (nm)	Provider	Process evaluated
TCO	Glass/Asahi-U	∼ 600-800	Comercial	P1 , Φ_{Th}
	Glass/ITO	∼ 100-1000	Ciemat	
	Glass/AZO	∼ 100-1000	Ciemat, UB	
Glass/Al		∼ 150-400	Ciemat	Φ_{Th}
Glass/a-Si:H		∼ 200-500	Ciemat, UB	
Glass/Asahi-U/a-Si:H		∼ 200-400	Ciemat/T-Solar	P2
Glass/Asahi-U/a-Si:H/AZO		Unknown	Gadir	P3
		∼ 800/400/70	UB	
Glass/Asahi-U/a-Si:H/Al		∼ 800/300/150	T-Solar	P3
		880/420/120	Ciemat	

Table 3.1: Sample features used in this work

in a vacuum chamber. By applying a discharge through radiofrequency the silane gas is decomposed. The a-Si:H layer mainly used in this work has been deposited by the Group of Silicio Depositado from CIEMAT (Centro de Investigaciones Energéticas, Medioambientales y Tecnológicas) with the facility shown in Fig. 3.1.

Figure 3.1: PECVD system at CIEMAT facilities

To assess the TCO laser ablation, this work presents commercial TCO based on SnO_2:F(Asahi U-type), from now on Asahi-U, ITO (SnO_2:I_2O_3) and AZO (ZnO:Al).

ITO thin films were deposited by RF magnetron reactive sputtering using a *Leybold–Heräus* Z400 system. An (SnO_2:I_2O_3, 95/5-wt) target were sputtered with plasma obtained form an Ar/O_2 (95/5-vol) gas mixture. The deposition was carry out at room temperature.

AZO thin films were deposited on 10 cm x 10 cm Corning glass 7059 in a commercial MVSystems magnetron sputtering operating by RF power. The ceramic target for AZO was (ZnO:Al, 98-2 wt) with purity of 99.995% and a density of 6.6 g/cm^3. The target to substrate distance was kept at 84 mm and the base pressure and working pressure were 2.7 x 10^{-5} Pa and 0.7 Pa, respectively. The sputtering RF power was fixed at 60 W and the deposition was performed room temperature (RT) Fig. 3.2.

The deposition of the TCO samples was made again, thanks to the intimate collaboration with CIEMAT , they deposited a large extent of the samples used in this work.

Figure 3.2: RF sputtering plant using a MV Systems device at CIEMAT facilities

3.2 Laser Systems

Three DPSS lasers have been used throughout the experimental work presented here. All the systems have as active medium neodymium doped crystals where Nd^{+3} ions are trapped in a transparent solid. The excitation of Nd^{+3} ions provides the radiative emission of 1064 nm of wavelength. This study is centred in the third harmonic wavelength of such fundamental radiation, that is 355 nm of wavelength in the UV range when the frequency is tripled by non-linear optics. As this thesis is centred in UV laser processes the main wavelength of the laser used was 355 nm as it will be described in detail below. Some works with the fundamental wavelength at 1064 nm have been made in order to compare the influence of the wavelength in the laser scribing process. The laser systems employed in this thesis are detailed as follow,

3.2.1 355 nm Nanosecond Laser Set-up

The laser source of the system is a diode pumped, Q-switched laser with $Nd:YVO_4$ (Vanadate) lasing media crystal (HIPPO SPECTRA PHYSICS). The system comprises three elements: the HIPPO $Nd:YVO_4$ laser head, model J80 air-cooled power supply and a chiller for cooling the laser head.

The laser head provides Gaussian beam 1064 nm output alone and include an harmonic tripled module which is attached to the output end of the laser for 355 nm output. To generate high energy pulses, two high-powered acousto-optic Q-switches are place in the cavity to act as switches to turn the laser on and off from 15 KHz to 300 KHz.

The data specifications of the laser source are shown in table 3.2, along with the typical performance data for 355 nm at different frequencies shown by the graph shown in Fig. 3.3.

HIPPO SPECTRA PHYSICS	
Average Power	5 W at 50 KHz
Repetition rate	15 - 300 KHz
Pulse-width nominal	<12ns at 50 KHz
Mode	TEM_{00}
Polarization	> 100:1, vertical

Table 3.2: Laser specifications of HIPPO SPECTRA PHYSICS system for 355 nm of wavelength

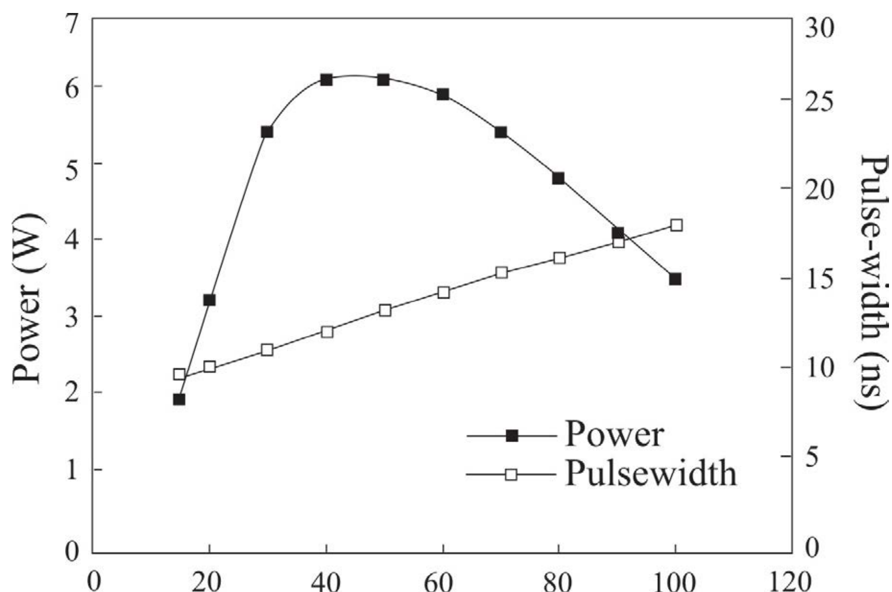

Figure 3.3: Typical performance data for HIPPO laser source at different frequencies

System control is provided by a graphical user interface (J-WIN software) that contains controls and displays for monitoring and controlling the laser system. This software allows to control the frequency of the system and current supplied to the the pump diodes, which determines the final output power. For the study performed in this work, maximum power at different frequencies were set, due to the fact that this laser sources generally has an unwanted side-effect on beam profile when the power is made by internal control. To avoid this problems and additional stability problems a programmable laser beam attenuator (AT4040 OPTEC) is set in the system to control the output power. This device works by shifting in cut-off wavelength which occurs when a multi-layer dielectric high-pass edge filter is tilted with respect to the beam.

The transmission reduces progressively with tilt angle in a non-linear fashion from 95 % to a low value typically < 5 % at 45° tilt.

The power monitoring is made in two places, the output from the laser head is sampled using a beam splitter and photodiode that are placed between the output coupler and the end of the laser, an additional measurement of the power is made at the end of the optic path, just before the sample to be processed, this monitoring is made by a commercial power meter (OPHIR Model Laserstar) with a photodiode head. The beam is delivered to the working area via steering mirrors which direct the beam to a scanner head (Hurrycan II 14 SCANLAB) via the power attenuator AT4040 see Fig. 3.4. Before the entrance of the scanner head an iris is placed in order to remove the diffraction and aberration defects of the laser beam. The scanner head directs and focuses the beam onto the target via a lens with a focal length of 250 mm.

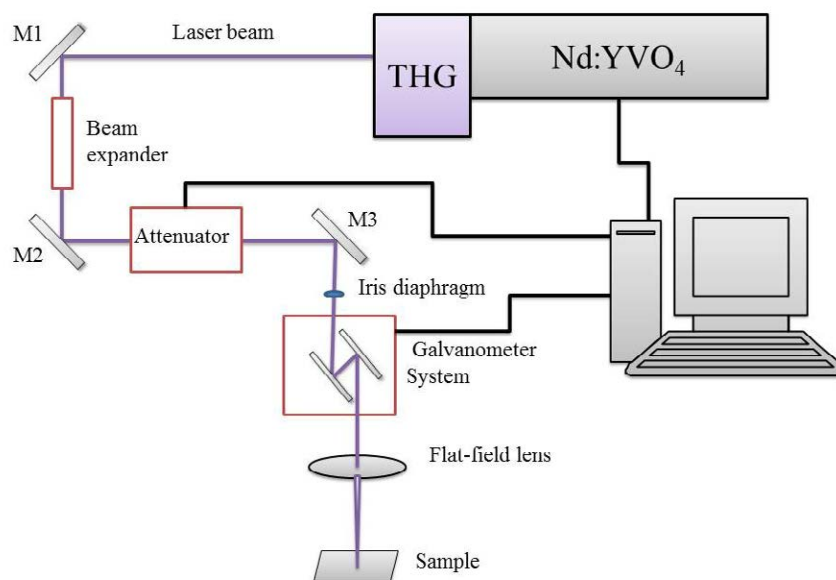

Figure 3.4: HIPPO setup scheme

3.2.2 355 nm Picosecond Laser Set-up

For the picosecond irradiation a Innolas ILS500 X system has been used. The system integrates a SUPER RAPID laser source from LUMERA LASER consisting in a mode-locked oscillator, a fast electro-optic pulse picker, an amplifier and a harmonic

LUMERA SUPER RAPID			
Frequency	**Average power (W)**		
kHz	1064 nm	532 nm	355 nm
100	12	8	4
200	14	8	4
500	15	6	3
1000	18	4	1.5

Table 3.3: Laser specifications of LUMERA SUPER RAPID system.

generator module which delivers Gaussian beam for the second (corresponding to a wavelength of 532 nm) and third harmonic (corresponding to a wavelength of 355 nm). The laser head is a rugged monolithic aluminium structure and is actively temperature controlled. The oscillator is a diode-pumped passively modelocked solid state Nd:YVO_4 laser with a repetition rate of 50 MHz, with a typical pulse width of 8 ps. The fast electro-optic pulse picker selects a number of pulses out of the picosecond pulse-train to reduce the effective pulse rate. The laser is equipped with a Second and Third Harmonic Generation Module. The frequency conversion into the green spectral region (SHG, Sencond Harmonic Generation) is present in nonlinear optical crystals. Third Harmonic Generation (THG) is produced by nonlinear crystal which converts the doubled radiation and the residual infrared radiation (1064 nm) to ultraviolet laser radiation with a wavelength of 355 nm by sum-frequency-mixing. The selected pulses will be amplified to obtain the required energy. The pulse picker provides single pulses at repetition rates from 0 to 500 kHz and group of pulses repeated from 0 to 500 kHz. The amplifier uses the same gain material as the oscillator, Nd:YVO_4 , which is well known for a high gain cross section leading to a very high amplification. The energy of a ps pulse is increased form 60 nJ ($\sim$ 3W, 50W) to a maximum of more 30μJ (repetition rate $\leq$ 10 kHz).

The data specifications of the laser source are shown in the table 3.3.

The system is equipped with high precision XY-table which utilizes precise linear motors and high-resolution glass scales for each axis combine with a vision recognition system that provides laser positioning accuracy to within a few microns.The system also includes a high speed laser scanner head for the three wavelengths of operation and the possibility to work with a short focal length optic with process gas nozzle.

System also has an in-situ laser power meter, which can monitor the power before each process.

The system control is provided by a graphical user interface that contains controls and displays for monitoring and controlling the laser system along with the movement of the axis and the scanner heads Fig. 3.5 provides a visual information of the scheme set-up.

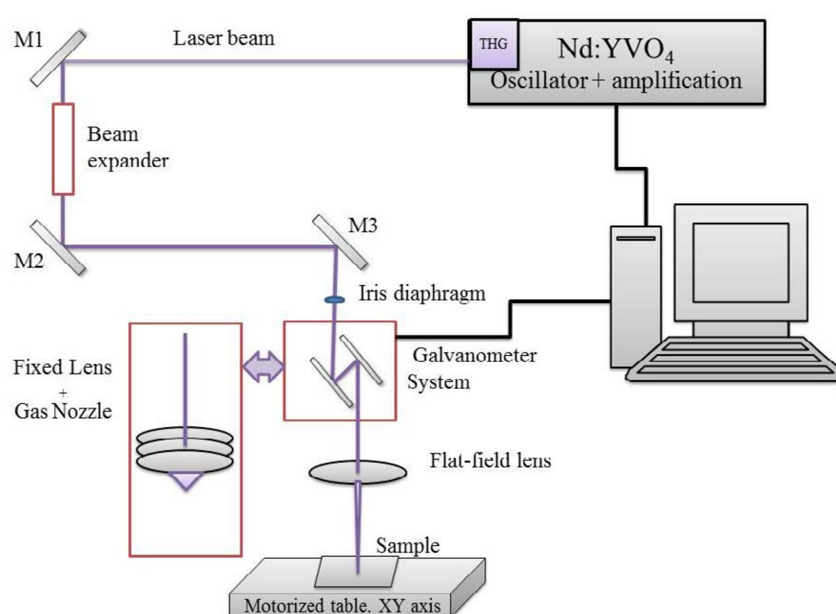

Figure 3.5: Innolas set-up scheme

3.3 Laser Scribing Characterization

3.3.1 Scanning Electron Microscope (SEM) and EDX (Energy Dispersive X-Ray) Spectroscopy Analysis

In order to have a complete characterization of the laser patterning processes presented in this work, SEM images and specially EDX analysis plays a main role when the selective ablation takes place. The only way to assure the complete selective ablation process is via EDX analysis as it will describe below in this section. SEM images will give a good view of the surface after ablation process and EDX analysis will provide

information about the quantity of material removal achieve by the same as long as the state of damage of the substrate.

SEM permits the observation and characterization of a wide variety of materials on a nanometer (nm) to micrometer (μm) scale. In the SEM, the area to be examined or the microvolume to be analyzed is irradiated with a finely focused electron beam, which may be swept in a raster across the surface of the specimen to form images or may be static to obtain an analysis at one position. The types of signals produced from the interaction of the electron beam with the sample include secondary electrons (SE), backscattered electrons (BSE), characteristic X-rays, and other photons of various energies. These signals are obtain from specific emission volumes within the sample and can be used to examine many characteristic of the sample (surface topography, composition, etc). Backscattered and secondary electrons, the principal signals used to form images in scanning electron microscopy, are generated within the interaction volume. These signals are capable of carrying information about specimen composition, shape (topography), local fine-scale surface texture, thickness, and local inclination to the incident beam.

Both secondary electron images (SE) and backscattered electron images (BSE) are routinely obtained. In backscattered mode, a simplest contrast mechanism, compositional contrast, arises from differences in the local chemical composition within an object under study. This mechanism conveys the type of information we normally obtain optically with colour, that is, differences in colour are often the result of differences in composition. Compositional contrast is principally a BSE number contrast mechanism, with a component of energy dependence.

With characteristic X-rays, and by means of an Energy Dispersive X-ray Analysis (EDX) data can be acquired at predetermined intervals and then correlated to specific features on the image. This system also allows EDX quantitative mapping software that permits an accurate display of elemental distribution without concern for spectral peak overlap. The maps accurately depict the weight percents within the elemental distribution. Line scans can provide quantitative data across a line profile of the sample. Area scans that can be varied in size or a spot analysis can be performed to obtain the elemental composition at a specified location. In addition, those locations can be referenced directly on the SEM image. Fig. 3.6 illustrates the different techniques obtained with this equipment.

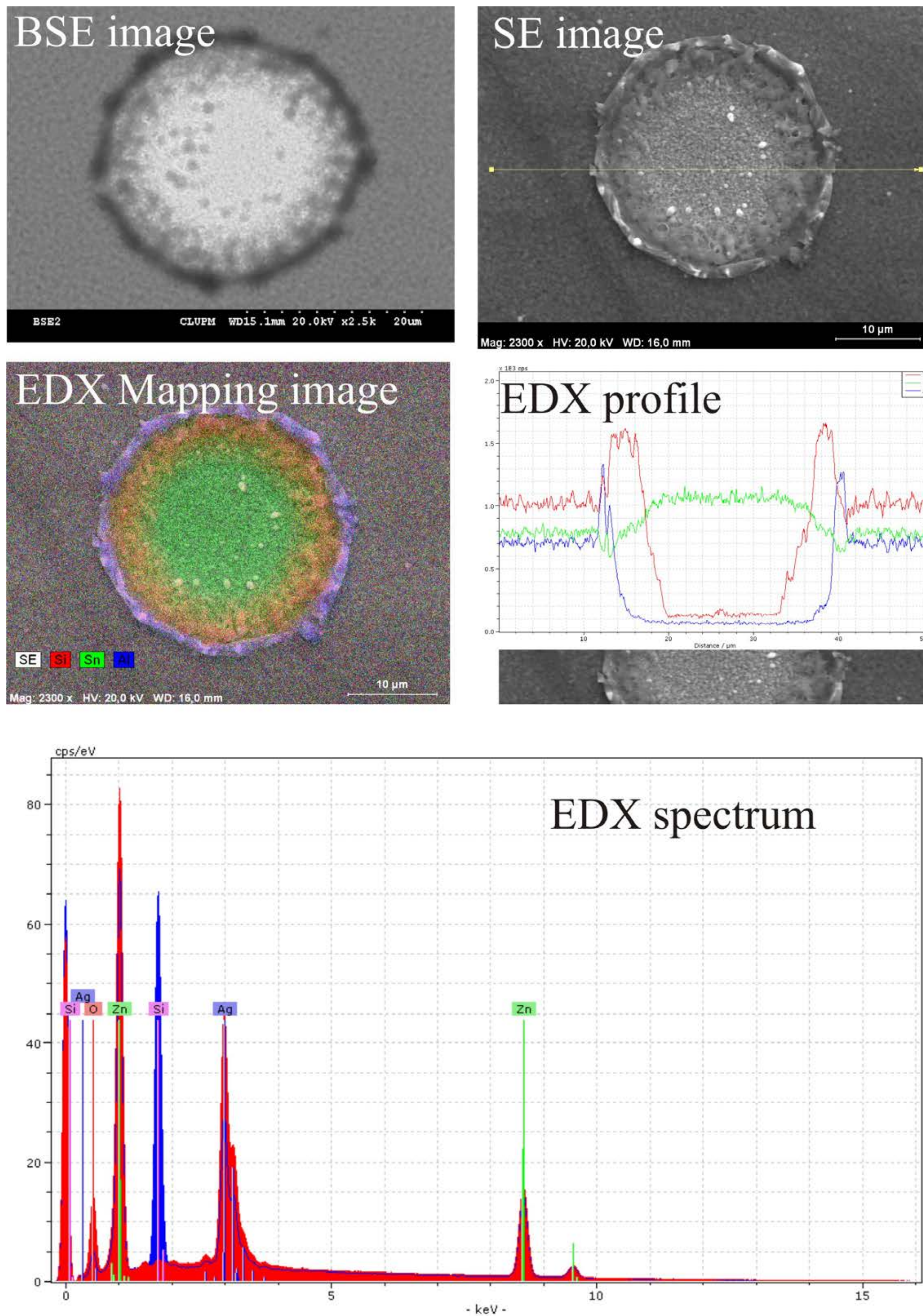

Figure 3.6: Techniques obtained with the SEM EDX system available at Centro Laser UPM

The images shown in this work have been acquired with a Hitachi S-3000N available in the Centro Láser UPM. This system can be used to analyze materials at voltages between 1-30 kV and at pressures ranging from <1 Pa to 270 Pa.

3.3.2 Confocal Laser Scanning Microscopy

Confocal laser scanning microscopy has became in a powerful instrument as a characterization technique in material science, since this instrument is capable to construct three-dimensional (3D) images. By means of a non-invasive serial optical slicing 3D images are performed. It allows profiling of the surfaces of 3D objects and multi-layer structures such as the solar cells treat in this work by a non-contacting and non-destructive method.

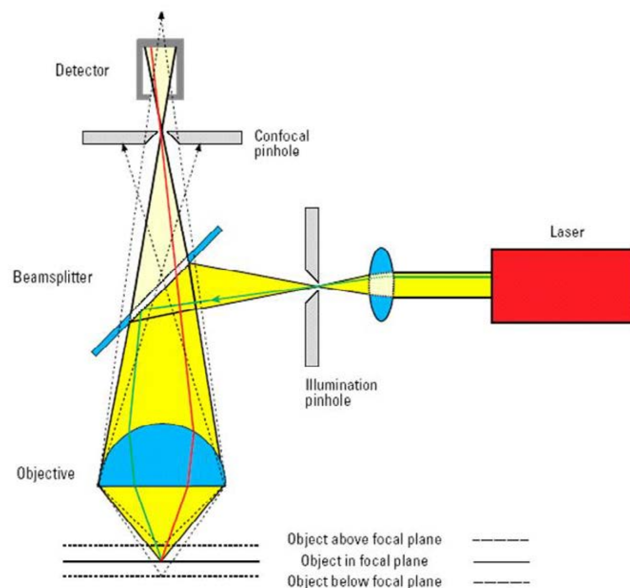

Figure 3.7: Confocal squeme

In Fig. 3.7 the confocal configuration is shown. The principle behind CLSM is to scan a focused laser beam inside a sample and collect the reflected or emitted light from the sample, while removing any light originating from outside of the focal point of the laser beam. Much of the light collected by the objective lens to form the image will thus come from regions of the specimen above and below the selected focal plane,

contributing as out-of-focus blur to the final image, and seriously degrading it by reducing contrast and sharpness. Collecting individual slices in the xy plane, for example, with small steps in the z-direction provides all the information necessary to perform a 3-D reconstruction of the interior of a sample nondestructively. The Centro Laser was pioneer in the use of these instruments for material science characterization, as it had the first confocal microscope for this purpose in Spain. Combining this technique with SEM and EDX techniques allows better assessment of the laser scribing morphology as can be seen in Fig.3.8.

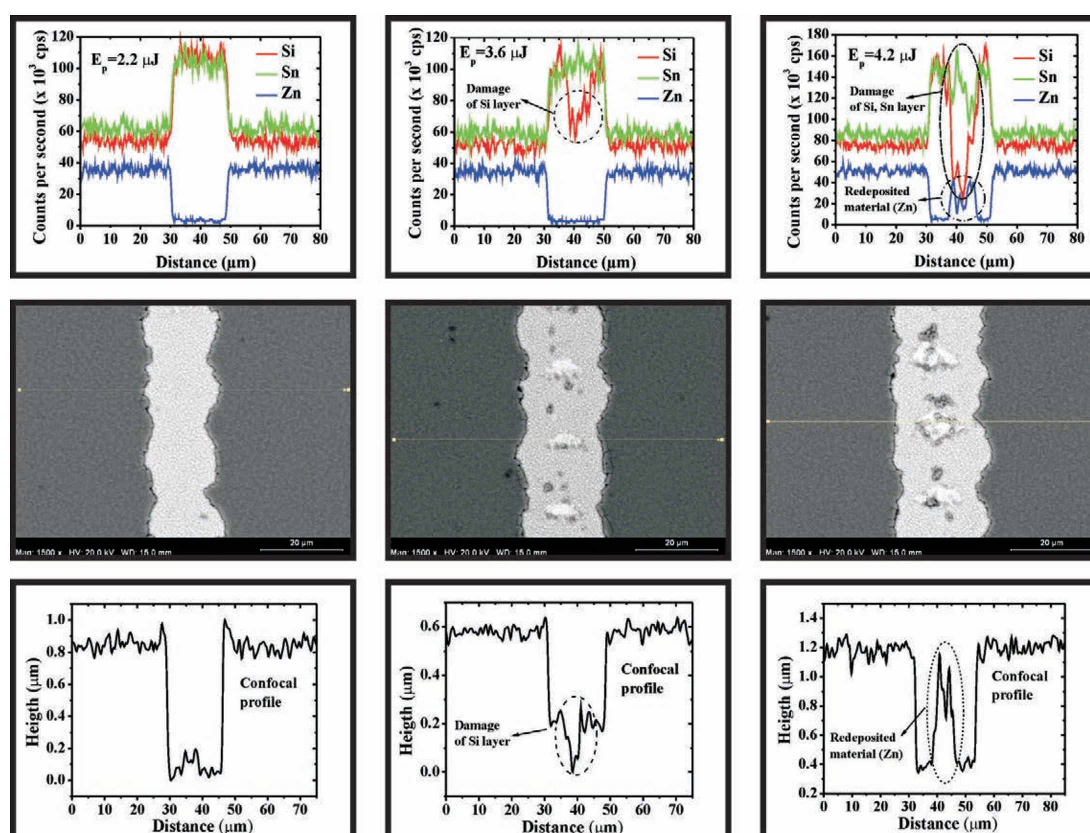

Figure 3.8: Combination of three techniques in scribing morphology evaluation

In this work topographical images and profiles have been obtained with a Confocal Laser Scanning Microscope (Leica ICM 1000). The equipment operation wavelength (635 nm corresponding to diode laser emission) together with the objective numerical aperture and pinhole diameter gives final resolution in axial direction. In confocal microscopic techniques, 3D images are obtained moving the focus plane and acquiring

single images (optical slices) that can be put together building up a three dimensional stack of images that can be digitally processed. Expected accuracy in step measurements is about 50 nm that correspond to theoretical calculations according objective specifications, however global accuracy in Z measurements is strongly dependent on sample optical reflectivity. Higher reflectivities give better step measurement accuracy, so the previous value must be considered a reasonable approach taking into account optical behaviour of materials studied. Fig. 3.9 shows a 3-D reconstruction of an ablated groove and the section used for profile measurement.

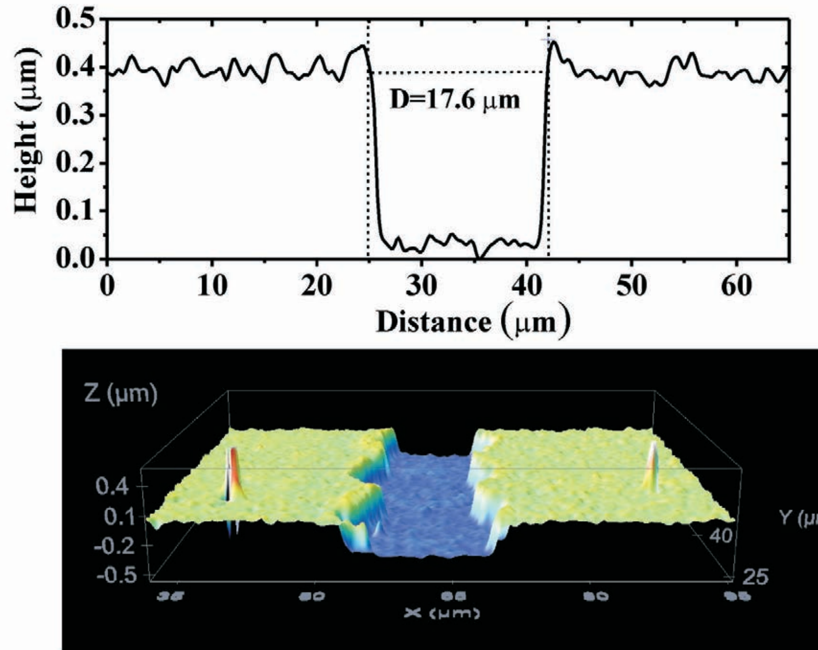

Figure 3.9: 3-D confocal topographical reconstruction with its corresponding profile

3.3.3 Raman Spectroscopy

Regarding conditions of the remaining material after laser irradiation for P2 and P3 steps, there are some experimental evidences supporting the formation of a heat affected zone,where an increased defect density and microstructural modifications of the intrinsic material seem to be induced due to thermal effects [55]. Although thermal effects are mostly associated to the use of ns regime lasers, the generation and expansion of this heat affected zone also depend on other laser radiation parameters, such as wavelength,

repetition frequency, pulse energy spatial distribution and, obviously, pulse energy. Furthermore, it is widely accepted that crystallization of a-Si:H can be induced by means of ultraviolet radiation, with Excimer Laser Crystallization techniques being well known for this purpose [32, 71]. In addition, some evidences of a-Si:H crystallization by means of green laser irradiation have been also recently reported [57, 70]. On this basis, microstructural alterations of the material closest to the ablated groove could be also expected when using 355 nm wavelength lasers with pulse duration in the ns range. Such modifications could lead to an increased crystalline phase resulting in the reduction of the intrinsic material electrical resistance [65]. Hence, the material in such region might behave as a leak path, degrading electrical properties of the device. Due to the high spatial resolution of Raman spectroscopy, regions with morphological modifications (closest to the groove edges) could be also studied with this technique [59].

Micro-Raman spectroscopy, or Raman microscopy, is a powerful analytical technique based on the analysis of the inelastic scattering of light interacting with the material under test. This technique provides spectra characteristic of molecular vibrations (or of phonons in solids) that can be used for sample identification and/or phase quantification. A Raman spectrum represents the intensity of the scattered light as a function of the shift in frequency (i.e. energy) from the excitation light frequency. This "Raman shift" is directly linked to the vibrational energy of the bonds between the atoms within the probed material. More specifically, in the case of silicon thin films, Raman spectroscopy is particularly well suited to discriminate between the amorphous and the crystalline phase of samples processed with laser.

The deconvolution of Raman spectra that yields quantitative information regarding crystallinity can, thus, be correlated to the material damage by means of the heat affected zone generated during the laser scribing. In that sense, due to the high temperatures reached by the a-Si:H layer during the interconnection steps (P2 and P3), a heat affected zone, mostly associated with morphological changes induced in the material, could be generated around the ablated portion.

The different phases (amorphous or crystalline material) present in a a-Si:H sample processed with laser result in different peaks on a Raman spectrum. This Raman signal collected in the micro-Raman experiment is dependent on the depth distribution of each phase. The relative proportion of each peak attributed to the amorphous and (micro-)

crystalline phases on the Raman spectra of a silicon thin-film sample can, thus, be considered as being an indication of the crystallinity of the volume probed within the sample.

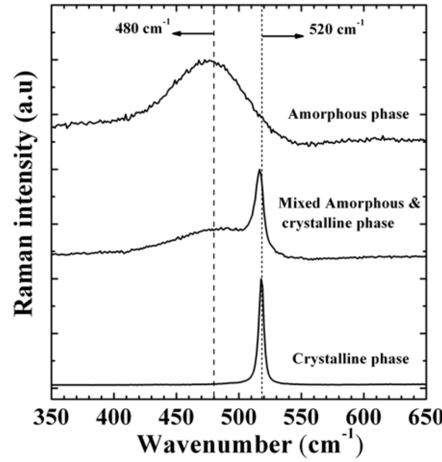

Figure 3.10: Examples of Raman spectra taken on our set up for different phases of the silicon in a thin layer

Fig. 3.10 shows typical Raman spectra corresponding to crystalline phase (c) exhibits a narrow peak centred at 520 cm^{-}1 characteristic of the transverse optics (TO) mode of the crystalline silicon phase . The Raman spectrum of an a-Si:H layer (Fig. 3.10 (a)) exhibits a broad peak centred at 480 cm-1. This is characteristic of the TO mode of the amorphous silicon phase. The middle spectrum corresponds to the mixture of the two phases (b).

The experimental set-up used throughout this work for collecting Raman spectra is the compact Renishaw Raman Imaging Microscope, system inVia. This system consists of a laser source for illuminating the sample and exciting Raman scattering, this system is equipped with an Argon laser (Spectra-Physics 163-M42-010) emitting at a wavelength of 514 nm (green light) and a Raman spectrometer where its lower part expands and directs the excitation laser beam to the microscope. Subsequently, the upper part processes the signal collected from the sample. Finally, signal detection is achieved through the use of a sensitive charge coupled device (CCD) array detector that is thermo-electrically cooled. The microscope can be used either as a common

instrument for observing samples or as the interface between the spectrometer and the sample during Raman measurements. It focuses the excitation beam onto the sample through an objective and then collects the backscattered light by the same way. For Raman measurements both 50X and 100X standard objectives were used along with Long Working Distance (LWD) of 50X magnification, that enable Raman measurements on the bottom side of thin films deposited on glass. The focused laser beam diameter is about 1 μm with a 100X objective. Data acquired from the CCD are read, stored and processed by computer, which also controls all spectrometer functions.

The excitation radiation could induce crystallization of a-Si:H thin films depending on the power density employed. In order to prevent this effect, and previous to the Raman analysis in the area of interest (vicinity of the groove), different laser powers were tested in a zone far from the ablated area, where the material was known to exhibit a completely amorphous character. The power of the light arriving on the sample has been varied by changing the transmission of the ND (Neutral Density) filter from 1 % to 100 %. Fig. 3.11 shows Raman spectra acquired on an amorphous sample and measured at different laser powers, recrystallisation on the probed volume is observed for an incident 50% of the power. The spectra recorded with the two lower laser power values (1%, 5% and 10 %) revealed a broad peak centred at 480 cm^{-1} characteristic of a-Si:H . Although, the 1% of power presents a large amount of noise. The spectra acquired with 50 and 100% of the laser power also presented this amorphous characteristic peak, in this case a peak center at about 500 cm^{-1}. Given these results, the power selected for the measurements in the surrounding of the laser groove was 5% of the power. As the aim of Raman measurements is to evaluate the crystallinity, the excitation light power must be lower than the threshold value over which recrystallization occurs. Taking into account the noise found at lower powers, there must be a compromise between a sufficient power to acquire good signal and any recrystallization effect.

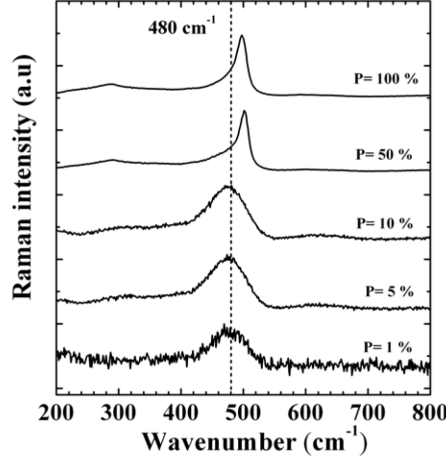

Figure 3.11: Effect of excitation light power (P) on the Raman spectrum of an a-Si:H sample

The Raman spectra give us qualitative information. Indeed, the relative heights of the amorphous and crystalline peaks enable us to compare the degree of crystallinity corresponding to different spectra. Although this qualitative information is relevant, to extract a quantitative value of the crystallinity from the Raman spectrum gives the possibility to compare the different measurements as it will explain in more detail bellow.

In order to get this additional quantitative information, Raman crystallinity fraction, ϕ_c, can be evaluated form the deconvoluted Raman spectra as the ratio of the area under those peaks related to crystalline parts over the total area of the silicon related peaks:

$$\phi_c = (I_{520} + I_{510})/(I_{520} + I_{510} + I_{480}) \tag{3.1}$$

where I_i is the area under the Gaussian centered at i (520 cm^{-1} corresponds to crystalline phase, 510 cm^{-1} corresponds to the defective crystalline phase and 480 cm^{-1} corresponds to the amorphous phase) see Fig. 3.12. This factor does not reflect the actual crystalline volume fraction but is simply a ratio of Raman intensities that can be used only for comparison purposes [64]. The calculation of the crystalline volume fraction from Raman spectra requires the knowledge of the effective cross-section for

both amorphous and crystalline material, which depends on the size of the crystallites [15], [46], assumed here as y=1 since it is unknown for our samples. Due to the high spatial resolution of Raman spectroscopy, regions with morphological modifications (in our work, closest to the groove edges) can be studied with this technique. In this work the Raman spectra deconvolution was performed by the fit of the peaks described before.

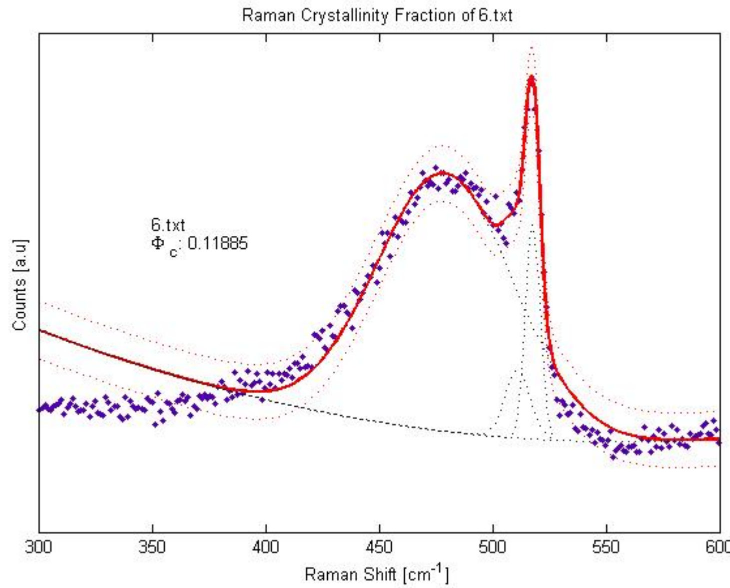

Figure 3.12: Raman spectrum and peak deconvolution of a-Si:H

3.3.4 IR-VIS Spectrometry

The characterization of the refractive index, n, is a powerful tool since its variations are known to be indicative of modifications in the microstructure of the material [41]. Refractometric detection is widely used in several research fields such as semiconductor technology for monitoring different fabrication steps [42], in liquid sensing [31], or in label-free biosensing [43], among others. Thus, the "n" characterization was used for the microstructural evaluation of a Si:H layers after the realization of laser treatments, whose conditions were equivalent to those used in the conventional P2 and P3 patterning steps. Although damage could be induced during both P2 and P3 steps, the influence on the electrical properties of the device would be much more critical after a P3 step than after a P2 one. The inspection of the p-i-n structure after the P3 step is difficult due to

the presence of the back contact layer. Hence, an alternative approach to characterize a P3 step was used for the evaluation of an a-Si:H layer exposed to a laser treatment equivalent to that used in a conventional P3 process [52].

A high resolution IR-VIS Fourier transform spectrometer (Bruker Vertex 70 with Hyperion microscope) was used for the measurement of a-Si:H thin film transmittance spectra. Measurements were carried out before (reference spectra) and after the laser ablation processing. Transmittance spectra were acquired by illuminating with a tungsten lamp through a rectangular area (300x2 μm^2). This area was determined by a variable edge aperture of the microscope.

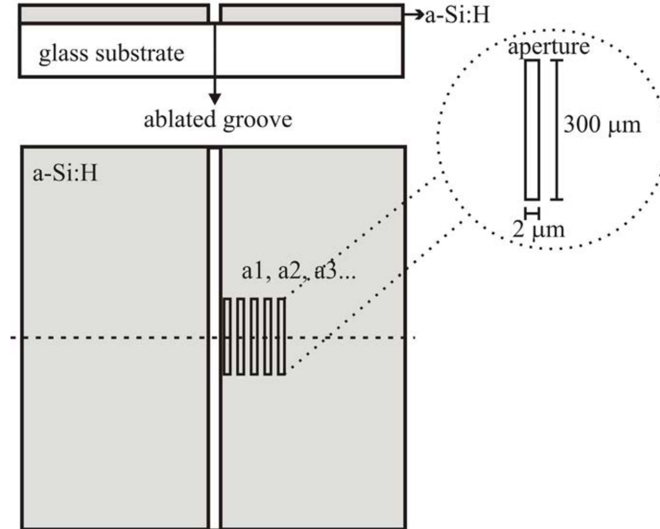

Figure 3.13: Schematic diagram showing sample structure and measurement procedure performed for the acquisition of the transmittance spectra.

The methodology is based on the analysis of an enclosed region, in which the average refractive index variation at different distances from the ablated groove is measured. A schematic diagram of the transmittance measurement procedure is also included in Fig. 3.13. This diagram shows an imaginary line in the middle of the sample, which is perpendicular to the laser groove and, which is used as a reference for the measurements. The aperture orientation with respect to the reference line and the laser groove can be also observed in Fig. 3.13. Distance between measures (a1, a2, a3 ...) depended on whether the spectra were acquired before or after the ablation process. The spectral range analyzed was from 600 to 1000 nm. In such range, two transmittance peaks are

clearly observed (see Fig. 3.14). In order to get additional insight into the crystalline structure of the material in the vicinity of the laser patterned area.

The use of the microscope allows us to measure the transmittance in micro domains of the thin film. By using an edge aperture of 2 μm width, different transmittance spectra were obtained at different positions with respect to the center of the sample, before and after the laser treatment. For measurements made after the laser treatment, transmittance spectra were acquired from the zone of the edges where the a-Si:H layer was uniform in thickness without morphological modifications and where the amount of material debris was small in comparison to the measured area (300x2μm^2).

It is also important to mention that transmission results of thin film structures as those under study depend strongly on thickness uniformity. For this reason, the effect of the thickness uniformity on the resulting transmittance spectra for the two samples was evaluated before laser scribing 3.14(a).

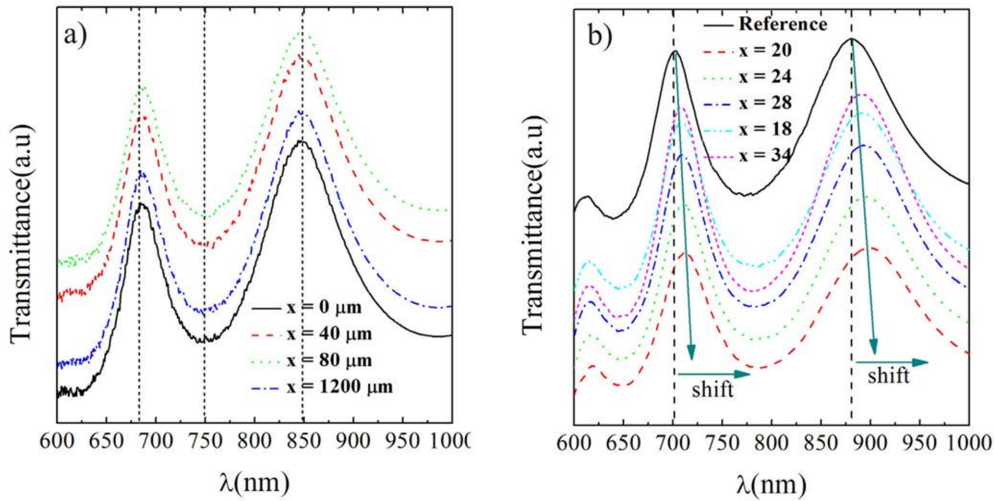

Figure 3.14: Transmittance spectra, measured at different positions (x) from the center of the a-Si:H sample: (a) before and (b) after a laser direct-scribing treatment. Reference corresponds to the spectrum acquired at x=0 mm before the laser process.

All the shown spectra present two interference peaks, whose position is very similar for all the x range evaluated. Consequently, it can be affirmed that, at least in the samples under study, the thickness non uniformities (standard deviation of 12 nm in a

size area of 3.4 cm^2) do not have a significant effect on resulting spectra.

Regarding the properties observed after the laser patterning process, 3.14 (b) shows transmittance spectra obtained at different positions with respect to the edge of the laser groove, x = 0, and corresponding to the sample treated by laser direct-scribing. A reference transmittance spectrum (REF) of the same sample acquired before the laser treatment is also included. A slight shift of the interference peaks with respect to the untreated sample can be distinguished. Such result gives evidence of changes in the refractive index, n, of the a-Si:H layer and, consequently, in its structure features as shown below. All the measured spectra exhibited two interference peaks, whose position was shifted towards higher wavelengths when approaching the edge of the patterned groove, indicating a higher refractive index.

These transmission spectra (Fig. 3.14(b)) allowed us to calculate the variation of the a-Si:H refractive index, Δn, as a function of the distance. The effective refractive index calculations were obtained with the transmission profiles and Fresnel equations of a layer of a-Si:H over a glass substrate by using a thin layer interference model to calculate the refractive index variation, Δn, in (arb. units) as a function of the peaks shift, $\Delta\lambda$, in nm [42]. Hence, given the thickness of the a-Si:H layer, the transmittance spectra can be theoretically determined. Consequently, it is possible to simulate different transmittance spectra supposing slight variations in the refractive index of the a Si:H layer. On this basis, the dependence of the peak position on the refractive index in the resulting theoretical transmission spectra can be easily estimated [31],[27]. Thus, the ratio of the Δn and $\Delta\lambda_{peak}$ variation is estimated in 0.00455 arb. units/nm for the peak centered around 870 nm and 0.00576 arb. units/nm for the peak centered around 720 nm.

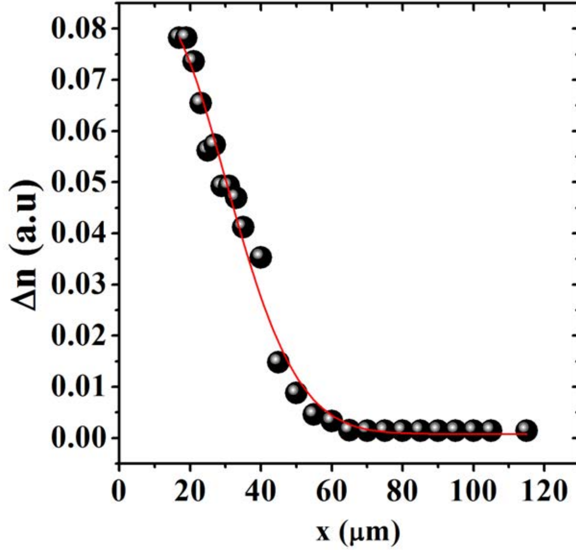

Figure 3.15: Variation of the refractive index as a function of the distance from the groove center

The variation of the refractive index as a function of the distance from the groove center, x, is shown in Fig. 3.15. where a Gaussian trend of the experimental data can be deduced. Consequently,the graph presents the data fitted to the following Gaussian expression:

$$\Delta n = A \exp(-x^2/2\omega^2) \tag{3.2}$$

where A is the amplitude of the Gaussian function and ω is related to the width of the Gaussian curve, so that 2ω is the distance from the center of the groove where δn is reduced by a factor of e^2 from its maximum amplitude (A).

Fig. 3.16 shows a schematic diagram where the relation between the fitting Gaussian function and the characteristic lengths of the groove and the surrounding affected materials is shown. It is also important to remark that transmittance spectra measurements were carried out form the area closet to the groove edges where a homogeneous appearance could be ensured over the whole analyzed area. This procedure was used to avoid the irregularities at the edges, which might have led to unreliable transmittance values due to the influence of ablated regions and re-solidified material.

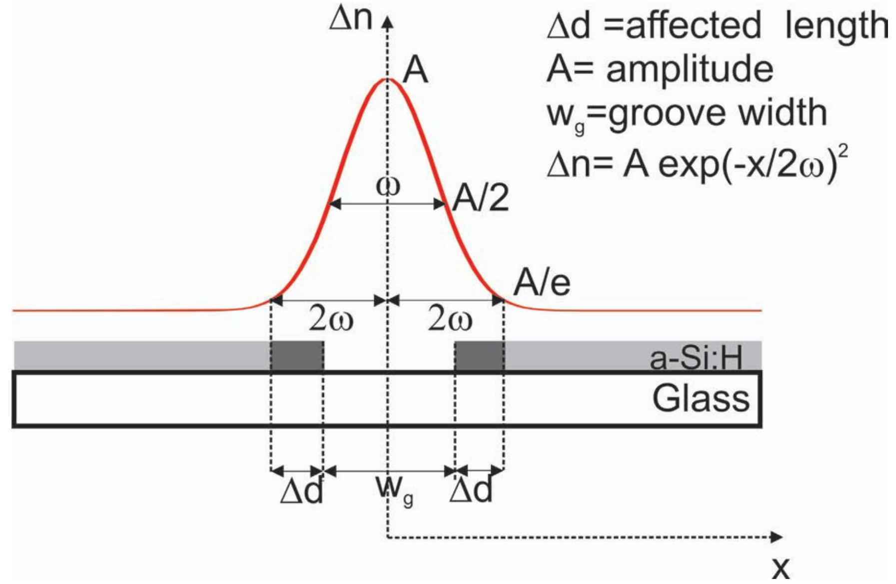

Figure 3.16: Model showing the relation between the Gaussian fit of the refraction index variation and laser groove characteristics lengths for laser treated a-Si:H layers.

In order to analyze the obtained results, mechanisms including the decrease in hydrogen concentration , changes in void structure, and network reorganization [21], which are in fact correlated, must be considered. In that sense, it is widely accepted that during laser annealing of a-Si:H , hydrogen released from the films forms bubbles which can explode, eventually leading to an ablation of the film [63],[50].

Additionally, crystallization of a-Si:H films is also related to the release of hydrogen atoms from the network, which is achieved by breaking the Si-H bonds. These bonds lead to the formation of many disordered domains, making the film more porous by increasing its structural heterogeneity. As a consequence, a more dense and ordered network has been observed by reducing Si-H bonds [38]. On the other hand, it is known that the increase of the refractive index is associated with network densification [57],[22]. Accordingly, and increase in the refractive index of a-Si:H layers can be induced by reducing its hydrogen concentration, thus leading to a more dense and ordered material.

3.3.5 Electrical Characterization

In this work, electrical measurements via J-V characterization will help to assess the damage introduced by laser monolithic interconnection on the modules electrical per-

formance. At first approximation in a cell, and later with the evaluation of a complete interconnected module.

The electrical characterization has been performed with a system composed by a computer-programmed Keithley 2420 source/meter. The devices were illuminated with a Newport Oriel class A solar simulator, which simulated the AM 1.5G sunlight (100 mW cm^{-2}) and was certified to the JIS C 8912 standard. The light source was also calibrated with a standard silicon photodiode (Hammamatsu S1133).

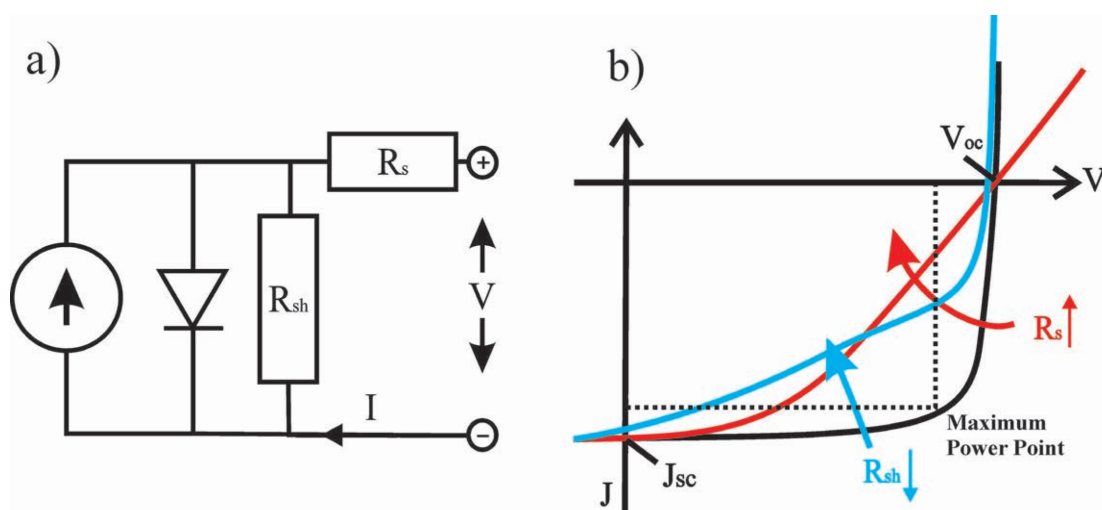

Figure 3.17: a) Equivalent circuit of a solar cell, b) J-V curve showing the ideal J-V curve (black line) and the effects of the variation of the internal resistance of the device (red and blue lines)

Fig. 3.17 shows the equivalent circuit for a solar cell. a) depicts the solar cell operation, where the latter can be seen as a current source which represents the light generated current, a diode and internal series and shunt resistances. b) shows how a change in the internal resistance of the cell can affect the J-V characteristics of the device. In that sense, the effects introduced by laser scribing processes can be assimilated by the increase of series resistance. On the other hand the decrease of the shunt resistance is due to the dead area generated during the interconnection. These effects produce a modification of the ideal J-V curve with a characteristic shift of the slopes related with the R_s and R_{sh} magnitudes observed in Fig. 3.17 represented by red and blue lines in the graph.

As it has been described above, the J-V curve of an illuminated solar cell has the

shape shown in Fig. 3.17 as the voltage across the measuring load is swept from zero to V_{oc}, and many performance parameters for the cell can be determined from this data, as described below.

The four main photovoltaic parameters which characterized the performance of a solar cell/module have been obtained in the usual way. The expression for the calculation of the same are detailed as follows:

- The FF (fill factor) is essentially a measure of quality of the solar cell. It is calculated by comparing the maximum power to the theoretical power that would be output at both the open circuit voltage and short circuit current together.

$$FF = \frac{I_{mp} \cdot V_{mp}}{I_{sc} \cdot V_{oc}} \times 100 \quad (3.3)$$

- The short-circuit current I_{sc} corresponding to the short circuit condition when the impedance is low and is calculated when the voltage equals 0.

- The open circuit voltage V_{oc} occurs when there is no current passing through the cell.

- Efficiency is the ratio of the electrical power output P_{out}, compared to the solar power input, P_{in}, into the PV cell. P_{out} can be taken to be P_{max} since the solar cell can be operated up to its maximum power output to get the maximum efficiency.

$$\eta = \frac{P_{max}}{P_{in}} \times 100 \quad (3.4)$$

4

Scribing Results

4.1 Scribing of Transparent Conductive Oxides (TCO) Layers

The study of the laser scribing of TCO's layers has great importance, not only are they essential in the first step of the laser interconnection for superstrate configuration but also for substrate interconnection where the third step of the same has to be made over a transparent conductive oxide. In this sense, the laser scribing evaluation of the TCO's is essential for two of the laser scribing steps to interconnect the cells to form modules [1, 47, 60, 62].

This section shows the laser parameter evaluation of different TCO's susceptible to be used as contact layers in the technology treated in this work. The goal of the evaluation is to find the best parameters to perform the process for the UV laser sources available at the moment, bearing in mind the original work [51] that opened the possibility to perform this work in the ultraviolet range of wavelength taking advantage of the closeness of the gap energies of the TCO materials with these wavelength. This evaluation includes:

- damage fluence threshold calculation
- scribing characterization including:
  - morphology appraisal to control the edge characteristics and the damage of the layers underneath (this will be the substrate, in the case of the TCO evaluation).

– electrical measurements to confirm the electrical isolation of the grooves

This study has been centered in the three types TCO's applied so far in commercial thin film modules based on amorphous silicon, those are, a commercial textured Asahi-U (SnO_2:F), and in-house prepared ITO (SnO_2:In_2O_3) and AZO (ZnO:Al). Table 3.1 presents the thickness range, origin and purpose of the samples of TCO utilized in this section. The structure of the samples was Glass/TCO for the damage threshold calculation and scribing characterization presented in this section. The selective scribing characterization will be presented in section 4.3. ITO is certainly the most expensive TCO as it contains a sizable fraction of Indium, which is a metal of low abundance on earth and its price has continued to increase [11]. On the other hand, both tin and zinc oxide are highly abundant and are considered environmentally harmless. The most common TCO used in present amorphous solar cells is SnO_2 (F doped) where a high quality product is the Asahi-U substrate [40].

The results are presented for the different laser sources employed in this work, acquiring the best process parameters for 355 nm wavelength which corresponds to the third harmonic of the Nd:YVO_4 laser, that as it has been mentioned before in this work, matched perfectly the requirements of the industrial process.

4.1.1 Damage Fluence Threshold Results

At first, the damage thresholds for the three TCO's have been calculated in order to have a good understanding of the behavior of this material with the laser interaction, and establishing the difference in terms of fluence necessary to perform the optimal process for the distinct material. This, along with the properties of the same will lead to establish the convenience of them to be used performed by the laser sources propose here. The damage thresholds have been determined by the method described in the section 2.4. They have been determined for two different regimes, single pulse for three different repetition rate and for multiple pulses at also different frequencies of operation.

Characteristic of the samples used in this study are presented in table 3.1, thickness of the samples were evaluated and found irrelevant for this purpose due to the independence of the same with the damage assessment.

4.1.1.1 Single Pulse Damage Threshold for λ = 355 nm and Nanosecond Pulse-width

The results obtained by the method described in section 2.4 are shown in table 4.1 and the graphical representation to obtained them are presented by the graphs shown in Fig. 4.1. The calculations have been performed for three different repetition rate in order to assess the influence of the frequency of the laser source with the laser matter interaction due to the difference in the pulse behavior shown for this laser source in its operation performance data (see Chapter 2).

Single pulse damage threshold λ = 355 nm ns radiation				
	Frequency	Asahi-U	ITO	AZO
Φ_{Th} (J/cm^2)	15 KHz	1.555±0.005	0.185±0.005	0.103±0.005
	50 KHz	1.409±0.005	0.213±0.005	0.184±0.005
	100 KHz	1.420±0.005	0.184±0.005	0.157±0.005

Table 4.1: Single pulse damage threshold values obtained for nanosecond pulse-width radiation at 355 nm of wavelength

The results show no relevant influence with the repetition rate for all the TCO's assessed in this work. From now on, the results presented in this section concerning to nanosecond radiation, just will be performed at the more stable repetition rate of the laser system HIPPO (Spectra-Physics), that is, following the specifications of the fabricate, 50 KHz of frequency.

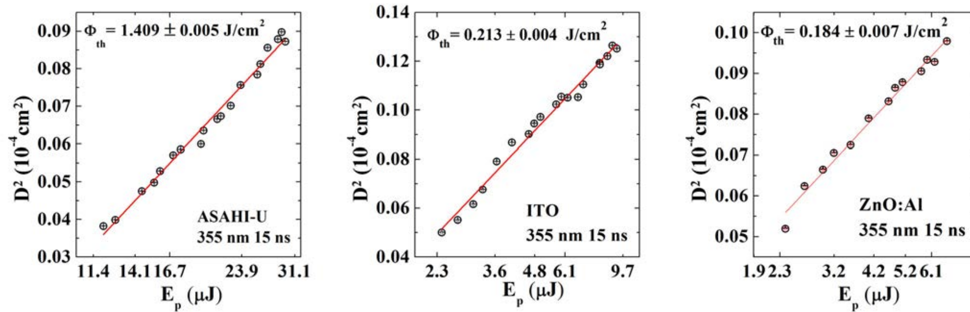

Figure 4.1: Damage threshold calculation, crater diameter represented as a function of its energy per pulse for 50 KHz of repetition rate with the corresponding fitting line and the damage threshold result

TCOs refers to heavily doped oxide semiconductors. They have a band gap sufficiently large ($\geq$ 3 eV) to make them optically transparent over the visible spectral range and own a high concentration of free carrier to give them high electrical conductivity. On this basis, the study of the results can be done as follows. The Asahi-U has the greater value of damage threshold, this difference is coherent to the band-gap value of the three materials, the wavelength 355 nm is closer to the ITO band-gap energy, which is 3.7 eV corresponding to 335.47 nm of wavelength and AZO with 3.4 eV corresponding to 365.07 nm, while the values for Asahi-U are 4.3 eV of band-gap energy corresponding to 288.66 nm. This explains the difference in damage threshold and as it will be presented below the increase in the energy required to perform the laser process in the case of Asahi-U. The wavelength of the third harmonic of the $Nd{:}YVO_4$ laser source match perfectly the band-gap of ITO and AZO, and explains the low damage threshold of the same, even taking into account the narrowly behaviour of this material with metals that could lead to think in the obtaining of similar values of the threshold with those obtained for Aluminium with a fluence threshold of 0.609 J/cm^2.

4.1.1.2 Single Pulse Damage Threshold for λ = 355 nm and Picosecond Pulse-width

In a similar way, the damage threshold for the picosecond laser source has been obtained. This time, the calculation was performed at a fixed repetition rate, due to the fact that this source does not change the pulse characteristics in its different range of frequency operation. The repetition rate chosen was 10 KHz and the results are shown in table 4.2.

Single pulse damage threshold λ = 355 nm ps radiation			
	Asahi-U	ITO	AZO
Φ_{Th} (J/cm^2)	0.462±0.003	0.36±0.01	0.324±0.006

Table 4.2: Single pulse damage threshold values obtained for picosecond pulse-width radiation at 355 nm of wavelength

Results were obtained by the graphical representation of the crater diameters with its corresponding energy per pulse as shown in Fig. 4.2.

For picosecond radiation the damage threshold value for Asahi-U is still bigger than for ITO and AZO, but the difference in magnitude is not as much as for the case of

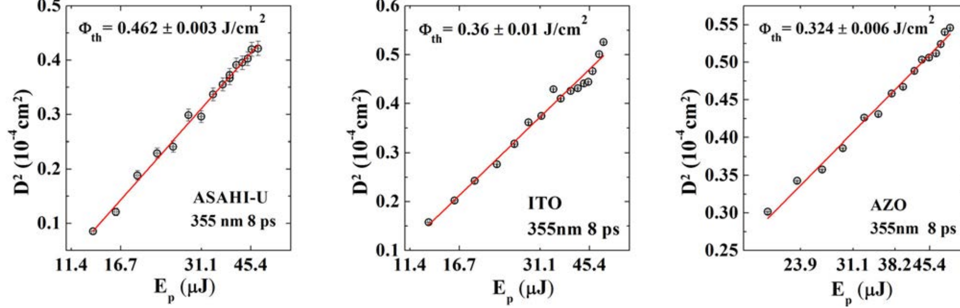

Figure 4.2: Damage threshold calculation, crater diameter represented as a function of its energy per pulse for 10 KHz of repetition rate with the corresponding fitting line and the damage threshold result

Single pulse damage threshold $\lambda = 1064$ nm ps radiation			
	Asahi-U	ITO	AZO
Φ_{Th} (J/cm^2)	2.3±0.1	1.74±0.08	1.89±0.06

Table 4.3: Single pulse damage threshold values obtained for picosecond pulse-width radiation at 1064 nm of wavelength

nanosecond pulse-widths. This indicates there must be non-linear absorption processes that are dependent of the radiation pulse-width [3].

4.1.1.3 Single pulse damage threshold for $\lambda = 1064$ nm and picosecond pulse-width

In this section, the influence of the wavelength in the TCO's used in this work is analyzed by means of the damage threshold for the three of them with a wavelength in the infrared range and picosecond puleswidth. The laser source utilized for this assessment was the same that the employed for 355 nm and picosecond pulses but working at its fundamental wavelength of 1064 nm. Consequently the results will be compare with the results obtained in the previous section.

The results are presented in table 4.3. Calculation was performed at a fixed repetition rate of 10 KHz in a similar way than for the third harmonic (355 nm) of this laser system. Owing to the fact that this source does not change the pulse characteristics in its different range of frequency operation.

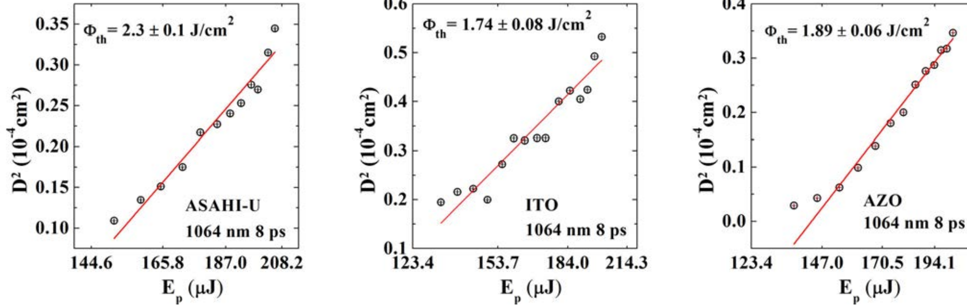

Figure 4.3: Damage threshold calculation, crater diameter represented as a function of its energy per pulse for 10 KHz of repetition rate with the corresponding fitting line and the damage threshold result

The results obtained for IR radiation are much larger than the achieved for UV radiation, again the optical characteristics of the TCO's, especially their semiconducting characteristics are the causes of the high influence of the wavelength. Materials without free electrons are transparent for photons with energy smaller than the band gap [29]. The band gap values shown in paragraph above fall in the UV range for all of the TCO's evaluated, demonstrating that the absorption of the light will be more efficient in this range than for infrared radiation. For this reason, strong absorption for all the TCO's only occurs in the spectral range of UV domain, as it has been demonstrated with the much higher values obtained for IR radiation remaining constant the rest of variables.

4.1.1.4 Multi-pulse Damage Threshold for λ = 355 nm and Nanosecond Pulse-width

Damage threshold for multiple pulses, particularly 1000 pulses, were obtained for the three TCO's in order to evaluate the effect of pulses accumulation in the laser interaction with these materials. It is particularly important due to the fact that for some of these materials more than one single pulse is required to eliminate the complete layer of material as it will be shown in scribing results. It is also important the knowledge of the behavior of the material at different regimes for further applications, such as bulk material removal, where the necessity of multiple pulses is compulsory. This assessment gives information about the mechanisms involved in the process, like the possible effect of the plasma plume inherent to all of the laser processes performed with laser pulsed

radiation at the nanosecond and picosecond range of pulse-width. In Fig. 4.4 and Table 4.4 the results for the three TCO's are represented together. It is remarked the similar tendency when the frequency is increased, all of them experiment a drop in the value of their damage threshold for 1000 pulses. This behavior is due to the accumulation effect of the pulses, more present as long as the frequency raise and therefore the time between pulses decline.

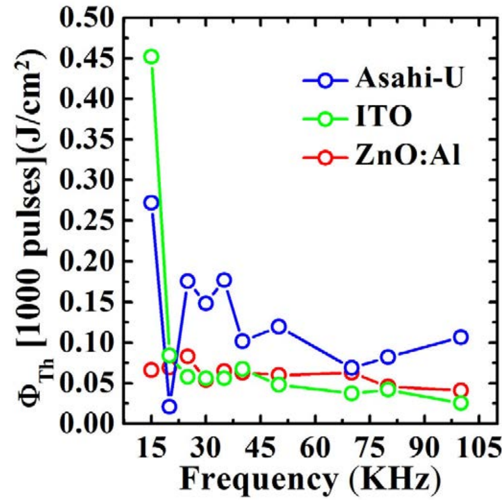

Figure 4.4: Damage threshold for 1000 pulses as a function of the repetition rate for 355 nm and nanosecond pulse-width

The damage thresholds for multipulse irradiation are much slower for the same conditions in single pulse irradiation; this can be seen remarked in the following table 4.5

4.1.1.5 Multi-pulse damage Threshold for Picosecond Pulse-width

In the same way as for nanosecond radiation, multipulse damage thresholds for picosecond radiation has been calculated. In order to obtain information about the behavior of the materials with different wavelength, the results were calculated for two different wavelength 1064 nm and 355 nm. This results as it will be foreseen are consistent with the ones obtained for nanosecond pulses.

Multipulse damage threshold λ = 355 nm ns radiation			
	Asahi-U	ITO	AZO
Frequency (KHz)	Φ_{Th} (J/cm^2) 1000 pulses		
15	0.272	0.451	0.066
20	0.021	0.084	0.069
25	0.175	0.057	0.083
30	0.148	0.056	0.054
35	0.177	0.067	0.065
40	0.101	0.048	0.063
50	0.119	0.048	0.060
70	0.068	0.037	0.063
80	0.082	0.042	0.046
100	0.106	0.025	0.041

Table 4.4: Damage threshold values obtained for 1000 pulses as a function of the repetition rate for nanosecond pulse-width radiation and 355 nm of wavelength

Damage threshold λ = 355 nm ns radiation			
	Asahi-U	ITO	AZO
Φ_{Th} (J/cm^2) single pulse	1.409	0.213	0.184
Φ_{Th} (J/cm^2) 1000 pulses	0.119	0.048	0.060

Table 4.5: Damage threshold comparison for $\lambda = 355$ nm 15 ns of pulsewidht and 50 KHz of repetition rate.

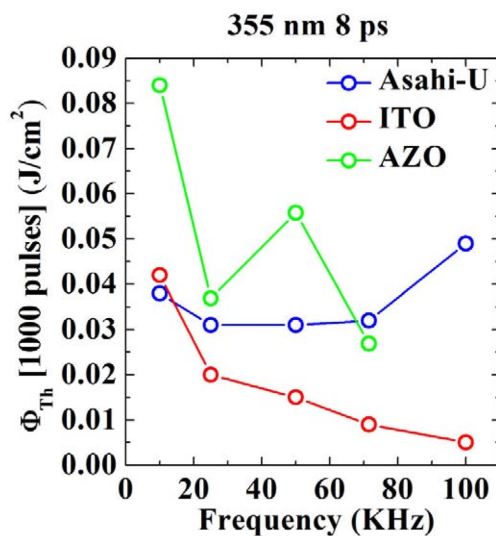

Figure 4.5: Damage threshold for 1000 pulses as a function of the repetition rate for 355 nm and picosecond pulse-width

Multipulse damage threshold $\lambda = 355$ nm ps radiation			
	Asahi-U	ITO	AZO
Frequency (KHz)	Φ_{Th} (J/cm^2) 1000 pulses		
15	0.038	0.042	0.084
25	0.031	0.018	0.037
50	0.031	0.015	0.056
71.5	0.032	0.009	0.027
100	0.049	0.005	0.084

Table 4.6: Damage threshold values obtained for picosecond pulse-width radiation at 355 nm of wavelength

These thresholds are again much higher for single pulse radiation than for multi-pulse as can be observed in the following table where the results for two condition are compared.

Damage threshold $\lambda = 355$ nm ps radiation			
	Asahi-U	ITO	AZO
Φ_{Th} (J/cm^2) single pulse	0.402	0.360	0.324
Φ_{Th} (J/cm^2) 1000 pulses	0.038	0.042	0.084

Table 4.7: Damage threshold comparison for $\lambda = 355$ nm 8 ps of pulse-width.

The same behavior is found for 1064 nm and the same pulse-width as shown in the following graph and table.

Multipulse damage threshold $\lambda = 1064$ nm ps radiation			
	Asahi-U	ITO	AZO
Frequency (KHz)	Φ_{Th} (J/cm^2) 1000 pulses		
15	0.314	0.213	0.268
25	0.235	0.254	0.269
50	0.233	0.292	0.407
71.5	—-	0.313	0.294

Table 4.8: Damage threshold values obtained for picosecond pulse-width radiation at 1064 nm of wavelength

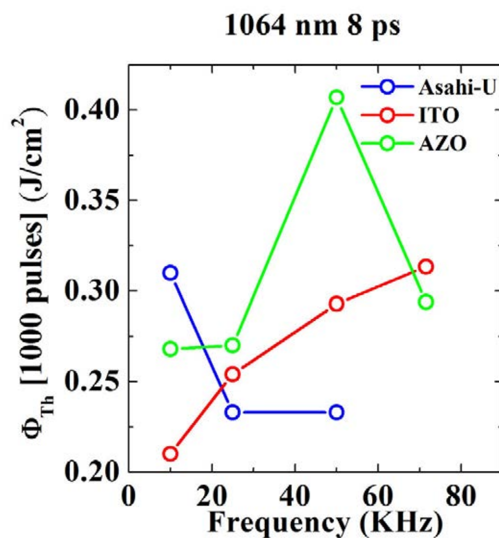

Figure 4.6: Damage threshold for 1000 pulses as a function of the repetition rate for 1064 nm and picosecond pulse-width

In table 4.9 can be seen the remarkable difference between two different condition of irradition,

Damage threshold λ = 1064 nm ps radiation			
	Asahi-U	ITO	AZO
Φ_{Th} **(J/cm^2) single pulse**	2.30	1.74	1.89
Φ_{Th} **(J/cm^2) 1000 pulses**	0.314	0.213	0.268

Table 4.9: Damage threshold comparison for λ = 1064 nm 8 ps of pulse-width.

4.1.2 TCO Scribing Results

As far as laser interconnection is concerned, a good characterization of the laser process to remove the TCO's involved in the same is required. The laser process consists in the performance of lines cleaned of material in order to isolate zones of the sheet deposited to form the solar cells modules. As TCO's are used as back and front contact in the modules, the main target of the laser process will be the electrical isolation and delimitation of different zones over the layers acting as contact films. Not only plays the isolation an important role but also the selective removal of the layer without damaging

the substrate or the layers underneath. These are the reasons because an exhaustive characterization is essential.

Owing to the results obtained form the threshold ablation calculations, the laser scribing process assessment has been performed just for wavelength in the UV domain, more precisely for the third harmonic of the vanadate laser (λ = 355 nm) and it will be evaluated the convenience of the use of picoseconds radiation versus the widely use nanosecond pulse-width as a possible innovation of this process. This section has been divided in three, in order to show the results of the laser scribing process and its characterization concerning to the three TCO's described above, that is, Asahi-U, ITO and AZO. Samples used for this purpose were the same as utilized for damage threshold calculations and are listed in table 3.1.

4.1.2.1 Asahi-U Scribing Characterization

This characterization will be presented as a comparison between the two different pulse-width regimes where this study is centered. In this way, it will be shown the results for the two radiations and the convenience in use of one over another.

A full range of experiments have been done in order to achieve the best laser parameters to perform the isolation of the grooves as an indispensable condition with good morphology characteristics and with no damage to the material underneath. Just the noteworthy results will be presented.

As the main condition to be accomplished is the electrical isolation, experiments with different speed process and energies per pulse were done in order to obtain the optimal laser process parameters. The good isolation of the groove was taken as suitable when the contact sheet resistance was over 500 MΩ.

As it has been shown at the beginning of this chapter, with the damage threshold calculation for all the materials, the Asahi-U ablation threshold is the largest of all the materials studied. The first approach for the speed process assessment was done with the maximum energy per pulse provided by the two laser sources. The results are shown in the Fig. 4.7.

From these results a closer approximation to fixed speeds process of 350 mm s^{-1} and 70 mm s^{-1} for nanosecond and picosecond radiation respectively is obtained. With these results, a new battery of experiments is done in order to find the proper values of the energy per pulse required to achieve the groove isolation. Fig. 4.8 shows the

resistance values for the best suitable speeds found in the previous assessment varying the energy per pulse.

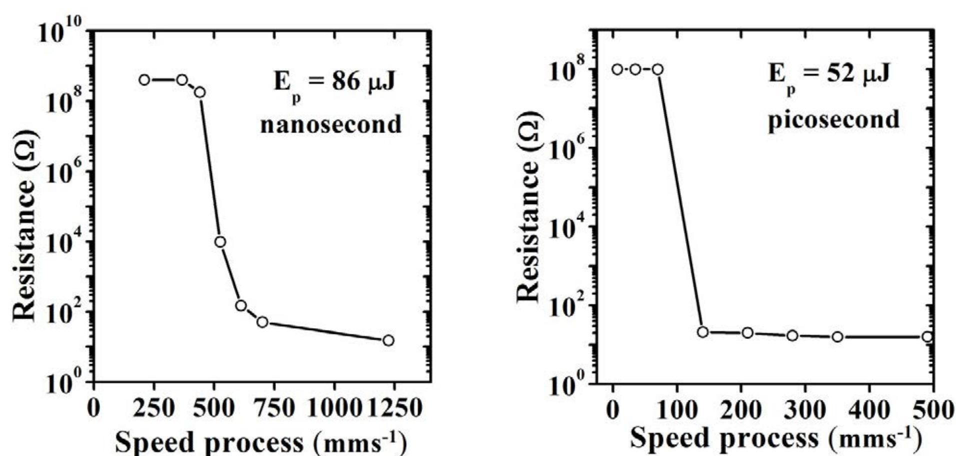

Figure 4.7: Contact resistance of grooves performed at the maximum energy per pulse of the laser sources for different speed process.

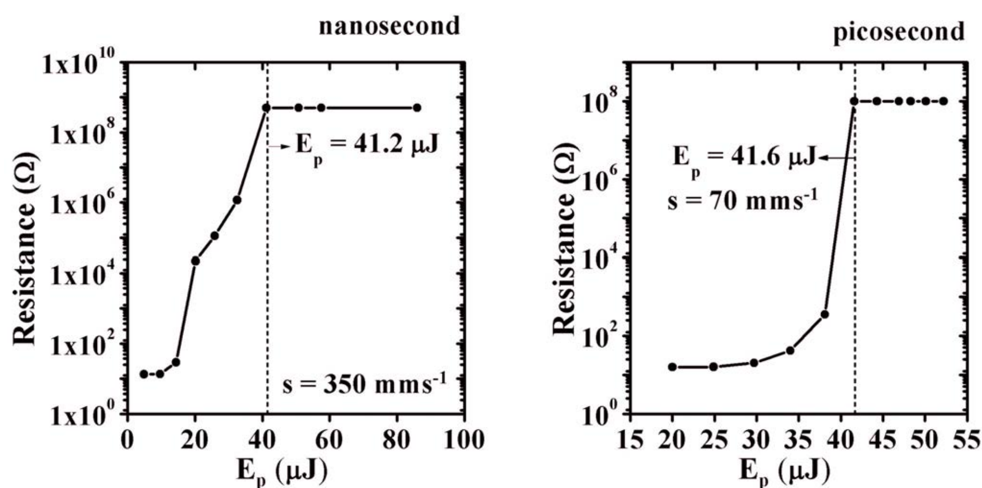

Figure 4.8: Contact resistance of grooves performed at 50 KHz, 350 mms^{-1} for nanosecond radiation and 10 KHz, 70 mms^{-1} for picosecond pulses, varying the energy per pulse

The optimal scribes, taken as the one with more than 500 MΩ of contact resistance, were obtained for the following parameters expressed in the following table 4.10. As the energy per pulse in value is exactly the same, there must be pointed out the fact

that the spot diameters of the two sources were different, this can be seen in Fig. 4.9 and 4.10 where the two optimal scribes for nanosecond and picosecond radiation are shown with their respective SEM images and Confocal profiles with the diameters measurements.

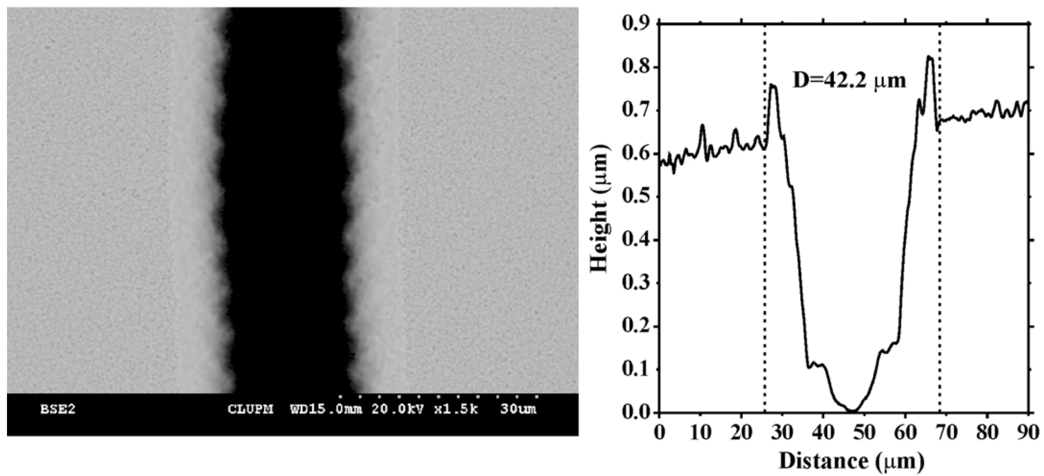

Figure 4.9: SEM image and Confocal profiles of the optimal laser scribe performed with nanosecond pulses and 355 nm of wavelength

Formation of shoulder is also present for nanosecond irradiation as shown in the confocal profile seen in Fig. 4.9, this strongly indicates that the removal of Asahi-U films for this pulse-width takes place via thermal vaporization. This effect can be attributed to the surface tension gradient in the molten film near the rim of the laser irradiated spot and the ablation pressure generated that deforms the molten film. Here the vaporization temperature is not reached due to the Gaussian pulse profile and lateral heat conduction, but due to the poor thermal conductivity of the glass substrate, melting is established for an extended time duration in the microsecond time scale during which liquid motion can take place.

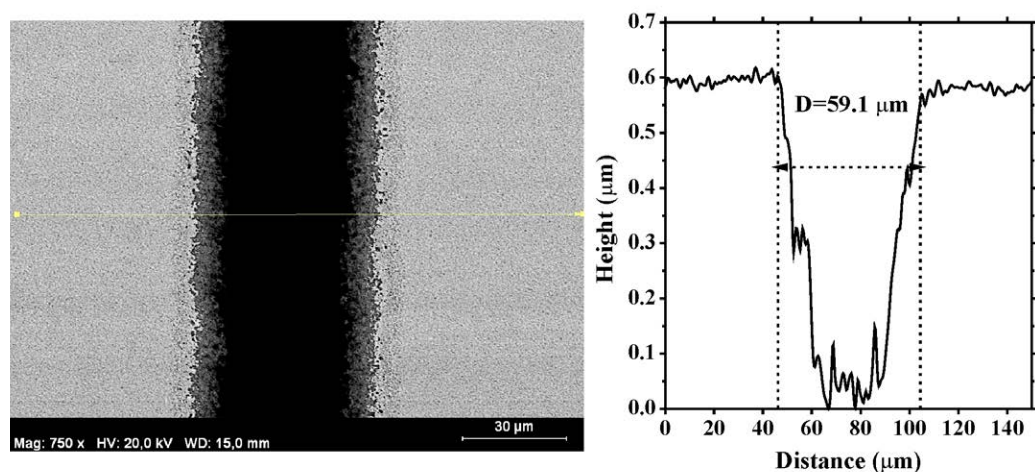

Figure 4.10: SEM image and Confocal profiles of the optimal laser scribe performed with picosecond pulses and 355 nm of wavelength

The last point to be verified is the non damage of the sustrate for the layer removal of Asahi-U over, in this case, glass substrate. This characterization is made by the study of the EDX and Confocal profiles for the two speeds and different energies evaluated above.

The damage assessment is described as follows, with regard to the silicon related to the glass substrate, the EDX silicon profiles along with the confocal profiles lead to the determination of the damage by the drop in the counts in the middle of the groove coming from this material. This can be seen in Fig. 4.11 and 4.12 where the graphs show the EDX silicon profiles for the different energies and how as long as the energy is increased the damage in the glass becomes more visible for the case of nanosecond radiation.

In the case of nanosecond radiation, due to the high values of energy per pulse delivered by the laser system, and its long pulse duration, the damage of the glass is more evident from the pulse-width chosen as optimal. If we compare these results with the obtained for picosecond radiation, the EDX and confocal show no noteworthy damage in the whole range of energy allow by the laser system. Nonetheless, for similar energy values, the damage in the glass substrate and the formation of ridges in the edge of the grooves are remarkable for the case of nanosecond pulses whereas for

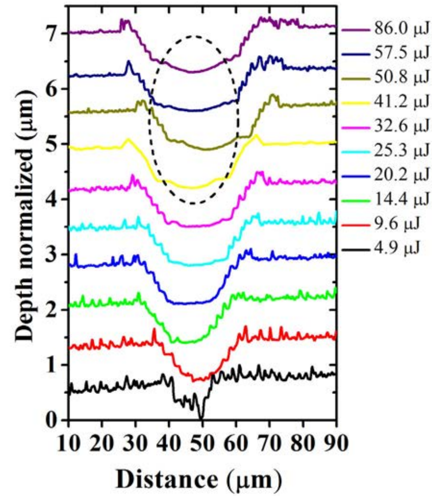

(a) Confocal profiles.

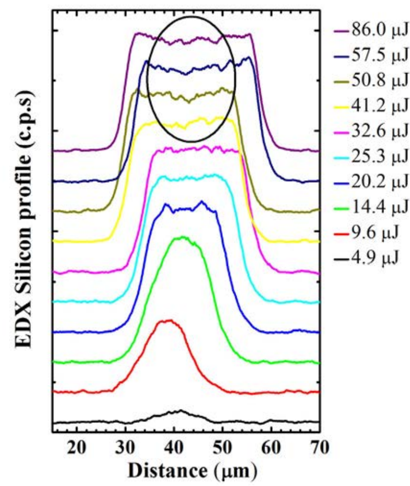

(b) EDX Silicon profiles.

Figure 4.11: Substrate damage assessment of laser scribing of Asahi-U over glass for the nanosecond source with a fixed repetition rate of 50KHz and 350 mms^{-1}

the picosecond ones there is no evidence of such effects probably due to the less heat conduction that occurs for the latter.

Finally, table 4.10 shows the parameters in terms of number of pulses, overlap, ablation fluence threshold and the process fluence and energy per pulse necessary to performed the optimal grooves in order to remarked the difference in energy needed to achieve the isolation in the grooves, and also its consistency with the previously damage threshold obtained.

	E_p (μJ)	Φ (J/cm^2)	Pulses per Location	Overlap %	$\Phi(\Phi_{Th})$
ns	41.2	2.946	6.03	83.4 (D=42.2 μm)	2.09
ps	41.6	1.516	8.44	88.2 (D=59.1 μm)	3.28

Table 4.10: Laser process parameters for optimal scribes over Asahi-U for nanosecond and picosecond UV radiation

4.1.2.2 ITO Scribing Characterization

The results for the other TCO's studied in this work will be presented in the similar way than for the previous one. As it has been mentioned, the electrical isolation is the main condition to be achieved, and it will lead along with the morphological characterization to the optimal laser process parameters. A full range of experiments have been done for this material but just the remarkable results will be presented.

The starting point of the parametrization was based on the damage threshold calculations presented at the beginning of this chapter. For the case of the ITO material the damage threshold has a low value and this will be consistence with the low laser energy needed to remove the TCO layer, where the elimination of the material is achieved with just one pulse [16].

Again, the proper isolation of the scribes was chosen when the contact sheet resistance exceeded a value of 500 Ω. In this material, the assessment is centred in the consecution of the minimum overlap, which is achieved at high speed process due to the removal of the material with just one pulse. The electrical measurements are not presented owing to this subject, all of the scribes where isolated as long as the overlap was achieved, without any separation between pulses that would spoil the isolation. Several

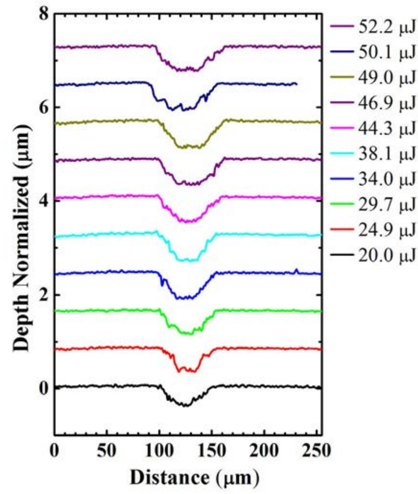

(a) Confocal profiles

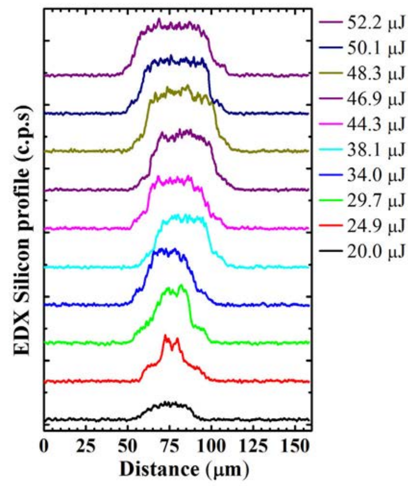

(b) EDX Silicon profiles

Figure 4.12: Substrate damage assessment of laser scribing of Asahi-U over glass for the nanosecond source with a fixed repetition rate of 10 KHz and 70 mm s^{-1}

speeds were assessed, for the results corresponding to lower speeds the electrical isolation was accomplished for all the energies tested. This behaviour was experimented for the two pulse-width regimes, ps and ns, chosen to be assessed in this work.

The optimal parameters for the scribing isolation are presented in table 4.11. The corresponding SEM images and Confocal profiles are shown in Fig. 4.13 and 4.14. This laser scribing process is governed by the removal of the complete layer of material with just one pulse; this reduces the optimization of the process to the consecution of a good overlap between the pulses. The results conclude that picosecond irradiation achieves better morphology of the grooves without ridges in the edges shown in the confocal profiles, where picoseconds scribes appears with smooth edges. This condition was also observed in the case of Asahi-U. Although the energy necessary for carrying out the process is slightly bigger in the case of picosecond radiation the smoother edges and therefore the best morphology results for picosecond radiation making the latter suitable to be the successor of the nanosecond sources currently used for this process in the industry.

	E_p (μJ)	Φ (J/cm^2)	Pulses per Location	Overlap %	$\Phi(\Phi_{Th})$
ns	2.48	0.286	1.6	36.7 (D=33.2 μm)	1.3
ps	22.3	0.902	1.05	5.5 (D=56.1μm)	2.5

Table 4.11: Laser process parameters for optimal scribes over ITO for nanosecond and picosecond UV radiation

As it has been seen in the case of Asahi-U, the formation of shoulders is also present for nanosecond irradiation as shown in the confocal profile of Fig. 4.13, this strongly indicates that the removal ITO films for this pulse-width takes place via thermal vaporization. And can be attributed to the surface tension gradient in the molten film near the rim of the laser irradiated spot. Here the vaporization temperature is not reached due to the Gaussian pulse profile and lateral heat conduction, but due to the pour thermal conductivity of the glass substrate, melting is established for an extended time duration in the microsecond time scale during which liquid motion can take place [67]. This melting and fast resolidification of an ITO film, induced by pulsed nanosecond laser heating at subdamage threshold fluences have been reported to result in the production of structural defects, causing a change in the optical absorption spectrum [61]. Similarly, in the present work the materials properties of ITO in the shoulderlike

structure at the rim of the irradiated spot are likely to be modified with respect to the virgin ITO film. It is noted that electrical conductivity of an ITO film sensitively depends on its microstructure and composition.

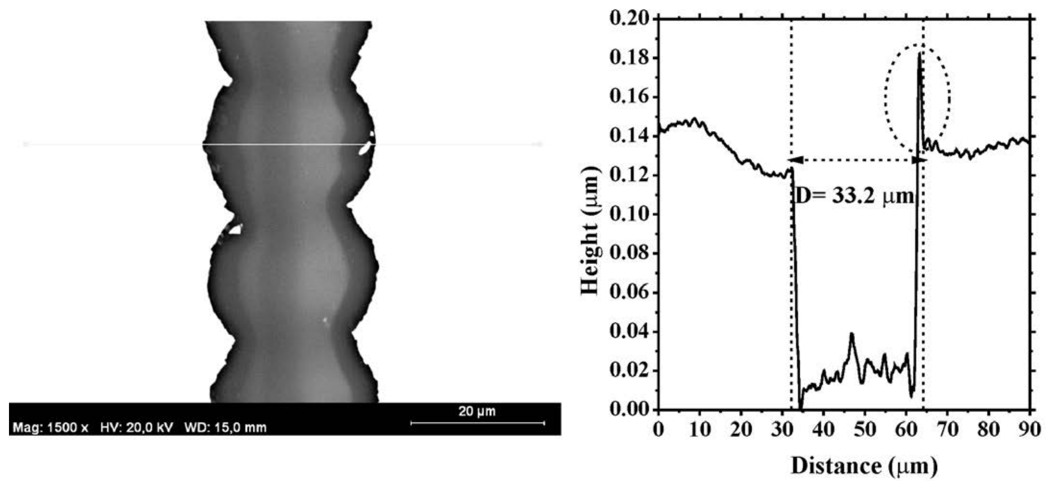

Figure 4.13: SEM image and Confocal profiles of the optimal laser scribe performed with nanosecond pulses and 355 nm of wavelength at 1050 mm s^{-1}

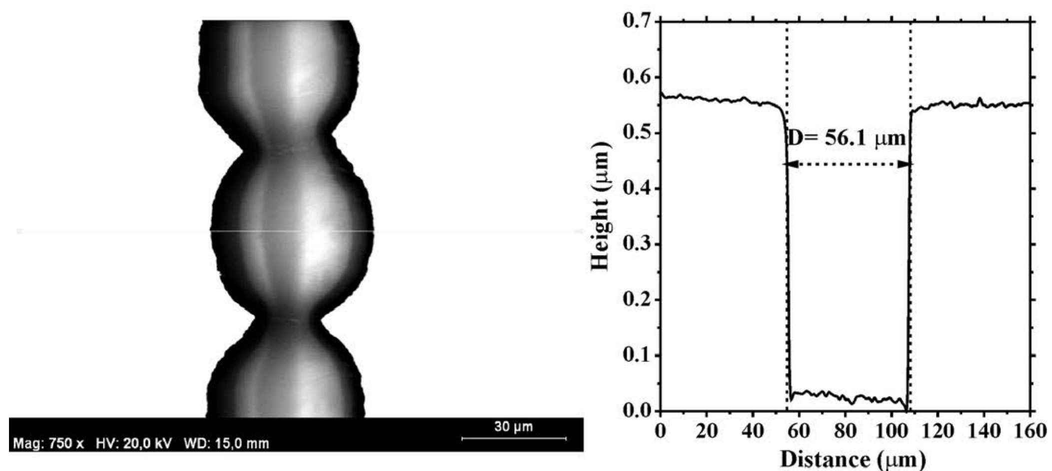

Figure 4.14: SEM image and Confocal profiles of the optimal laser scribe performed with picosecond pulses and 355 nm of wavelength at 530 mm s^{-1}

In order to assess the behavior of ITO with the increasing of the energy of the pulses, additional experiments have been done at the same optimal speed process. This leads to the evaluation of the substrate damage as it has been presented above for the case of Asahi-U. As far as nanosecond radiation is concerned the experiments show a special behavior comparing with picoseconds shown in the SEM images for both of them in Fig. 4.15 and 4.17, where the expected damage on the substrate does not occur in form of elimination of material but with some redeposition or not elimination of TCO material in the middle of the groove when the energy increases. This phenomenon is illustrated in Fig. 4.18. Information regarding of the presence of TCO in the middle of the grooves has been evaluated with the EDX profiles corresponding to the main elements forming the ITO, these are Tin (Sn) and Indium (In) for the nanosecond pulse-width radiation due to the lack of this behaviour in the case of picosecond pulses. The height confocal profiles show, as seen in Fig. 4.18, a material accumulation of the material in the middle of the groove. This leads to think that there must be a deposition of material or non-elimination of the same instead of the diffusion of material on the substrate.

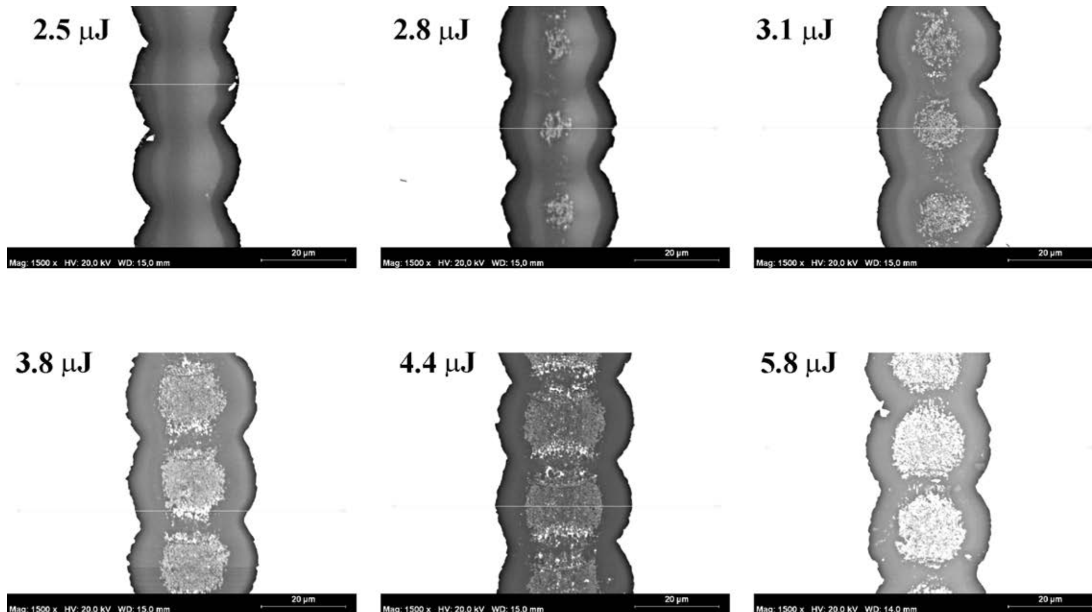

Figure 4.15: SEM images of ITO laser scribes carried out with nanosecond pulse-width at 355 nm of wavelength and 1050 mm s^{-1} of speed process

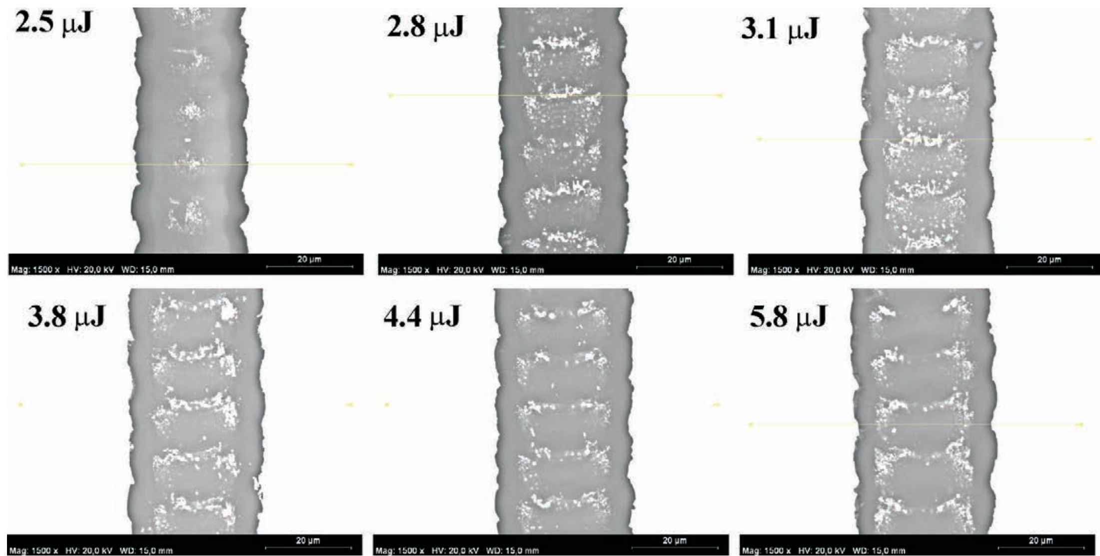

Figure 4.16: SEM images of ITO laser scribes carried out with nanosecond pulse-width at 355 nm of wavelength and 600 mm s^{-1} of speed process

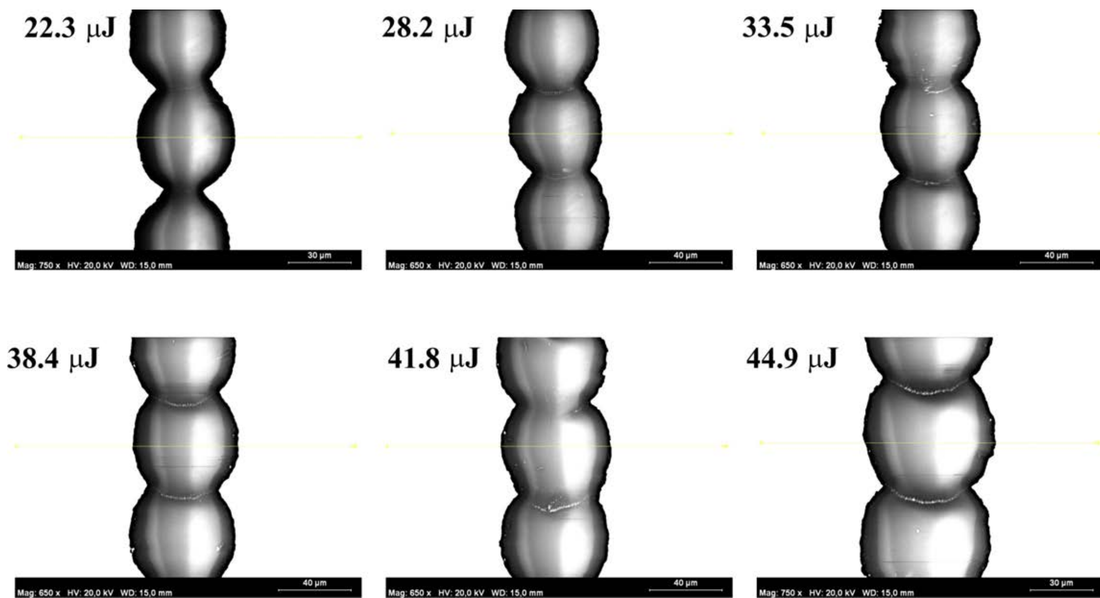

Figure 4.17: SEM images of ITO laser scribes carried out with nanosecond pulse-width at 355 nm of wavelength and 530 mm s^{-1} of speed process

In Fig. 4.18, the confocal profiles show an elevation in the middle of the grooves from the value of 2.8 μJ to further energies per pulse, this corresponds with the material observation in the SEM images presented in Fig. 4.16. The EDX profiles corresponding

to Tin and Indium confirm the existence of these materials where the confocal profiles and topographical images demonstrate an increased in height.

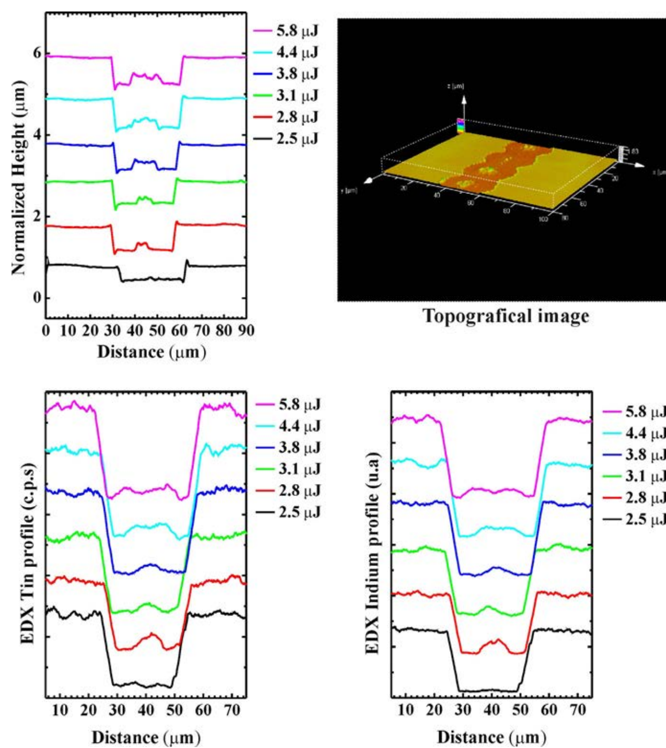

Figure 4.18: Confocal, EDX profiles and a confocal topographical image where the accumulation with the increase of of processing energy of material is demonstrated

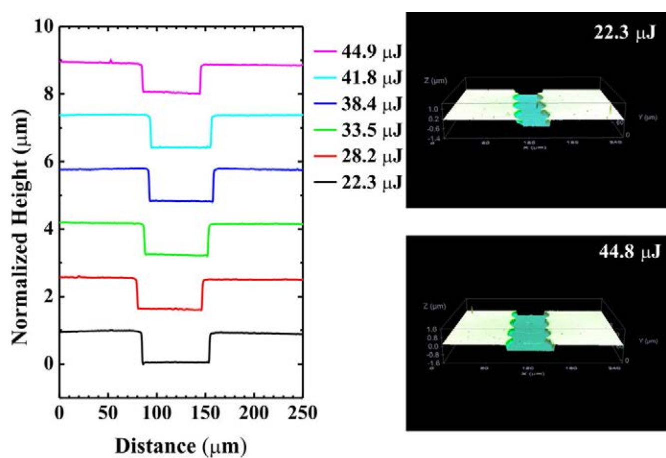

Figure 4.19: Confocal profiles and topographical images of laser scribes carried out at 355 nm and picosecond pulse-width for different pulse energies.

Regarding to picoseconds experiments, confocal profiles where obtained to assess this phenomenon, but no accumulation was found as can be seen in the confocal profiles in Fig. 4.19, there was no need of EDX profiles measurements in this case, confocal topographical images are presented in order to illustrate the lack of material in the interior of the grooves. Fig. 4.19 also is evidence for the good results obtained with picosecond radiation, mainly attending to the good smooth edges obtained for all the energies.

4.1.2.3 AZO Scribing Characterization

AZO may be used as front contact in superstrate configuration where the layer of TCO is deposited over the glass substrate, and also as front contact in substrate configuration where the layer is over the silicon structure. In this section the results corresponding to AZO deposited over glass are presented, this results will give preliminary information about the laser scribing process that will be used for the selective ablation process required for removing the TCO deposited in substrate configuration where the layer is over the complete stack of the cell. Because of this, the results are divided in two section, AZO deposited over glass substrate and AZO over the amorphous silicon structure which will be presented in section 4.3.1.

Proper isolation of the scribes was chosen when the contact sheet resistance exceeded a value of 500 MΩ. In this material, as in ITO, the assessment is centred in the consecution of the minimum overlap, which is achieved at high speed process due to the removal of the material with just one pulse. Several speeds were assessed, for the results corresponding high overlap, the electrical isolation was accomplished for all the energies per pulse tested. This behaviour was experimented for the two pulse-widths chosen to be assessed in this work. Fig 4.20 shows the electrical measurement for the speed more relevant in this study.

The optimal parameters for the scribing isolation are presented in table 4.12. The corresponding SEM images and Confocal profiles are shown in Fig. 4.21 and 4.22. This laser scribing process is governed by the removal of the complete layer of material with just one pulse; this reduces the optimatization of the process to the consecution of a good overlap.

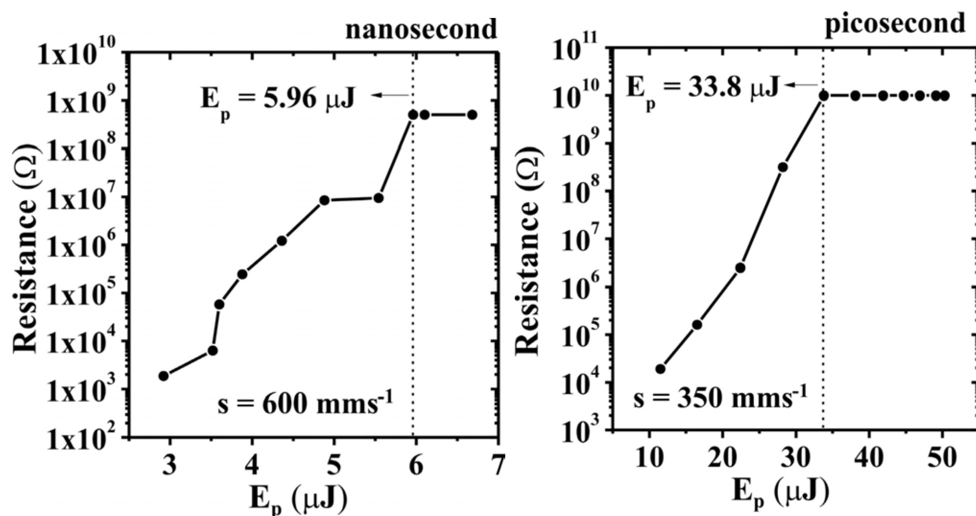

Figure 4.20: Contact resistance of grooves performed at 50 KHz, 600 mms^{-1} and nanosecond radiation and 10 KHz, 350 mms^{-1} for picosecond pulses, varying the energy per pulse

	E$_p$ (μJ)	**Φ (J/cm^2)**	**Pulses per Location**	**Overlap %**	**$\Phi(\Phi_{Th})$**
ns	5.96	1.03	2.26	36.7 (D=27.1 μm)	5.6
ps	33.8	1.69	1.05	50.5 (D=50.5 μm)	5.2

Table 4.12: Laser process parameters for optimal scribes over AZO for nanosecond and picosecond UV radiation

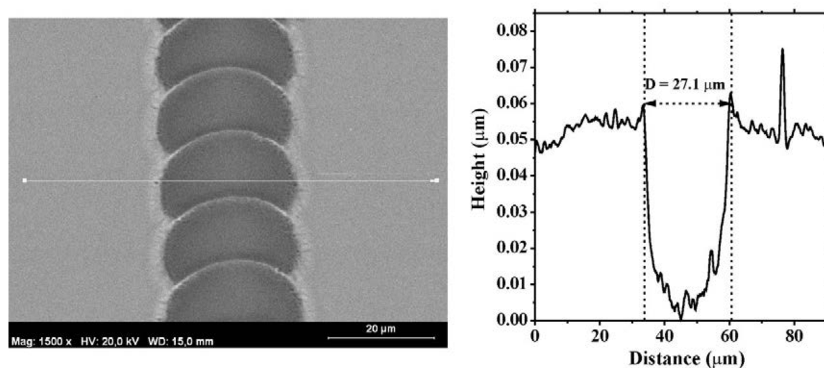

Figure 4.21: SEM image and Confocal profiles of the optimal laser scribe performed with nanosecond pulses and 355 nm of wavelength at 600 mms^{-1} of speed process and 5.96 μJ of pulse energy.

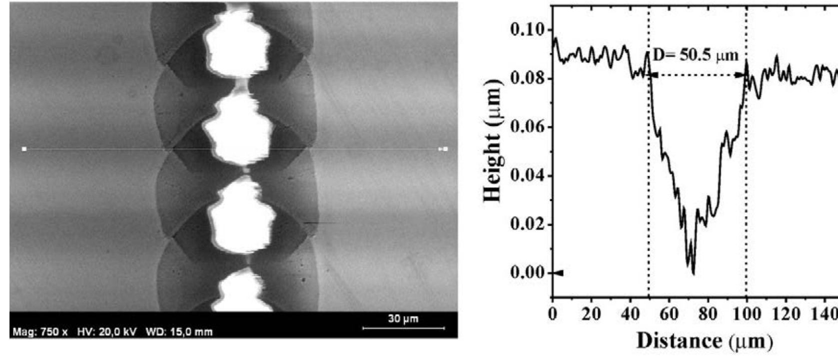

Figure 4.22: SEM image and Confocal profiles of the optimal laser scribe performed with picosecond pulses and 355 nm of wavelength at 350 mms^{-1} of speed process and 33.8 μJ of pulse energy.

As in the case of ITO, the low damage threshold leads to the elimination of the material with low energies per pulse, but as the same than in the ITO ablation, some material is left in the elimination process when the energy is increased. This behaviour is again observed in the case of nanosecond radiation exclusively. But a different way than ITO, the pattern observed on the etched groove is formed due to the incomplete removal of the material in the border of the laser spot. Despite of the presence of this ripplelike the electrical isolation turn out to be independent with this phenomenon.

This phenomenon is fully described by [67]. The results presented here also present this ripple like structure dependent with the speed process and the repetition rate, i.e. the overlap, the spacing of the structure is directly related with the overlap, the more overlap the less spacing in the ripplelike structure. This behaviour is shown in Fig. 4.23. All the lines were isolated and performed at the same energy per pulse. The SEM images show the ripplelike structure with the spacing decreased as the speed decreases or the overlap increases. The confirmation of the incomplete removal of the material in the etched groove for these lines is done by the representation of the Zn counts profile coming from the EDX signal (Fig. 4.24). As [67] observed in his work, this phenomenon is probably due to the absorption of the glass substrate for 355 nm of wavelength, and the thermal vaporization which governs the process [68].

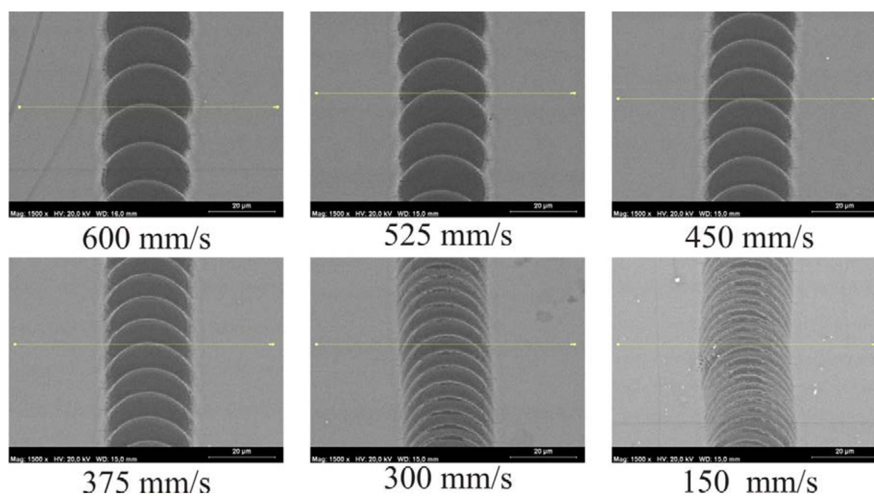

Figure 4.23: Laser scribes of AZO over glass performed at nanosecond radiation of 355 nm of wavelength 50 KHz and 5.96 μJ of pulse energy.

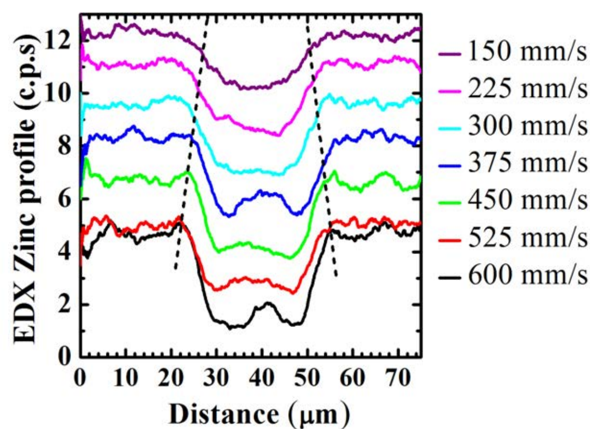

Figure 4.24: EDX Zinc profiles of laser scribes of AZO over glass performed at nanosecond radiation of 355 nm of wavelength 50 KHz and 5.96 μJ of pulse energy, varying the scribing speed.

The EDX profiles show the accumulation of material as long as the scribing speed decrease, the incomplete removal of the material is more remarkable for the lowest speed and the scribe width is decreased due to this unsuccessful removal. Nonetheless, it must be pointed out again that all the scribed lines were electrically isolated.

In order to illustrate the difference with picoseconds radiation, where this phenomenon is not observed, Fig. 4.25 show the same experiments in terms of scribing

speed variation. In this case, SEM images demonstrate that there is no material in the etched groove, and to corroborate the same, Fig. 4.26 illustrates the confirmation via EDX Zinc profiles, where no material remains.

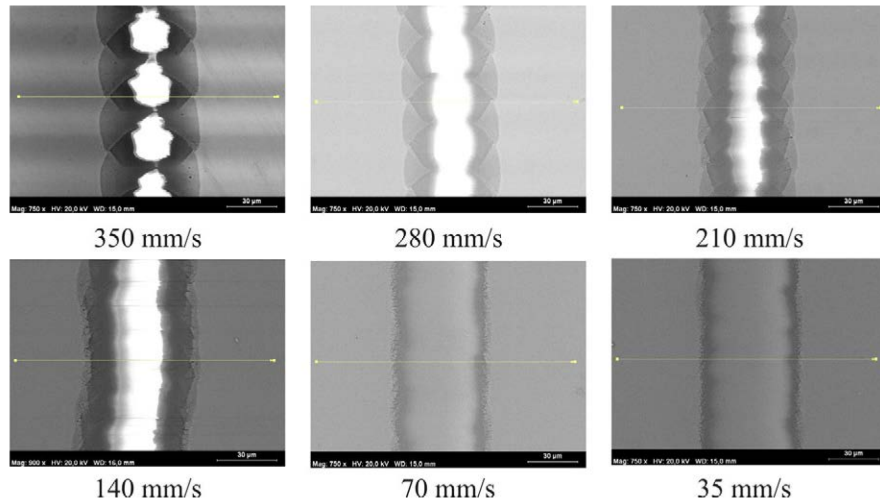

Figure 4.25: Laser scribes of AZO over glass performed at picosecond radiation of 355 nm of wavelength 10 KHz and a common pulse energy of 33.8 μJ.

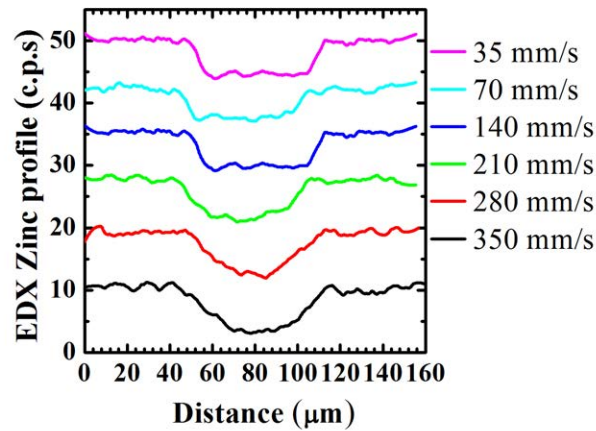

Figure 4.26: EDX Zinc profiles of laser scribes of AZO over glass performed at picosecond radiation of 355 nm of wavelength 10 KHz and 33.8 μJ of pulse energy, varying the scribing speed.

According with chapter 2 the thermal vaporization governs the nanosecond process more strongly than for the scribes performed with picosecond pulses; this would explain

the absence of this phenomenon for shortest pulses, where it has been demonstrated the lack of remaining material and therefore the ripplelike structure in the etched groove.

4.2 Scribing of a-Si:H Structure Layer

In this chapter, the study of laser scribing of the a-Si:H layer is performed. In the general approach for monolithic interconnection process, the removal of the active layer is done in back scribing configuration as it has been mentioned all over this work, but in the extent of this work this removal must be done from the film side in direct scribing configuration. This implies that the elimination of the layer must be done selectively without damaging the layers underneath. In order to achieve the best laser process and accomplish these requirements, a complete study including damage threshold calculation and the scribing process characterization is presented in this chapter. Samples used in this chapter are listed in table 3.1, (Glass/a-Si:H) structures were used for the calculation of the damage threshold and the P2 assessment was carried out in a complete structure (Glass/Asahi-U/a-Si:H).

4.2.1 Damage fluence threshold results.

In the same way as performed for TCO's the damage thresholds for amorphous silicon have been calculated in order to have a good understanding of the behaviour of this material with the laser interaction, and establishing the difference in terms of fluence necessary to perform the optimal process for selective ablation of this material. This assessment has been made for different irradiation conditions, two wavelengths 355 nm and 1064 nm and two pulse-width ranges, nanosecond and picoseconds.

The study is divided in two different sections attending to the number of pulses, single pulse and multiple pulses. The damage threshold in single pulse will give evidence about the material interaction with the wavelength and the pulse-width [37] whereas the multiple pulses threshold will give information about the incubation effect [48] when multiple pulses are deposited in the material in different temporal regimes.

The damage threshold have been determined according with the method described in section 2.4.

Single pulse damage threshold λ = 355 nm ns radiation			
	15 KHz	50 KHz	100 KHz
Φ_{Th} (J/cm^2)	0.104±0.004	0.13±0.09	0.10±0.09

Table 4.13: Single pulse damage threshold values of a-Si:H obtained for nanosecond pulse-width radiation at 355 nm of wavelength

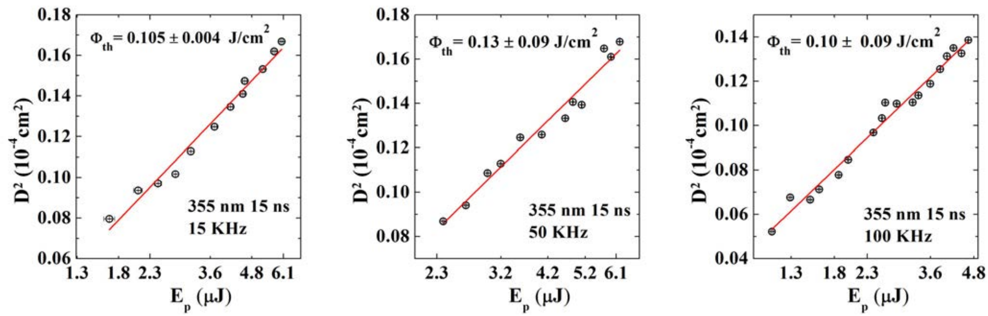

Figure 4.27: Damage threshold calculation, crater diameter represented as a function of its energy per pulse for three repetition rates with the corresponding fitting line and the damage threshold result

4.2.1.1 Single Pulse Damage Threshold at λ = 355 nm and Nanosecond Pulse-width.

The results obtained by the method described in section 2.4 are shown in table 4.13 and the graphical representation to obtained them are presented in Fig. 4.27. The calculations have been carried out for three different repetition rate in order to assess the influence of the frequency of the laser source with the laser matter interaction due to the difference in the pulses behaviour shown for this laser source in its operation performance data (see Chapter 3).

Table 4.13 shows the results for three different conditions. There are not significant changes in the values for the three frequencies studied, so 50 KHz will be assume the frequency of operation since the laser system is optimized in this value and meets better stability and efficiency.

4.2.1.2 Multi-pulse Damage Threshold at λ = 355 nm Nanosecond Radiation.

Damage threshold for multi-pulses, particularly 1000 pulses, were obtained for the amorphous silicon layer, as it was done for TCO's, in order to evaluate the effect of pulses accumulation in the laser interaction with these materials. It is important the knowledge of the behaviour of the material at different regimes for further applications, such as bulk material removal, where the necessity of multiple pulses is compulsory. This assessment gives information about the mechanisms involved in the process like the possible effect of the plasma plume inherent to all of the laser process performed with laser pulsed radiation at the nanosecond and picoseconds range of pulse-width. In the Fig. 4.28 and the corresponding table 4.14 of results for multiple damage threshold at different frequencies of operation are represented. It is remarked the similar tendency when the frequency is increased, all of them experiment a drop in the value of their damage threshold for 1000 pulses. The threshold in single pulse condition is almost four times bigger than for multi-pulse irradiation. This behaviour is due to the accumulation effect of the pulses, more present as long as the frequency raise and therefore the time between pulses decline.

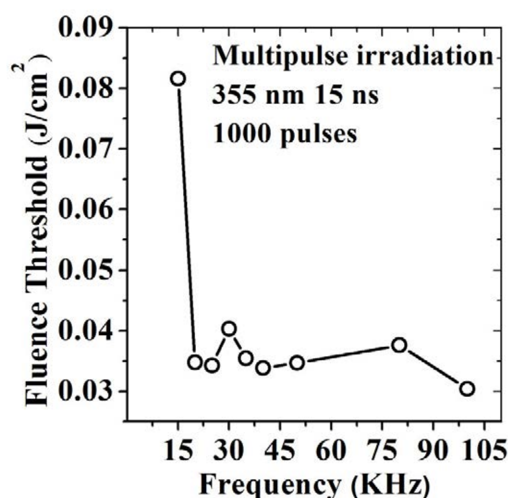

Figure 4.28: Damage threshold for 1000 pulses as a function of the repetition rate for 355 nm and nanosecond pulse-width

Multipulse damage threshold	
Frequency (KHz)	Φ_{Th} (J/cm^2) 1000 pulses
15	0.082
20	0.045
25	0.035
30	0.040
35	0.035
40	0.034
50	0.035
80	0.038
100	0.030

Table 4.14: Damage threshold values obtained for 1000 pulses as a function of the repetition rate for nanosecond pulse-width radiation and 355 nm of wavelength

Single pulse damage threshold picosecond radiation		
	λ = 355 nm	λ = 1064 nm
Φ_{Th} (J/cm^2)	0.111±0.004	0.213±0.003

Table 4.15: Single pulse damage threshold values obtained for nanosecond pulse-width radiation at 355 nm of wavelength

4.2.1.3 Single pulse damage threshold at λ = 355 nm, 1064 nm and picosecond pulse-width.

In a similar way, the damage threshold for the picosecond laser source has been obtained. This time, the calculation was performed at a fixed repetition rate, due to the fact that this source does not change the pulse characteristics in its different range of frequency operation. For amorphous silicon the values for the two different wavelengths studied here are presented together. The repetition rate chosen was 10 KHz, and the results are shown in the table 4.15.

Those results were obtained by the graphical representation of the crater diameters with its corresponding energy per pulse (Fig. 4.29). Results corresponding to 355 nm of wavelength are very similar for both pulse-widths, however there is a difference of two times in the value for infrared wavelength, consistent once more with the results obtains in TCO's materials where more energy is needed to ablate these materials with

infrared wavelength.

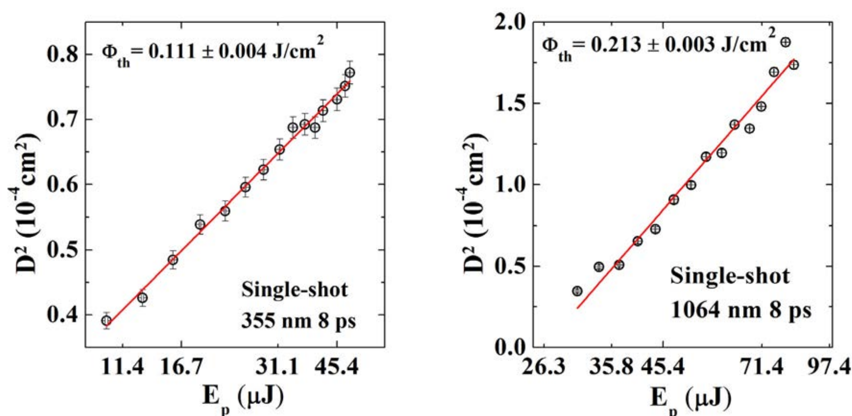

Figure 4.29: Damage threshold crater diameter represented as a function of its energy per pulse with the corresponding fitting line and the ablation threshold result for two wavelengths

4.2.1.4 Multi-pulse damage threshold at λ = 355 nm, 1064 nm

Damage threshold results obtained in multi-pulse configuration are shown in Fig. 4.30 and table 4.16. In this case, as it was expected, due to the stability in the pulses of the laser source, there is no difference in the results attending to the frequency. On the other hand, there are substantial differences for the wavelength used again consistent with the results obtained for other materials, where the infrared damage thresholds are bigger than the ones obtained at ultraviolet radiation. When multi-pulse values are compared with the single-pulse damage threshold, it is shown that the latter are one order bigger, this difference is bigger in this case where the pulse-width is in the range of the picosecond.

Multi-pulse damage threshold		
Wavelength	355 nm	1064 nm
Frequency (KHz)	Φ_{Th} (J/cm^2) 1000 pulses	
10	0.014	0.033
25	0.016	0.027
50	0.013	0.030
71.5	0.014	0.031
100	0.013	0.032

Table 4.16: Damage threshold values obtained for 1000 pulses as a function of the repetition rate for picosecond pulse-width radiation at 355 and 1064 nm of wavelength

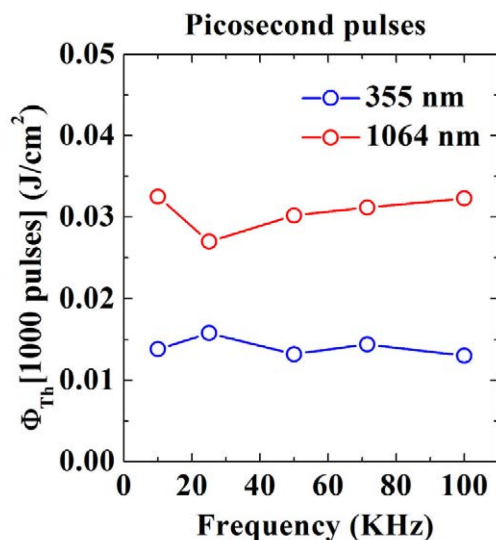

Figure 4.30: Damage threshold for 1000 pulses as a function of the repetition rate for 355 nm and nanosecond pulse-width

4.2.2 Selective ablation of a-Si:H structure characterization

In the case of a-Si:H scribing, characterization of the selective ablation of the layer is specially relevant, as the structure must be removed without compromising the layer underneath and the silicon structure.

To characterize the selective removal of the a-Si:H layer, the same is done attending to the morphology of the grooves, measuring the changes on the material structure in the vicinity of the laser scribe caused by laser irradiation by means of Raman spec-

troscopy and evaluating damage on the TCO layer underneath the amorphous silicon layer.

The assessment has been done just for wavelength of 355 nm, seeing that damage thresholds are notable lower for this wavelength, and the convenience of possible use of the same laser source to carry our all the steps which compose the interconnection.

In this case, the optimal scribes present complete removal of the a-Si:H layer with good edge profile, i.e. smooth grooves and no damage on the layer underneath. A complete study of scribing has been done and relevant results are presented.

The complete ablation of the amorphous silicon layer has been accomplished without damaging the underneath layer of TCO for both laser sources. This process has been assessed by EDX microanalysis, which allowed the evaluation of the selective removal of the silicon layer, additionally to the assessment of the damage on the TCO. In table 4.17 are represented the laser parameters for the two different radiations attending to the best result obtained in two different speed regimes, corresponding to different overlaps. Where it can be seen that for picosecond radiation more energy is needed in the case of low overlap, but more pulses are needed when the fluence is similar to the used with nanosecond pulses.

	Φ (J/cm^2)		**Pulses per location**		**$\Phi(\Phi_{Th})$**	
	ns	ps	ns	ps	ns	ps
Low overlap	0.59	1.26	1.6	1.8	5.1	5.8
High overlap	0.47	0.57	3.6	7.9	4.1	2.6

Table 4.17: Laser parameter for the optimal scribes of amorphous silicon structure layer in terms of fluence (J/cm^2) and number of pulses per location with damage of threshold of 0.13 and 0.11 J/cm^2 for ns and ps radiation respectively

Nevertheless, it is more important in this case to assess the morphological aspects of the groove together with the removal of the material and damage of the layer underneath. To accomplish characterized with EDX spectroscopy and SEM images for laser parameters presented in table 4.17 of low and high overlap for the two different pulse-widths.

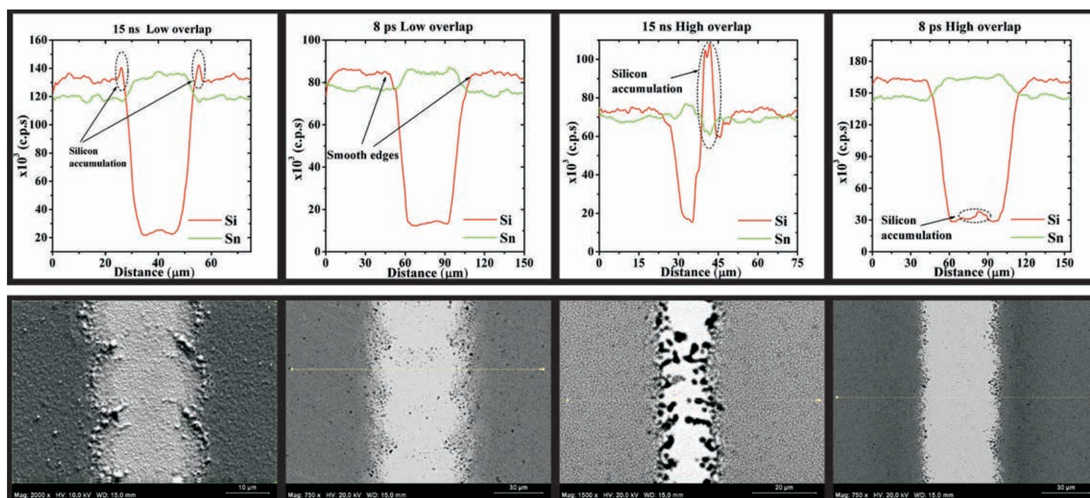

Figure 4.31: SEM images and EDX profiles of laser scribes at nanosecond and picosecond radiation of a-Si:H (pin)/Asahi-U/Glass)

Fig 4.31 shows that the best results are achieved with the picosecond source and for high overlap, the edge of the groove for this condition is better, and the effect of the Gaussian energy profile is less pronounced for highest overlaps. Not in the case of the nanosecond radiation where the low speed regime leads to more accumulation of material in the groove. With these results we conclude that the best results are low overlap for nanosecond radiation and high overlap for picosecond.

To correlate the Silicon accumulation on the edge of the groove with its real height, the confocal and EDX profiles for the optimal scribes have been represented together as can be seen in Fig. 4.32. EDX profiles can demonstrate selective ablation of silicon and also the damage of the TCO layer by the drop in the atom counts coming from silicon and tin related to the two different layers as Fig. 4.33 reveals. When the Silicon profile drops in the middle of the groove, without decreasing the counts coming from the Tin of the Asahi-U in the same location, this indicates that the amorphous silicon layer has been removed without damaging the layer underneath.

To illustrate this in a better way, Fig. 4.33 supports the damage on the TCO layer during the P2 process in EDX profiles. When the counts coming from the TCO drop in the middle of the groove, it is seen an associated increase in the counts of Silicon appearing at the same position due to the Silicon contribution of the glass. This becomes more evident when more energy is deposited. When the Silicon counts

exceed the ones from the Tin, this means that there is a large contribution of the Silicon coming from the glass, implying that the TCO layer has been removed. This assessment is especially relevant because the damage of the TCO layer leads to an increase in the series resistance of the final device.

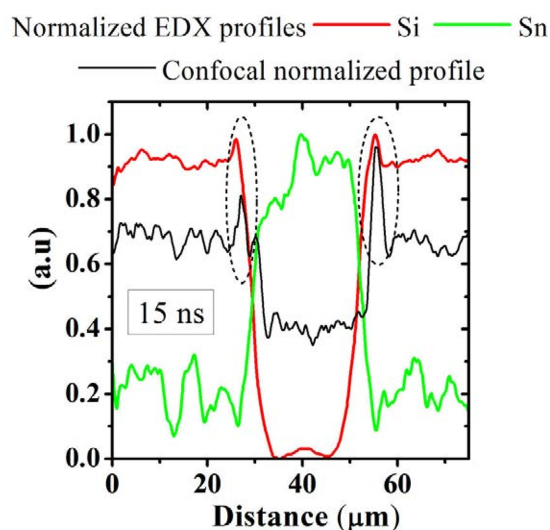

(a) nanosecond pulses

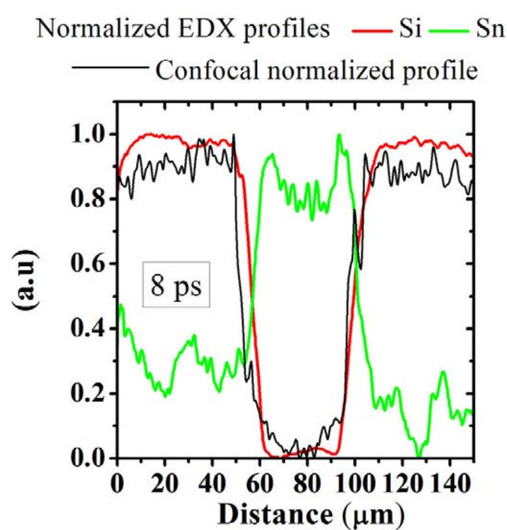

(b) picosecond pulses

Figure 4.32: Confocal and EDX profiles of laser scribes of asi (pin)/Asahi-U/Glass for optimal scribes for two different pulse-widths

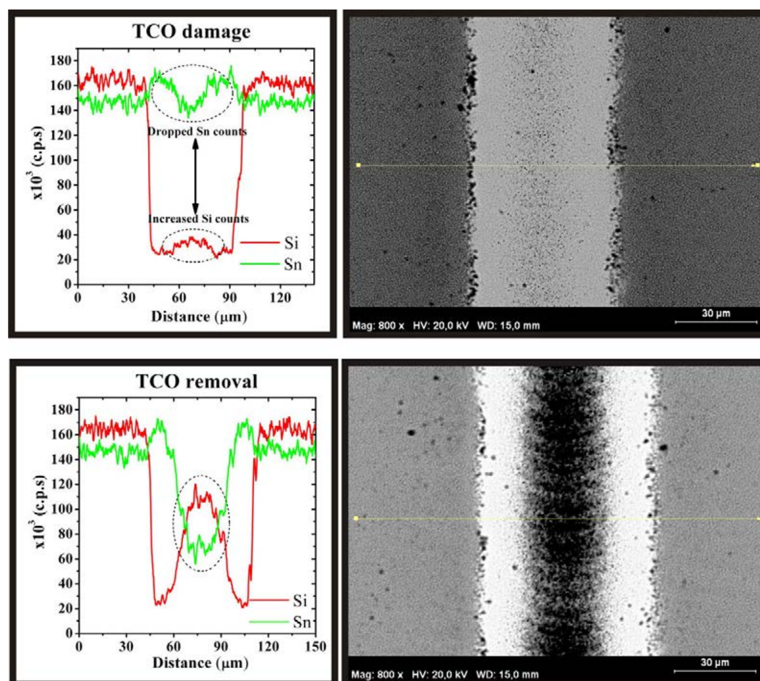

Figure 4.33: EDX profiles and SEM images of laser scribes at picosecond radiation of a-Si:H (pin)/Asahi-U/Glass to illustrate the damage on the TCO layer

Raman spectroscopy characterization has been performed for this laser step, in order to evaluate the state of the silicon layer in the vicinity of the groove. The damage of the silicon layer is assessed with the variation of the crystalline fraction resulting from the Raman spectra from the edge of the groove. Raman crystalline fraction has been calculated as it has been described in section 3.3.3. The increase of crystalline fraction entails a microstructural modification of the intrinsic material, mainly related to thermal effects. On this basis, these alterations of the remaining silicon could result in the reduction of the intrinsic material electrical resistance [65]. The study has been made for the optimal speed of process, increasing the energy to evaluate the state of the material. Fig. 4.34a shows the result for nanosecond results. Affected area has high values of crystalline fraction, for all the energy the crystalline fraction reach is 0.8. Particulary remarkable is the decreased of this affected area as long as the pulse energy increases. This is due to the Gaussian energy distribution of the pulse, as the total energy is increased, the tail of the Gaussian also acquire more energy capable to eliminate more material.

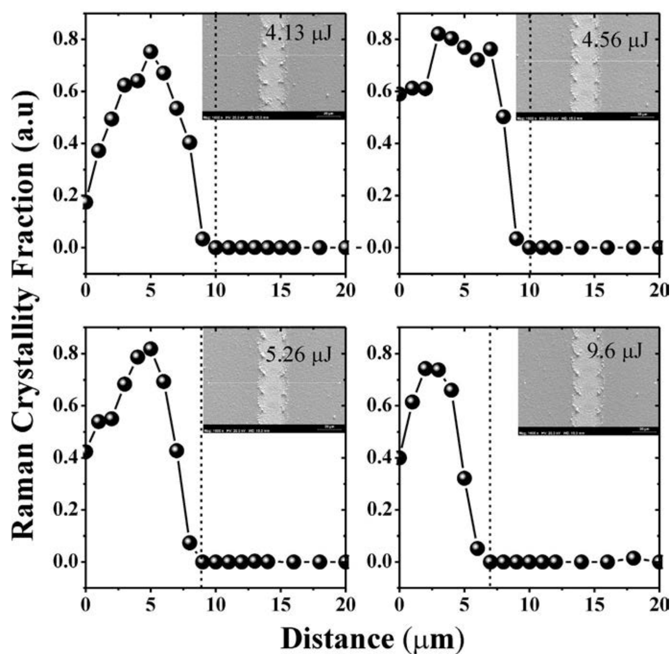

(a) Nanosecond pulses

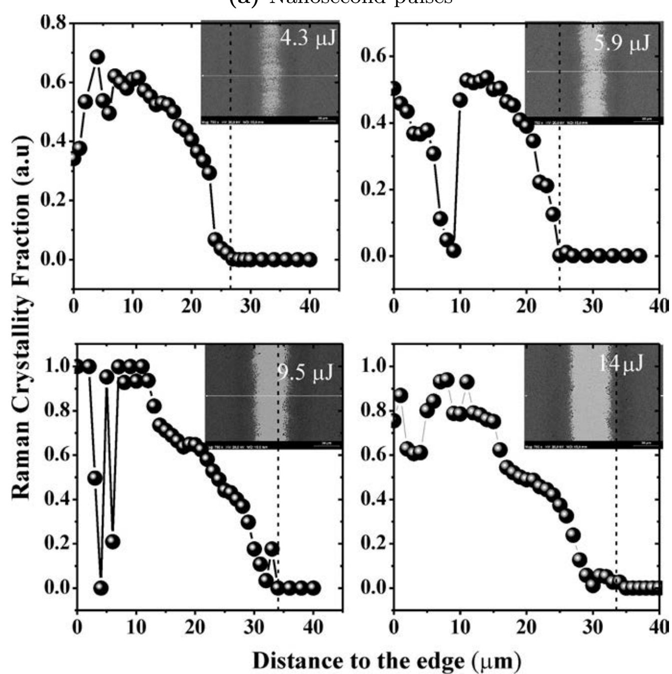

(b) Picosecond pulses

Figure 4.34: Raman crystalline fraction study of a-Si:H structure performed from the edge of the groove with ns and ps radiation for different energy conditions

If we compare the Raman crystalline fraction obtained for nanosecond radiation with the obtained for picosecond pulses, the results for similar pulse energy show lower values in the second case, when the energy increase this difference vanishes and the Raman crystalline fraction is very similar. This assessment indicates that there is an important affectation of the silicon structure around the laser scribing process and the affectation extents into the edge of the groove. However, as the P2 process takes place in the middle of the interconnection zone, where the area is inactive as a solar cell, the heat affected zone is not relevant.

4.3 Selective Ablation of Front Contact Characterization

As it has been noted throughout this work, the assessment of the laser scribing process in direct scribing configuration has its main value when it is performed in substrate deposition configuration where the front contact is a TCO to allow the entrance of light in the device. In fact, laser monolithic interconnection through back scribing laser process is already fully industrialized for superstrate configuration. On top of this, the main advantage of the direct laser scribing is to enable the use of opaque substrates along with the combination of new laser sources that can be absorbed by transparent substrates. For these two reasons, this process has logic only if the study is made on a device with a substrate configuration, hence the last step to obtain laser monolithic interconnection from the film side is the laser scribe isolation of a front contact TCO. Having said this, and taking into account where this thesis is framed, during the development of this work different types of samples have been made available in order to carry out to the maximum extent this task. However, to evaluate qualitatively the P3 process for substrate configuration, modules "ad-hoc" were used. In order to have a proof of concept, a study of laser scribing process was performed in commercial devices in superstrate configuration, where the assessment of P3 process via electrical characterization was able. Finally, the proof of concept of P3 laser process in a functional module in superstrate configuration was accomplished with all the laser steps performed in direct scribing configuration.

Attending to the characteristic of the samples where the studies have been carried out, the results are presented according to deposition sequence of the samples, characteristic of samples and provider are shown in table 3.1:

4.3.1 Substrate configuration

For substrate modules, two types of samples have been used, the first to be presented was deposited ”ad-hoc” for this purpose by the University of Barcelona see Fig. 4.35a. A commercial module unfinished, that is, without its last layer deposited, was used. The last layer was an AZO layer of 300 nm of thickness. Unfortunately, these modules were not functional, as their thickness not allowed electrical measurements. However, the selective ablation of the AZO layer over an active structure of amorphous silicon with Asahi-U TCO as back contact has been evaluated, giving information for future functional modules. The second kind of samples are commercial modules from Gadir Solar in substrate configuration, where the front contact layer was AZO and they were semitransparent; as the samples were commercial modules and the characteristics of the layer thickness and deposited method were unknown due to contractual terms of the engagement. Most of the samples were not electrically functional, and the few received with functionality could not be irradiated due to its protective coating from the production process that was not compatible with laser processes.

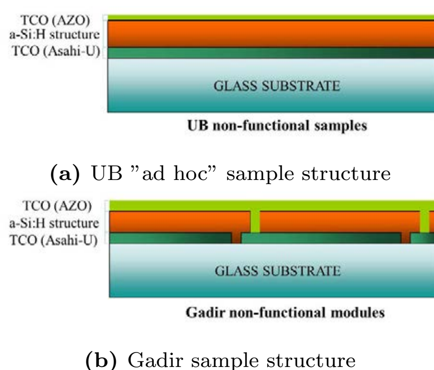

(a) UB ”ad hoc” sample structure

(b) Gadir sample structure

Figure 4.35: Samples used in substrate configuration.

According with the previous work, the assessment of this last laser process for the interconnection has been performed for two different laser sources, both of them working at 355 nm of wavelenght and two different pulse-width (nanosecond and picosecond). The achievement of the back contact selective ablation from the film side would suggest the feasibility of applying this approach to substrate configurations and the use of non-transparent substrates.

	Φ (J/cm^2)		Pulses per location		$\Phi(\Phi_{Th})$	
Laser sources	ns	ps	ns	ps	ns	ps
	0.71	0.96	1.03	1.04	3.8	3.0

Table 4.18: Laser parameter for the optimal scribes of P3 step over AZO layer of the ad-hoc module in terms of fluence (J/cm^2) and damage threshold values 0.184 and 0.324 J/cm^2 for ns and ps radiation

To characterize the selective removal of the front contact layer, the same is done attending to the morphology of the grooves with confocal microscopy, evaluating the complete removal of the layer by means of EDX profile analysis and measuring the changes on the material structure in the remaining a-Si:H at the bottom of the P3 scribe by means of Raman spectroscopy. Raman spectroscopy evaluates the state of the remaining silicon layer after irradiation. The damage of the silicon layer is assessed with the variation of the crystalline fraction resulting from the Raman spectra along the groove. The increase of the crystalline fraction entails a microstructural modification of the intrinsic material, mainly related to thermal effects. On this basis, these alterations of the remaining silicon could result in the reduction of the intrinsic material electrical characteristics [65].

4.3.1.1 Ad-hoc modules with AZO deposited by UB

The study has been done for different pulse energies and overlaps. Here will be presented the more representative results. Complete removal of AZO layer over the silicon structure was achieved for the two pulse-widths and the process parameters are collected in Table 4.18 in terms of fluence (J/cm^2) and damage threshold Φ_{Th}. The damage thresholds utilized are the ones presented in section 4.1.

The optimal scribes are shown in Fig. 4.36 for nanosecond and picoseconds radiation. These figures illustrate the selective ablation achievement of the TCO layer over the stack of the cell. In the figures, compositional characterization made by means of EDX profile analysis shows that both scribes (ns and ps) are free of AZO at its bottom and topographical characterization via confocal profiles exhibit not presence of ridges on the edge of the grooves.

By comparing the results at nanosecond and picosecond, it is shown that the overall morphological quality of the grooves obtained with both sources is similar, but paying

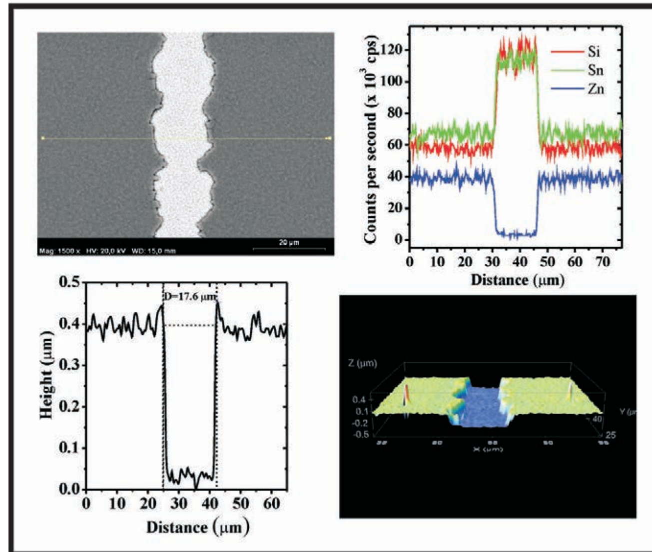

(a) Optimal selective removal of AZO over a-Si:H structure performed with nanosecond pulses

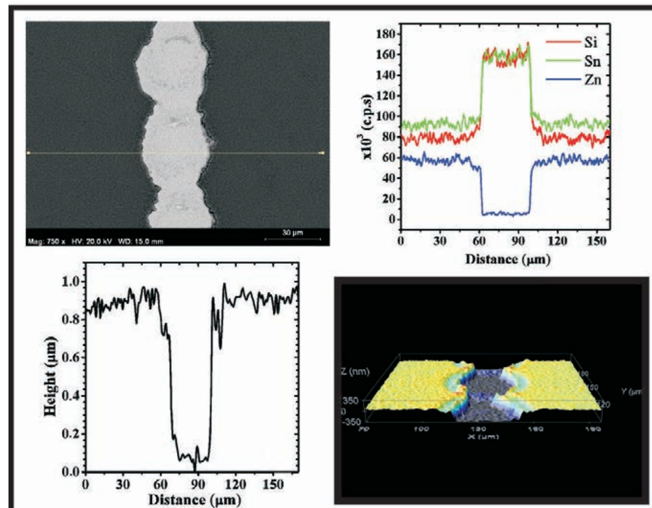

(b) Best result for AZO selective removal carried out with picosecond pulses

Figure 4.36: SEM image, EDX profile, Confocal profile and 3D topographical image for P3 laser scribing step for two different pulse-widths

attention to the confocal profiles and the topographical images it is seen that the quality of the groove for nanosecond radiation is slightly better, since the Gaussian profile of the laser beam on the edges of the grooves is more pronounced in the case of picosecond radiation due to its bigger spot. This phenomenon, common to most of the laser sources with Gaussian beams, could be avoided by using a laser beam shaper to get a good homogeneity of the laser profile. Although achieving this for UV wavelength is still a challenge, it is considered for future experiments.

However attending to Raman spectroscopy (Fig. 4.37) of the optimal grooves in the two regimes, it is particularly remarkable the low values obtained for the crystalline fraction; less than 0.2 in the lower energies for both pulse durations. Comparing these results with the ones obtained by laser back-scribing performed at 532 nm [17], the crystalline fraction generated with 355 nm just in the middle of the ablated groove is considerably lower than at the edge of the groove with 532 nm and nanosecond radiation, where the values of the fraction reach up to 0.8. It must be pointed out the difference in the maximum values of crystalline fraction in the center of the grooves for picosecond and nanosecond, for a similar increment in energy at two pulse-width, in picosecond the maximum value is appreciable lower. This suggests that picosecond radiation generate less affectation in the amorphous silicon layer.

The results obtained in this study are very promising due the good morphology achieved for this wavelength, and the excellent control of the selective ablation. This encourage us to keep working in this line.

4.3.1.2 Commercial modules from GADIR

As described above, the commercial modules from Gadir Solar were studied to have a proof of concept of the P3 laser step in direct scribing configuration. Unfortunately, when this study was being carried out the company closed down, and the supply of samples was finished reducing the time to perform the experiments. The experiments were formulated according to previous results obtained with the ad-hoc modules deposited by University of Barcelona. However, the results showed that the previous laser parameters did not achieved the selective removal of the AZO layer, requiring more energy and even multiscribes at the same P3 process. This suggests the importance of the deposit of the layers, since even with the same material, the process parameters can changed dramatically, as it will be shown below.

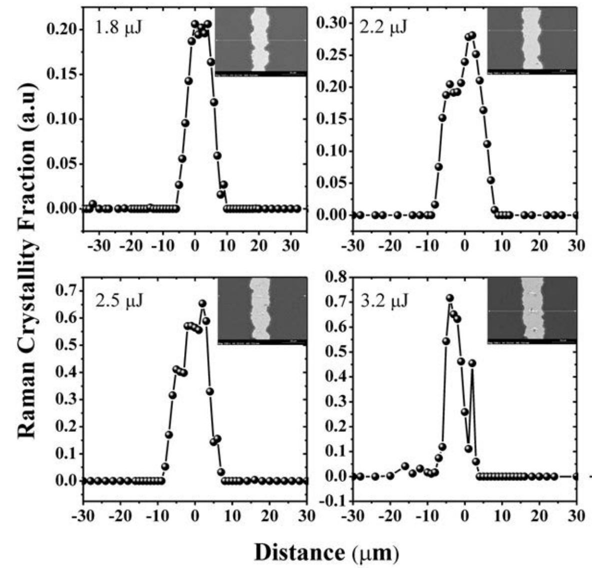

(a) Nanosecond pulses

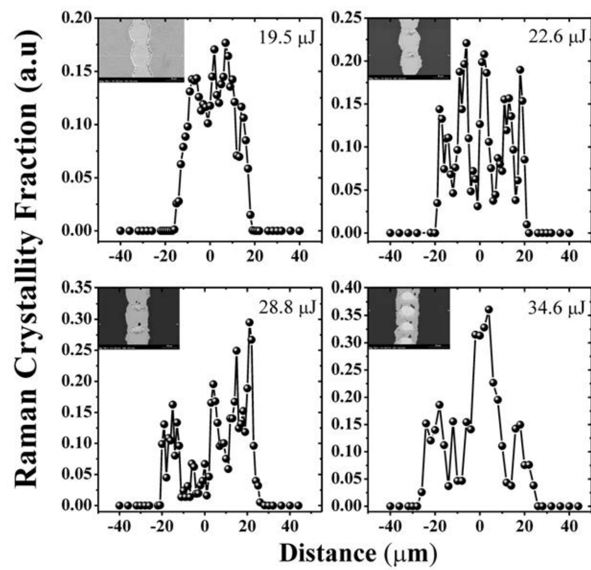

(b) Picosecond pulses

Figure 4.37: Raman crystalline fraction study of a-Si:H structure performed with ns and ps pulses for different energy conditions

As it has been performed for the rest of laser scribing process, the evaluation has been done in two different regimes of pulse-width, obtaining the best results for picosecond radiation and an ultrasonic cleanning during 40 min. The result is shown in Fig. 4.38. In this case, the a-Si:H layer underneath the laser groove is completely removed, as EDX profile demonstrates. It is observed the presence of flakes, whose effect has been studied by [25] in superstrate configuration, hence this presence must be deeply evaluated in functional modules.

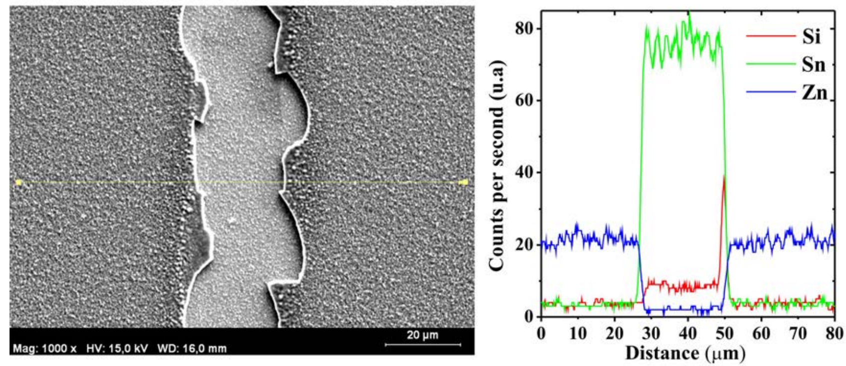

Figure 4.38: SEM image and EDX profile picosecond scribe with 100KHz of repetition rate 250 mm/s of speed process and 600 mW two lines overlapped and 30 minutes of Ultrasonic cleaning

In order to evaluate the remainning state of the surrounding area of the P3 laser scribing and the effect on it of two lines overlapped and ultrasonic cleaning, Raman crystalline fraction has been calculated. The results can be seen in Fig. 4.39 where Raman crystalline fraction shows that the remaining material has not been affected, as the value of the same is near zero.

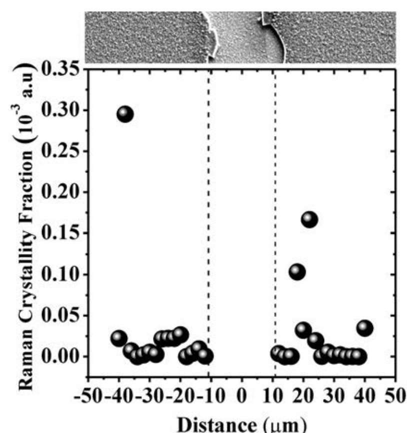

Figure 4.39: Crystalline fraction assessment of a-Si:H structure in the vicinity of the groove

4.3.2 Superstrate configuration

In this assessment the samples used were cells and modules in superstrate configuration, the scheme of the samples is shown in Fig. 4.40, where the front contact was Aluminium. Samples prepared by Ciemat and commercial modules from T-solar has been utilized to have a proof of concept capable to demonstrate the viability of laser direct scribing process. These samples gave the possibility to evaluate electrically the laser process.

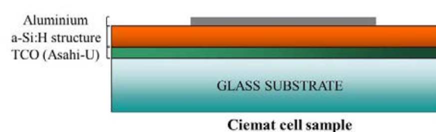

(a) Ciemat cell sample structure

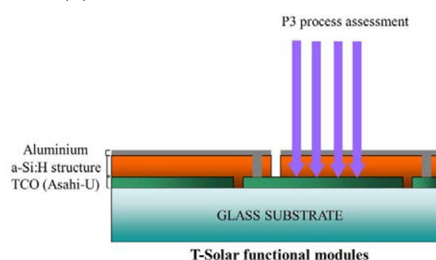

(b) T-Solar module structure

Figure 4.40: Samples used in superstrate configuration.

P3 laser step has been evaluated at 355 nm of wavelength and in concordance with

this document for nanosecond and picosecond pulses.

The Aluminium damage threshold have been obtained in the same way than for the rest of materials, obtaining $\Phi_{Th} = 0.62$ J/cm^2 for nanosecond radiation and $\Phi_{Th} = 0.14$ J/cm^2 for picosecond pulses shown in Fig. 4.41. This difference is due to the reduce heat losses into the surrounding material governed by the shorter pulses [35]. The results are consistent with this difference, suggesting less energy necessary to remove or eliminate Aluminium layer with picosecond laser.

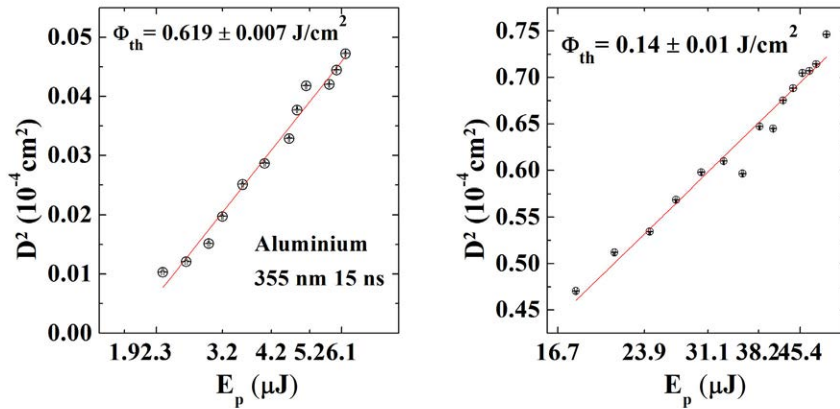

Figure 4.41: Damage threshold result for Aluminum layer obtained for nanosecond and picosecond radiation

At first, P3 laser process was performed with nanosecond radiation (HIPPO system) over lab cells deposited in Ciemat. In order to have a electrical measurement, and assess the influence of the P3 laser step over the nominal curve I-V of the cell, at that time, the electrical measurement could only be done in dark current configuration. The sketch of the experiments is shown in Fig. 4.42, in the figure can be seen concentric circles which relate to the different laser processes, carried out at different energies starting from less to higher energies. After each circular scribe the dark I/V curve is measured and the results are represented in the Fig. 4.42. As expected, the higher the energy, the larger the damage over the material [14].

Nevertheless the morphological aspects, seen in Fig. 4.43 show accumulation of Aluminium on the edge of the groove demonstrated by means of EDX profile. Being this, the probable cause of the damage of the cell.

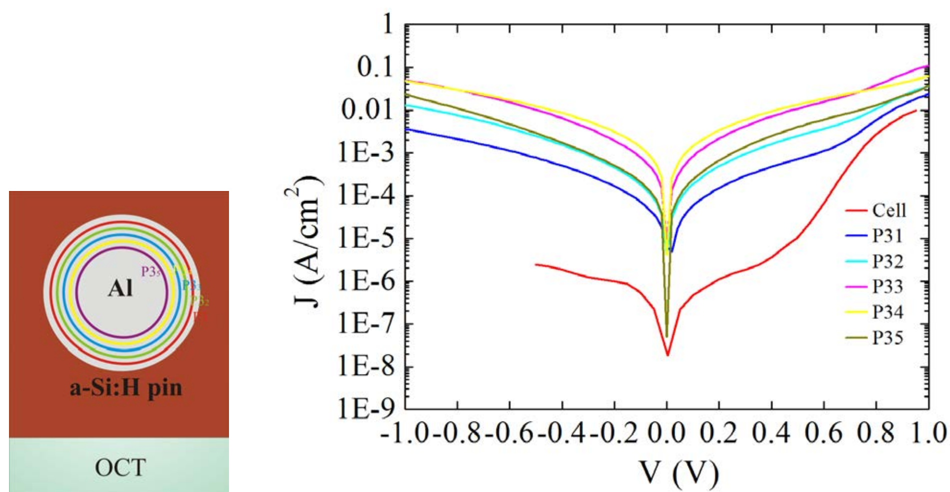

Figure 4.42: Sketch of P3 experiments over a cell with Aluminium layer as back contact with its corresponding electrical characterization by means of dark current curves.

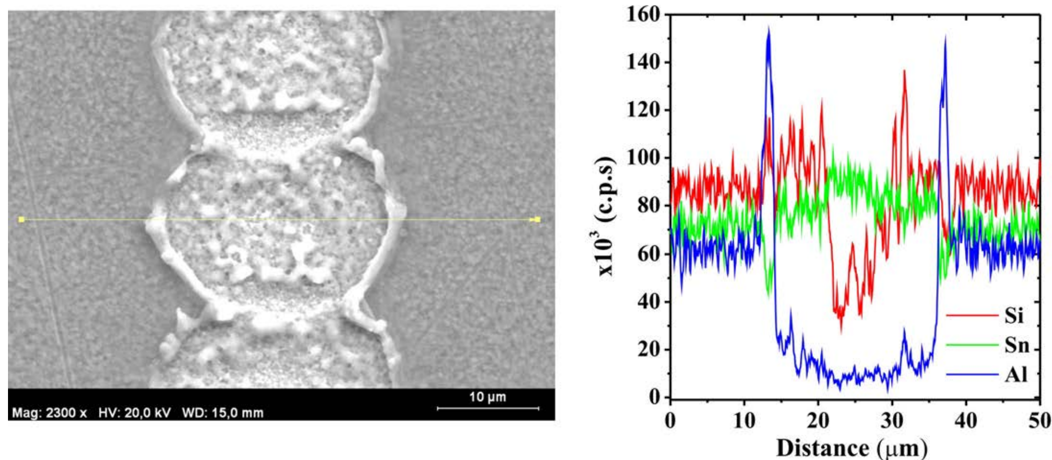

Figure 4.43: SEM image and EDX profile of the best laser scribe performed at 496 mW, 50KHz, 30% overlap

This study did not have in consideration the acceleration effect introduce by the scanner head, lately this was found crucial by [23] as was so the effect of accumulation that the lines introduce in the cell, describe as well in the cited work.

In order to improve the laser scribing characteristics, laying in the difference in the

damage threshold, the following results were performed at picosecond radiation. In this case, the experiments have been carried out in commercial modules in superstrate configuration from T-Solar, where the modules are finished and functional, but allowing the measurement when another P3 step is performed just closed to the already done.

The modules (100 X 100 mm) have six individual cells of (7 x 1) cm^2 that were previously measured its current-voltage (J-V) characteristics under calibrated 100 mW/cm^2 AM 1.5 G irradiance.

In order to achieve a correct interconnection, without damage of the cell performance and hence the module efficiency, different experiments have been designed. First was to evaluate the influence of pulses with different energies without overlap, in order to eliminate the possible effect that overlapping pulses could introduce in the final process. This would give information about the accumulation of damage introduce by single pulses. Secondly the influence of pulse number was assessed by performing multiple scribes within a cell with the purpose of delimiting the accumulation of damage for different fluences of pulses.

Figure 4.44 shows the study performed for several energies per pulse for just one line over the cells, the results showed that for all the energies studied there was no significant damage as seen in the J-V characteristics of the cells, just a slight separation from the raw cell curve is seen, highlighted in the zoomed area of the graph in Fig. 4.44.

When it came to the study of the number of pulses accumulation three laser fluences of picosecond pulses were assessed adding new process to the previous measured. Each process introduced 500 pulses aproximately with no overlap. When the fluence increases the damage of the cells assessed by its J V characteristic, is bigger. For 2.83 J/cm^2 the biggest one, the J-V characteristic for 2 processes appeared short-circuited (Fig. 4.45a), for 2.29 J/cm^2 the graph shows no short-circuited cells, however the separation of the curves as the number of processes increased (i.e. more number of pulses) leads the series resistance of the cells increase, observed in Fig. 4.45b. Finally, a fluence with no damage of the cells was found, in Fig. 4.45c can be seen no differences between the curves, which reveals no dependence with the number of pulses.

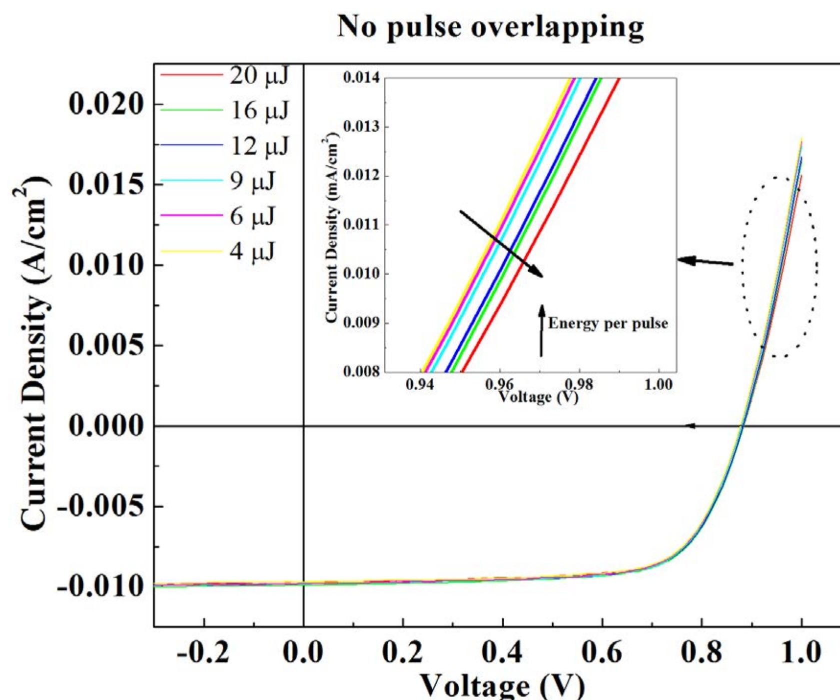

Figure 4.44: J-V characteristic where pulse energy assessment has been performed with picosecond 355 nm radiation

Attending to these results, the laser parameters for a functional P3 with optimum overlapped pulses were set. Finally, P3 in direct scribing configuration and picosecond radiation was achieved for modules from T-Solar, and the morphological aspects can be seen in the Fig. 4.46. There is an ablation of the TCO front contact layer in the area were the overlapped is produced, this could led to an increase in the series resistance of the final device. This effect will be avoid in the final process, however in these samples this effect could not be eliminated.

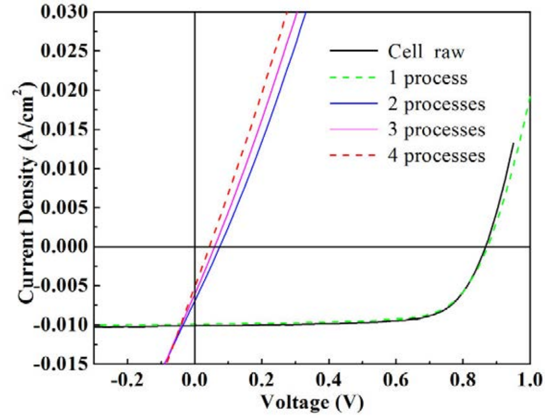

(a) Effect of number of pulses ϕ = 2.83 J/cm^2

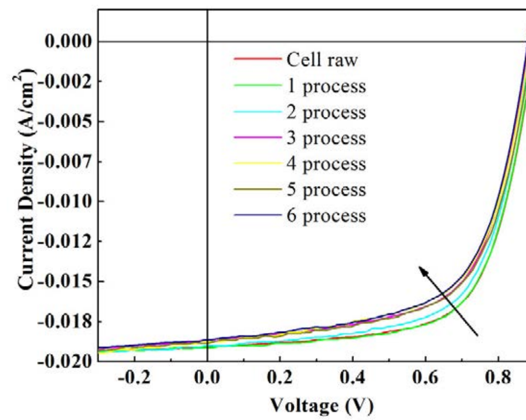

(b) Effect of number of pulses ϕ = 2.29 J/cm^2

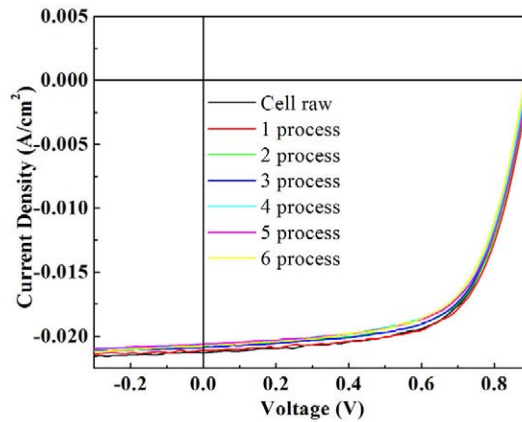

(c) Effect of number of pulses ϕ = 1.46 J/cm^2

Figure 4.45: J-V characteristic for multiples lines in a cell for three different fluences of picosecond 355 nm radiation

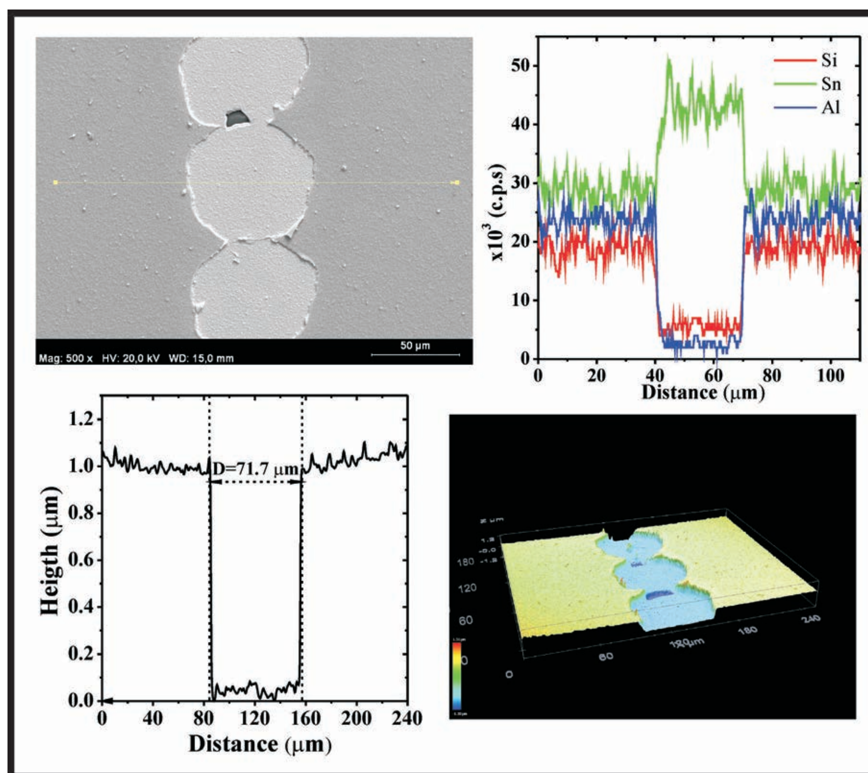

Figure 4.46: SEM image, EDX profile and 3D image and depth Confocal profile performed with laser parameters obtained by the presented study for T-Solar modules.

4.3.2.1 Laser direct scribing interconnection of a complete module in superstrate configuration

As a proof of concept, the results obtained in T-Solar modules were transferred to Ciemat device to interconnect a module through laser direct scribing. Three steps for the interconnection were performed in direct scribing configuration with 355 nm picosecond laser source. The P3 was done over the back contact, an Aluminium layer of 120 nm of thickness, the structure is depicted in the Fig. 4.47a and the sample details are presented in 3.1. The module dimensions were 100 x 100 mm^2 and eight cells were isolated and interconnected to achieve a complete module (Fig. 4.47b).

This module has been interconnected by laser direct scribing at 355 nm of wavelength and picosecond pulses. The same laser source (Lumera Super Rapid) has been used for the three steps of the interconnection. The laser parameters utilized in the three steps of the interconnection were the obtained over this thesis and are resumed in

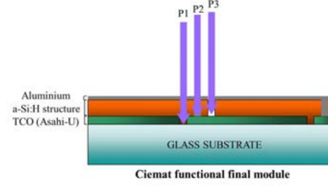

(a) Module structure and laser process step configuration.

(b) Image of the final device.

Figure 4.47: Structure and picture of the final module interconnected performed by means of laser direct scribing at 355 nm and picosecond pulses.

	Φ (J/cm^2)	**Overlap %**
P1 (Asahi-U)	1.516	88.2
P2	1.26	10
P3	1.46	5

Table 4.19: Laser parameter for the optimal scribes P1 over Asahi-U, P2 and P3 over Aluminum.

table 4.19. The morphological characterization is observed via SEM and topographical images in Fig. 4.48 and 4.49. The results showed good edge profiles.

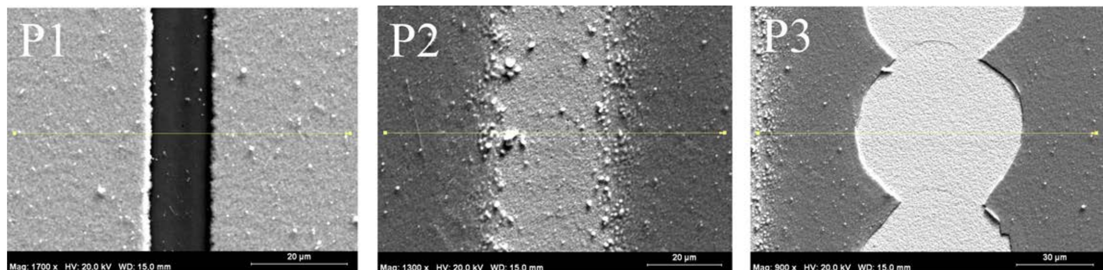

Figure 4.48: SEM images of the three steps of the laser monolithic interconnection.

The electrical characterization has been carried out for each cell individually, the J-V characteristic curves are presented in Fig. 4.50 and their corresponding values are

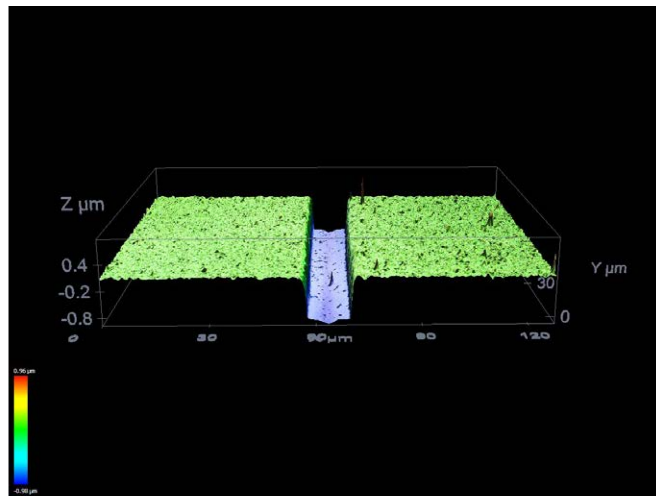

(a) 3D topographical image of P1 process

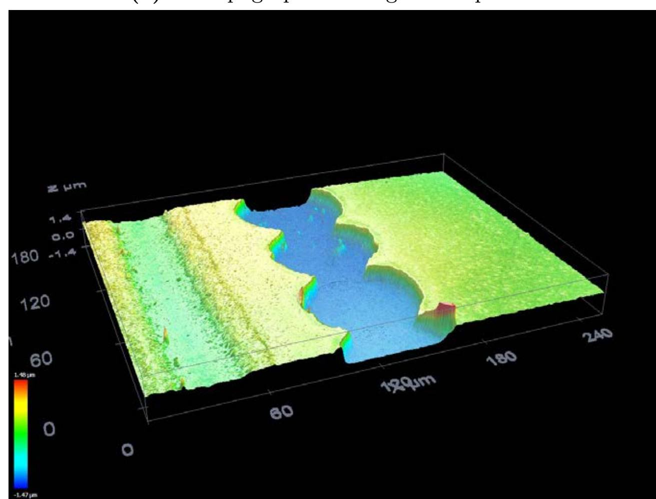

(b) 3D topographical image of P2 presented on the left and P3 next to the same

Figure 4.49: Confocal characterization of laser interconnection process in direct scribing configuration by means of 3D topographical images of the three laser steps carried out in the final device.

detailed in table 4.20. Efficiencies for individual cells with no laser process performed by Ciemat were 8 % approximately, the results obtained with the three laser steps for the interconnection show a slight affectation on the electrical properties of the individual cells. And finally the complete module has been characterized electrically presented in Fig. 4.51 with its more representative values. These measurements were performed in the Ciemat facilities in order to have reliable results.

Cell	1	2	3	4	5	6	7	8
I_{sc} (A)	0.13	0.12	0.12	0.13	0.12	0.12	0.13	0.12
V_{oc} (V)	0.83	0.77	0.79	0.82	0.81	0.82	0.82	0.83
FF(%)	48.06	37.56	38.06	45.40	44.20	42.67	41.87	43.78
Effic.(%)	6.88	4.60	4.85	6.38	5.99	5.67	5.84	5.86

Table 4.20: I-V relevant characteristics for the eight cells which compone the functional module, each cell has 7.5 cm^2 of area

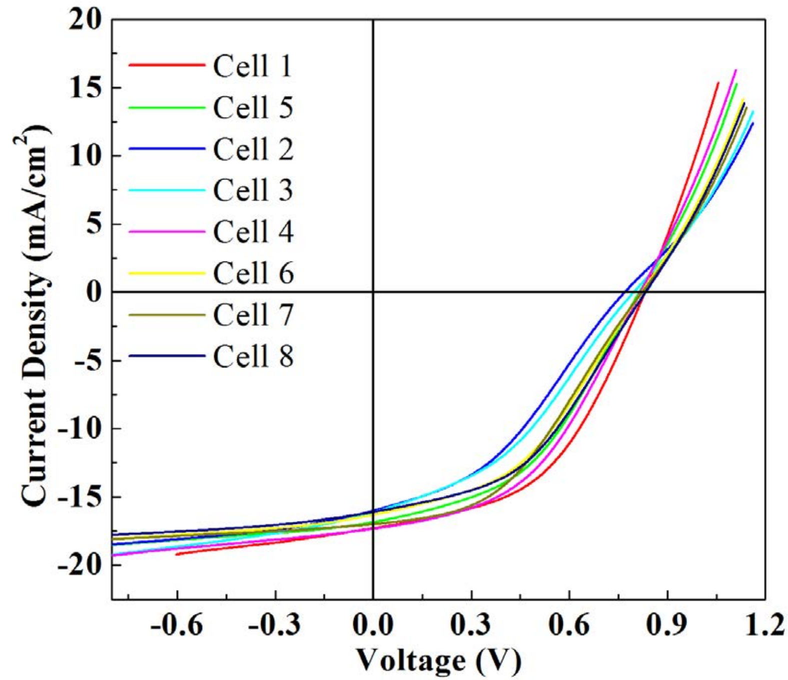

Figure 4.50: J-V characteristics of the cells which make up the complete module

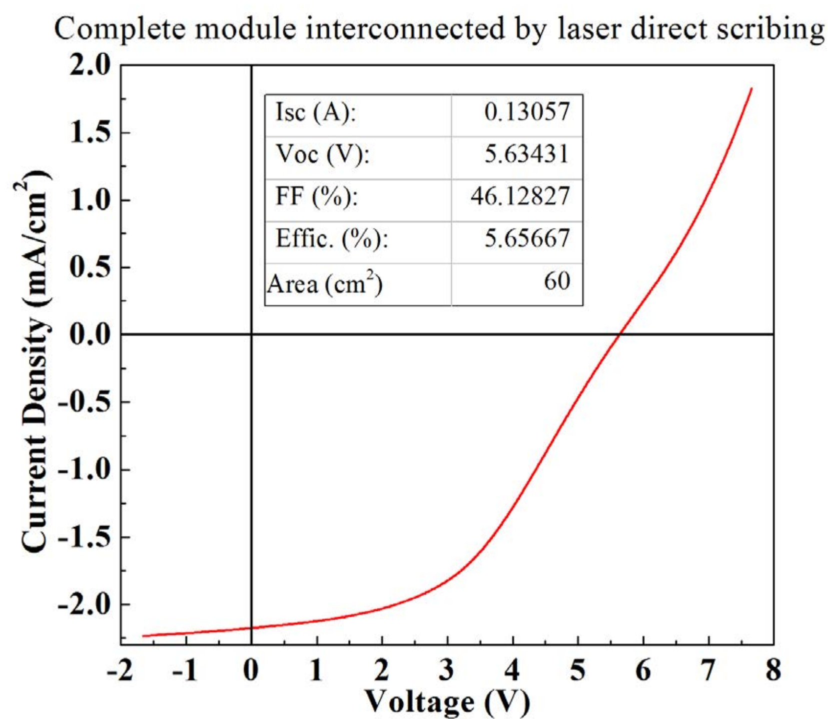

Figure 4.51: J-V characteristic of the functional module fully interconnected by laser direct scribing with 355 nm and picosecond pulses

5

Conclusions

Three processes: P1, P2 and P3, have been developed in order to achieve the interconnection of photovoltaic devices based on a-Si:H, with irradiation from the film side and fully based on the use commercial UV laser sources. More in detail, the optimal conditions for the first step of the interconnection have been established for three TCO materials (Asahi-U, ITO and AZO), with good galvanic isolation to define the cells. The best edge profile of the groove was obtained with picosecond UV irradiation. The selective ablation of the a-Si:H layer has been developed with best groove results for picosecond radiation, with good edge profiles and no damage of the TCO underneath. Micro-raman spectroscopy showed less affectation for this irradiation as well. At last, P3 has been demonstrated to be feasible for two different configurations and two materials, AZO and Aluminium, achieving as a proof of concept a functional P3 over Aluminium in direct scribing configuration and picosecond UV laser source. In particular, it is especially remarkable the development of the process for P1 with UV sources, as this can be applied for all kind of configurations in substrate and superstrate configuration. In fact, the author's contribution [51] is the first publishing in this regard at international scientific level, demonstrating the possibility of substituting with competitive advantage the processes carried out to date with IR sources by using laser UV processes, which nowadays implies a fully industrialized approach.

The laser processes developed in this thesis are optimal for its application on devices deposited over opaque and flexible substrates. The circumstances where this work has been developed, led to demonstrate the acceptability of the process on "ad-hoc" devices, especially designed under the collaboration with CIEMAT and UB groups mentioned in

this work. Additionally, this has led to the demonstration of the possibility to consider the interconnection processes through direct ablation with metal layers in the structure which, given the strong thermal character of the laser-metal interaction in the range of scope, can be considered an achievement of notable scientific relevance. The validity of the same has been evidenced by means of the interconnection of a standard pin module over glass in irradiation from the film side. The efficiency losses of this module are due, fundamentally, to the interaction of the metal layer of the back contact. It is considered that in nip structures the behaviour will be better, since in such devices the front contact is a TCO, material with which it has been demonstrated the feasibility of selective ablation without effects on the underlying layers.

Part of the work developed in this thesis has served as a basis for the realization of the first interconnection in Spain of an a-Si:H module with fully Spanish technology in the context of following public funding projects:

- Proyecto Singular Estratégico PSE-MICROSIL08 (PSE-120000-2006-6)
- Proyecto INNDISOL (IPT-420000-2010-6)
- AMIC (ENE2010-21384-C04-02)
- CLÁSICO (ENE2007-6772-C04-04)

In addition to this, the performed studies allow the extrapolation of the selective ablation conditions to other photovoltaic technologies over flexible substrates, like CdTe and CIS/CIGS, which is an area on which the author of this work is currently investigating. Apart from the general conclusions previously described, some other particular findings of scientific interest can be enumerated. Firstly, the need to adapt well established material characterization techniques, like scanning confocal spectroscopy, EDX techniques or Raman spectroscopy, to the working particular conditions, has led to define original adaptations of these techniques (like the combined use of EDX and confocal spectroscopy), suitable for the characterization of selective ablation processes of materials in thin layer. The use of Raman spectroscopy techniques to determine the damaged induced over the Silicon layer is totally original (see SPIE publishing) and opens the door to future designs of characterization and control processes in the industrial environment. Lastly, the work performed in the systematic study of OCT ablation

from the film side is of high relevance, not only in the scope of photovoltaic devices, but also in the development of other optoelectronic devices, like matrix positioning sensors from which, in fact, derives the original idea that was the germ of this thesis.

6

Lines of Future Development

After the work developed in this thesis an important line of future development would be the transference of the results obtained for the a-Si:H thin film technology to chalcogenide technology, being this one of the most economically viable technologies at present. This transference would offer the possibility of using flexible substrates to the thin film photovoltaic technology.

Another alternative for future is to capitalize the results obtained in TCO analysis and the degree of knowledge acquired during the same, opening the door to their application in the flexible microelectronic industry, which is expected to have a significant growth in the next few years.

As a third line, the degree of optimization achieved in the selective ablation process allows to propose novel applications of the photovoltaic devices in the field of building integration, especially of those which leverage the effects of controlled transparency.

Lastly, we could purpose the application of the knowledge acquired in selective ablation of thin film layers to the crystalline silicon photovoltaic technologies, in particular the ones based in heterojunction cells with interdigitated back contact cells (IBC), technology that is currently focusing the interest of the scientific community within the photovoltaic area [30].

It is important to highlight that the research group to which the author belongs has already initiated works on all these areas.

List of Publications

[1] S. Lauzurica, J.J. García-Ballesteros, M. Colina, I. Sánchez-Aniorte, and C. Molpeceres. **Selective ablation with UV lasers of a-Si:H thin film solar cells in direct scribing configuration**. *Applied Surface Science*, **257**(12):5230 – 5236, 2011. E-MRS 2010 Spring Meeting Symposium R.

[2] S. Lauzurica and C. Molpeceres. **Assessment of laser direct-scribing of a-Si:H solar cells with UV nanosecond and picosecond sources**. *Physics Procedia*, **5**(Part 1):277 – 284, 2010. Laser Assisted Net Shape Engineering 6, Proceedings of the LANE 2010, Part 1.

[3] J.J. García-Ballesteros, I. Torres, S. Lauzurica, D. Canteli, J.J. Gandía, and C. Molpeceres. **Influence of laser scribing in the electrical properties of a-Si:H thin film photovoltaic modules**. *Solar Energy Materials and Solar Cells*, **95**(3):986 – 991, 2011. 96

[4] C Molpeceres, S Lauzurica, JL Ocana, JJ Gandia, L Urbina, and J Carabe. **Microprocessing of ITO and a-Si thin films using ns laser sources**. *J. Micromech. Microeng*, **15**(6):1271–1278, JUN 2005. 1, 49, 105

[5] C. Molpeceres, S. Lauzurica, J.J. García-Ballesteros, M. Morales, G. Guadaño, J.L. Ocaña, S. Fernández, J.J. Gandía, F. Villar, O. Nos, and J. Bertomeu. **Selective ablation of photovoltaic materials with UV laser sources for monolithic interconnection of devices based on a-Si:H**. *Materials Science and Engineering: B*, **159-160**:18 – 22, 2009. EMRS 2008 Spring Conference Symposium K: Advanced Silicon Materials Research for Electronic and Photovoltaic Applications.

[6] C. Molpeceres, S. Lauzurica, J.J. García-Ballesteros, M. Morales, and J.L. Ocaña. **Advanced 3D micromachining techniques using UV laser sources**. *Microelectronic Engineering*, **84**(5-8):1337 – 1340, 2007. Proceedings of the 32nd International Conference on Micro- and Nano-Engineering.

[7] C. Molpeceres, S. Lauzurica, J.J. Garcia-Ballesteros, M. Morales, S. Fernandez-Robledo, J.L. Ocaña, J.J. Gandia, J. Carabe, F. Villar, J. Escarre, J. Bertomeu, and J. Andreu. **New techniques for laser microprocessing of photovoltaic devices based on thin-film a-Si:H**. *Applied Surface Science*, **254**(4):1115 – 1120, 2007. ¡ce:title¿Laser synthesis and processing of advanced materials¡/ce:title¿ ¡ce:subtitle¿E-MRS-P Symposium¡/ce:subtitle¿.

[8] C. Molpeceres, S. Lauzurica, J.A. Porro, and J.L. Ocaña. **Metrologic assessment of high power laser generated surface roughness by confocal laser scanning microscopy**. In A. Mendez-Vilas, editor, *Recent Advances in Multidisciplinary Applied Physics*, pages 133 – 140. Elsevier Science Ltd, Oxford, 2005.

[9] C. Molpeceres, M.I. Sanchez, M. Morales, D. Muñoz-Martin, S. Lauzurica, I. Martin, P. Ortega, M. Colina, C. Voz, and R. Alcubilla. **Parameterization of local laser doping and laser-fired contacts for high efficiency c-Si solar cells**. *Physics Procedia*, **39**(0):693 – 701, 2012. Laser Assisted Net shape Engineering 7 (LANE 2012).

[10] C. L. Molpeceres, M. Colina, M. Holgado, M. Morales, I. Sanchez-Aniorte,S. Lauzurica, J. J. Garcia-Ballesteros, J. L. Ocaña *Optical characterization of the heat-affected zone in laser patterning of thin film a-Si:H*, **7202**. SPIE, 2009. 41

References

[1] Z. Geretovszky A. Buzás. **Patterning ZnO layers with frequency doubled and quadrupled Nd:YAG laser for PV application**. *Thin Solid Films*, **515**:8495–8499, 2007. 49

[2] S. Nakade A. D. Compaan, I. Matulionis. **Laser scribing of polycrystalline thin films**. *Optics and Lasers in Engineering*, **34**(1):15 – 45, 2000. 2

[3] I. Matulionis A.D. Compaan and S. Nakade. **Optimization of Laser Scribing for Thin-Film PV Modules**. Technical report, National Renewable Energy Laboratory, 1998. 9, 53

[4] Y. V. Afanasiev, B. N. Chichkov, V. A. Isakov, A. P. Kanavin, and S. A. Uryupin. **Thermal regime of laser ablation of metals by ultrashort pulses of low fluence**. *Journal of Russian Laser Research*, **20**(3):189–201, May 1999. 14

[5] P. B. Allen. **Theory of Thermal Relaxation of Electrons in Metals**. *Physical review letters*, **59**:1460–1463, 1987. 14

[6] J. E. Andrew, P. E. Dyer, R. D. Greenough, and P. H. Key. **Metal film removal and patterning using a XeCl laser**. *Applied Physics Letters*, **43**(11):1076–1078, 1983. 1

[7] S. I. Anisimov and B.S. Luk'yanchuk. **Selected problems of laser ablation theory**. *Physics-Uspekhi*, **45**(3):293, 2002. 14, 16

[8] M. Vanecek J. Meier E. Vallat-Sauvain N. Wyrsch U. Kroll C. Droz J. Bailat A.V. Shah, H. Schade. **Thin-film silicon solar cell technology**. *Progress in Photovoltaics: Research and Applications*, **12**(2-3):113–142, 2004. 5

[9] S. Nolte F. von Alvensleben-A. Tünnermann B. N. Chichkov, C. Momma. **Femtosecond, picosecond and nanosecond laser ablation of solids**. *Applied Physics A: Materials Science & Processing*, **63**(2):109 –115, 1996. 14

[10] D. Baüerle. *Laser Processing and Chemistry.* Springer Berlin, 2000. 16, 17

[11] A. De Bonis, A. Galasso, V. Marotta, S. Orlando, A. Santagata, R. Teghil, S. Veronesi, P. Villani, and A. Giardini. **Pulsed laser ablation of indium tin oxide in the nano and femtosecond regime: Characterization of transient species**. *Applied Surface Science*, **252**(13):4632 – 4636, 2006. Proceedings of the European Materials Research society 2005 - Symposium-J: Advances in Laser and Lamp Processing of Functional Materials - EMRS 2005 Symposium J. 50

[12] J.P. Borrajo, M. Vetter, and J. AndreuCompaan2006. **Laser scribing of very large 2,6m x 2,2m a-Si: H thin film photovoltaic modules.** *Electron Devices, 2009. CDE 2009. Spanish Conference on*, pages 402 –405, feb. 2009. 8

[13] J. Bovatsek, A. Tamhankar, R.S. Patel, N.M. Bulgakova, and J. Bonse. **Thin film removal mechanisms in ns-laser processing of photovoltaic materials**. *Thin Solid Films*, **518**(10):2897 – 2904, 2010. 9

[14] K. Brecl, M. Topic, and F. Smole. **A detailed study of monolithic contacts and electrical losses in a large-area thin-film module**. *Progress in Photovoltaics: Research and Applications*, **13**(4):297–310, 2005. Faculty of Electrical Engineering, University of Ljubljana, Tržascaronka 25, 1000 Ljubljana, Slovenia. 9, 95

[15] E. Bustarret, M. A. Hachicha, and M. Brunel. **Experimental determination of the nanocrystalline volume fraction in silicon thin films from Raman spectroscopy**. *Applied Physics Letters*, **52**(20):1675–1677, 1988. 40

[16] H. W. Choi, D. F. Farson, J. Bovatsek, A. Arai, and D. Ashkenasi. **Direct-write patterning of indium-tin-oxide film by high pulse repetition frequency femtosecond laser ablation**. *Appl. Opt.*, **46**(23):5792–5799, 2007. 64

[17] M. Colina, C. Molpeceres, M. Holgado, J. Gandia, O. Nos, and J.L. Ocana. **Study of the refractive index change in a-Si:H thin films patterned by 532 nm laser radiation for photovoltaic applications**. *Thin Solid Films*, **518**(18):5331 – 5339, 2010. 91

[18] A. D. Compaan. **Photovoltaics: Clean power for the 21st century**. *Solar Energy Materials and Solar Cells*, **90**(15):2170 – 2180, 2006. Selected Papers from the Solar Cells and Solar Energy Materials Symposium -IMRC 2005. 5

[19] A.D. Compaan, M.J. I. Matulionis, Miller, and U.N. Jayamaha. **Optimization of laser scribing for thin-film photovoltaics**. *Photovoltaic Specialists Conference, 1996., Conference Record of the Twenty Fifth IEEE*, pages 769–772, May 1996. 8

[20] P. B. Corkum, F. Brunel, N. K. Sherman, and T. Srinivasan-Rao. **Thermal Response of Metals to Ultrashort-Pulse Laser Excitation**. *Phys. Rev. Lett.*, **61**(25):2886–2889, Dec 1988. 16

[21] J. E. Fredrickson, C. N. Waddell, W. G. Spitzer, and G. K. Hubler. **Effects of thermal annealing on the refractive index of amorphous silicon produced by ion implantation**. *Applied Physics Letters*, **40**(2):172–174, 1982. 45

[22] M. Fujimaki, Y. Nishihara, Y. Ohki, J. L. Brebner, and S. Roorda. **Ion-implantation-induced densification in silica-based glass for fabrication of optical fiber gratings**. *Journal of Applied Physics*, **88**(10):5534–5537, 2000. 45

[23] J.J. García-Ballesteros, I. Torres, S. Lauzurica, D. Canteli, J.J. Gandía, and C. Molpeceres. **Influence of laser scribing in the electrical properties of a-Si:H thin film photovoltaic modules**. *Solar Energy Materials and Solar Cells*, **95**(3):986 – 991, 2011. 96

[24] S. Golay, J. Meier, S. Dubail, S. Fay, U. Kroll, and A. Shah. **First pin/pin micromorph modules by laser patterning**. *Photovoltaic Specialists Conference, 2000. Conference Record of the Twenty-Eighth IEEE*, pages 1456 – 1459, 2000. 8

[25] S. Haas, A. Gordijn, and H. Stiebig. **High speed laser processing for monolithical series connection of silicon thin-film modules**. *Progress in Photovoltaics: Research and Applications*, **16**(3):195–203, 2008. 93

[26] R.F. Haglund, J.C. Miller, T. Lucatorto, and M. De Graef. *Laser Ablation and Desorption*. Experimental Methods in the Physical Sciences. Elsevier Science, 1997. 16

[27] E. Hecht. *Optics*. Addison-Wesley Longman, Incorporated, 2002. 43

[28] S. Hegedus. **Thin Film Solar Modules: The Low Cost, High Throughput and Versatile Alternative to Si Wafers**. *Progress in Photovoltaics: Research and Applications*, **14**:393–411, 2006. 5

[29] J. Hermann, M. Benfarah, G. Coustillier, S. Bruneau, E. Axente, J.-F. Guillemoles, M. Sentis, P. Alloncle, and T. Itina. **Selective ablation of thin films with short and ultrashort laser pulses**. *Applied Surface Science*, **252**(13):4814 – 4818, 2006. Proceedings of the European Materials Research society 2005 - Symposium-J: Advances in Laser and Lamp Processing of Functional Materials - EMRS 2005 Symposium J. 54

[30] S. Hermann, N. Harder, R. Brendel, D. Herzog, and H. Haferkamp. **Picosecond laser ablation of SiO_2 layers on silicon substrates**. *Applied Physics A*, **99**:151–158, 2010. 109

[31] M. Holgado, R. Casquel, B. Sánchez, C. Molpeceres, M. Morales, and J. L. Oca na. **Optical characterization of extremely small volumes of liquid in sub-micro-holes by simultaneous reflectivity, ellipsometry and spectrometry**. *Opt. Express*, **15**(20):13318–13329, 2007. 40, 43

[32] J. D. Hoyland and D. Sands. **Temperature dependent refractive index of amorphous silicon determined by time-resolved reflectivity during low fluence excimer laser heating.** *Journal of Applied Physics*, **99**(6):063516, 2006. 36

[33] Y. Ichikawa, S. Fujikake, T. Takayama, S. Saito, H. Ota, T. Yoshida, T. Ihara, and H. Sakai. **Large-area amorphous silicon solar cells with**

high stabilized efficiency and their fabrication technology. *Photovoltaic Specialists Conference, 1993., Conference Record of the Twenty Third IEEE*, pages 27–33, May 1993. 8

[34] Y. Izawa, Y. Setuhara, M. Hashida, M. Fujita, and Y. Izawa. **Ablation and Amorphization of Crystalline Si by Femtosecond and Picosecond Laser Irradiation**. *Japanese Journal of Applied Physics*, **45**(7):5791–5794, 2006. 18

[35] H. D. Hoffmann H.G. Treusch E. W. Kreutz J. Jandeleit, G. Urbasch. **Picosecond laser ablation of thin copper films**. *Applied Physics A: Materials Science & Processing*, **63**(2):117–121, 1996. 95

[36] R. Grundmuller J. Meier. **Laser structuring for manufacture of thin film silicon solar cells**, 12 2005. 1

[37] H. O. Jeschke, M. E. Garcia, M. Lenzner, J. Bonse, J. Krüger, and W. Kautek. **Laser ablation thresholds of silicon for different pulse durations: theory and experiment**. *Applied Surface Science*, **197-198**:839 – 844, 2002. 76

[38] Yeu-Long Jiang and Yung-Chih Chang. **Rapid crystallization of a-Si:H films with various silicon-to-hydrogen bonding configurations using rapid energy transfer annealing**. *Thin Solid Films*, **500**(1-2):316 – 321, 2006. 45

[39] V. Dutta K. L. Chopra, P. D. Paulson. **Thin-film solar cells: an overview**. *Progress in Photovoltaics: Research and Applications*, **12**(2-3):69–92, 2004. 5, 9

[40] Y. Wakayama Y. Hayashi K. Adachi K. Sato, Y. Gotoh and N. Nishimura. **Highly Textured SnO2:F TCO Films for a-Si Solar Cells**. Technical report, Rep. Res. Lab., Asahi Glass Co. Ltd.42,, 1992. 50

[41] H. Kato, N. Kashio, Y. Ohki, K. S. Seol, and T. Noma. **Band-tail photoluminescence in hydrogenated amorphous silicon oxynitride and silicon nitride films**. *Journal of Applied Physics*, **93**(1):239–244, 2003. 40

[42] J.M. Leng, J.J. Sidorowich, M. Senko, and J. Opsal. **Simultaneous measurement of six layers in a silicon on insulator film stack using visible-near-IR spectrophotometry and single-wavelength beam profile reflectometry**. *Thin Solid Films*, **313-314**(0):270 – 275, 1998. 40, 43

[43] V.S.Y. Lin, K. Motesharei, K. S. Dancil, M. J. Sailor, and M. R. Ghadiri. **A Porous Silicon-Based Optical Interferometric Biosensor**. *Science*, **278**(5339):840–843, 1997. 40

[44] J. M. Liu. **Simple technique for measurements of pulsed Gaussian-beam spot sizes**. *Opt. Lett.*, **7**(5):196–198, May 1982. 20

[45] X. Liu, D. Du, and G. Mourou. **Laser ablation and micromachining with ultrashort laser pulses**. *Quantum Electronics, IEEE Journal of*, **33**(10):1706–1716, 1997. 18

[46] J. Stuchlík A. Fejfar J. Ko&ccaron M. Ledinský, A. Vetushka. **Raman mapping of microcrystalline silicon thin films with high spatial resolution**. *physica status solidi (c)*, **7**(3-4):704–707, 2010. Institute of Physics, Academy of Sciences of the Czech Republic, Cukrovarnická 10, 162 53 Prague 6, Czech Republic. 40

[47] H. S. Kim S. C. Jeoung D. Kim J.-I. Lee H. Y. Chu H. R. Kim M. Park, B. H. Chon. **Ultrafast laser ablation of indium tin oxide thin films for organic light-emitting diode application**. *Optics and Lasers in Engineering*, **44**:138–146, 2006. 49

[48] P.T Mannion, J Magee, E Coyne, G.M OConnor, and T.J Glynn. **The effect of damage accumulation behaviour on ablation thresholds and damage morphology in ultrafast laser micro-machining of common metals in air**. *Applied Surface Science*, **233**(1-4):275 – 287, 2004. 20, 76

[49] Shyam Mehta. **27th Annual Data Collection Results**. Technical report, PV News, 2011. 3

[50] P. Mei, J. B. Boyce, M. Hack, R. A. Lujan, R. I. Johnson, G. B. Anderson, D. K. Fork, and S. E. Ready. **Laser dehydrogenation/crystallization**

of plasma-enhanced chemical vapor deposited amorphous silicon for hybrid thin film transistors. *Applied Physics Letters*, **64**(9):1132–1134, 1994. 45

[51] C Molpeceres, S Lauzurica, JL Ocana, JJ Gandia, L Urbina, and J Carabe. **Microprocessing of ITO and a-Si thin films using ns laser sources**. *J. Micromech. Microeng*, **15**(6):1271–1278, JUN 2005. 1, 49, 105

[52] Carlos L. Molpeceres, Monica Colina, Miguel Holgado, Miguel Morales, Isabel Sanchez-Aniorte, Sara Lauzurica, Juan J. Garcia-Ballesteros, and J. L. Ocaña. **Optical characterization of the heat-affected zone in laser patterning of thin film a-Si:H**. *SPIE Proceedings*, pages 72020R–72020R–10, 2009. 41

[53] M. B. Pandit A. H. Jahagirdar D. Scheiman N. G. Dhere, S. R. Ghongadi. **CIGS2 thin-film solar cells on flexible foils for space power**. *PROGRESS IN PHOTOVOLTAICS: RESEARCH AND APPLICATIONS*, **10**(6):407–416, 2002. 8

[54] S. Nolte, C. Momma, H. Jacobs, A. Tünnermann, B. N. Chichkov, B. Wellegehausen, and H. Welling. **Ablation of metals by ultrashort laser pulses**. *J. Opt. Soc. Am. B*, **14**(10):2716–2722, Oct 1997. 14

[55] S.R. Praschek, W. Riedl, H. Hoermann, and H.G. Goslowsky. **Laser patterning of a-Si solar modules with transparent conducting zinc oxide back electrodes**. *Photovoltaic Specialists Conference, 1991., Conference Record of the Twenty Second IEEE*, pages 1285 –1289 vol.2, oct 1991. 8, 35

[56] A.M. Prochorov. *Laser Heating of Metals*. Optics and Optoelectronics Series. Taylor & Francis Group, 1990. 16

[57] C. Santato, G. Mattei, W. Ruihua, and F. Mecarini. **In situ micro Raman investigation of the laser crystallization in Si thin films plasma enhanced chemical vapor deposition-grown from He-diluted** SiH_4. *Journal of Applied Physics*, **95**(10):5366–5372, 2004. 36, 45

[58] A. Shah, J. Meier, A. Buechel, U. Kroll, J. Steinhauser, F. Meillaud, H. Schade, and D. Domine. **Towards very low-cost mass production of thin-film silicon photovoltaic (PV) solar modules on glass**. *Thin Solid Films*, **502**(1-2):292 – 299, 2006. Selected Papers from the 5th International Conference on Coatings on Glass (ICCG5)- Advanced Coatings on Glass and Plastics for Large-Area or High-Volume Products - ICCG-5. 2

[59] C. Smit, R. A. C. M. M. van Swaaij, H. Donker, A. M. H. N. Petit, W. M. M. Kessels, and M. C. M. van de Sanden. **Determining the material structure of microcrystalline silicon from Raman spectra**. *Journal of Applied Physics*, **94**(5):3582–3588, 2003. 36

[60] K. Sugioka, M.C. Gower, R.F. Haglund, A. Pique, F. Traeger, J.J. Dubowski, and W. Hoving, editors. *Excimer ablation of ITO on flexible substrates for large format display applications*, **4637** of *Presented at the Society of Photo-Optical Instrumentation Engineers (SPIE) Conference*, June 2002. 49

[61] T. Szorenyi, Z. Kantor, and L.D. Laude. **Atypical characteristics of KrF excimer laser ablation of indium-tin oxide films**. *Applied Surface Science*, **86**(1-4):219 – 222, 1995. 66

[62] D.S. Ginley T.J. Coutts, J.D. Perkins and T.O. Mason. **Transparent Conducting Oxides: Status and Opportunities in Basic Research**. In *195th Meeting of the Electrochemical Society*, 1999. 49

[63] D. Toet, P. M. Smith, T. W. Sigmon, T. Takehara, C. C. Tsai, W. R. Harshbarger, and M. O. Thompson. **Laser crystallization and structural characterization of hydrogenated amorphous silicon thin films**. *Journal of Applied Physics*, **85**(11):7914–7918, 1999. 45

[64] A. T. Voutsas, M. K. Hatalis, J. Boyce, and A. Chiang. **Raman spectroscopy of amorphous and microcrystalline silicon films deposited by low-pressure chemical vapor deposition**. *Journal of Applied Physics*, **78**(12):6999–7006, 1995. 39

[65] W.Shinohara, M. Shima, S. Taira, K. Uchihashi, and A. Terakawa. **Applications of laser patterning to fabricate innovative thin-film silicon solar cells**. *SPIE Proceedings*, pages 61070J–61070J–18, 2006. 3, 36, 85, 89

[66] Shizhou Xiao. *Picosecond laser ablation of indium tin oxide thin film.* PhD thesis, Fakultät für Maschinenbau der Ruhr-Universität Bochum, 2012. vii, 15, 16, 17

[67] O. Yavas and M. Takai. **Effect of substrate absorption on the efficiency of laser patterning of indium tin oxide thin films**. *Journal of Applied Physics*, **85**(8):4207–4212, 1999. 66, 73

[68] O. Yavas and M. Takai. **High-Speed Maskless Laser Patterning of Thin Films for Giant Microelectronics**. *Japanese Journal of Applied Physics*, **38**(Part 1, No. 12B):7131–7134, 1999. 73

[69] J. H. Yoo, S.H. Jeong, R. Greif, and R. E. Russo. **Explosive change in crater properties during high power nanosecond laser ablation of silicon**. *Journal of Applied Physics*, **88**(3):1638–1649, 2000. 18

[70] Z. Yuan, Q. Lou, J. Zhou, J. Dong, Y. Wei, Z. Wang, H. Zhao, and G. Wu. **Numerical and experimental analysis on green laser crystallization of amorphous silicon thin films**. *Optics & Laser Technology*, **41**(4):380 – 383, 2009. 36

[71] H. Zou, L. Wu, X. Huang, F. Qiao, P. Han, X. Zhou, Z. Ma, Y. Liu, W. Li, and K. Chen. **Microstructure properties of nanocrystalline silicon/SiO2 multilayers fabricated by laser-induced crystallization**. *Thin Solid Films*, **491**(1-2):212 – 216, 2005. 36